UC Berkeley
UC Berkeley Electronic Theses and Dissertations

Title

Molecular MRI Approaches for Noninvasively Characterizing Renal Pathophysiology

Permalink

https://escholarship.org/uc/item/81c1h0jc

Author

Shin, Soo Hyun

Publication Date

2022

Peer reviewed|Thesis/dissertation

Molecular MRI Approaches for Noninvasively Characterizing Renal Pathophysiology

By

Soo Hyun Shin

A dissertation submitted in partial satisfaction of the

requirements for the degree of

Joint Doctor of Philosophy
with University of California, San Francisco

in

Bioengineering

in the

Graduate Division

of the

University of California, Berkeley

Committee in charge:

Professor Moriel H. Vandsburger, Chair
Professor George A. Brooks
Professor Peder E. Z. Larson

Spring 2022

Abstract

Molecular MRI Approaches for Noninvasively Characterizing Renal Pathophysiology

by

Soo Hyun Shin

Doctor of Philosophy in Bioengineering

University of California, Berkeley

Professor Moriel H. Vandsburger, Chair

Renal diseases that involve filtration function loss are usually diagnosed through measuring estimated glomerular filtration rate (eGFR) via blood tests such as blood urea nitrogen and serum creatinine level measurements. Although these methods allow quick assessment of renal function, it does not tell the cause of function loss and lacks adequate sensitivity due to the hyperfiltration by intact nephrons. These limitations become more critical in cases that involve progressive renal function loss such as acute kidney injury (AKI)-to-chronic kidney disease (CKD) transition and chronic graft function loss after renal transplantation, in which microstructural alterations often precede the change in blood marker levels. Biopsy remains the gold standard to pick up these tissue level damages, but the procedure is invasive and prone to sampling errors. Here, the use of novel molecular magnetic resonance imaging (MRI) technique called chemical exchange saturation transfer (CEST) imaging is demonstrated for noninvasively characterizing renal pathophysiology. Specifically, urea was studied as an imaging target and contrast agent of CEST MRI, as urea is a major metabolite responsible for controlling water reabsorption in the kidneys. Characterization of urea showed concentration and pH-dependent CEST contrast, and the feasibility of in vivo urea imaging was demonstrated with heightened CEST contrast in the inner medulla and papilla of the mouse kidneys after urea infusion. This method was further optimized for better quantification of urea by choosing the optimal time point of acquiring CEST data after urea infusion, removing T_1 time effect on the CEST contrast and adopting multi-pool Lorentzian fitting. Lastly, this technique was applied to mouse renal disease models to test its diagnostic potential. Acute and chronic nephropathies were induced in mice, and the CEST data were longitudinally acquired along the disease progression. Since CEST data also reflects the presence of other mobile proteins, metabolites, and semi-solid macromolecules, the CEST contrast from these molecules were also analyzed in addition to urea. The urea CEST showed significant changes upon acute injury development, and the multiparametric CEST clearly distinguished acute and chronic nephropathies. Overall, CEST MRI can observe urea recycling in the mouse kidneys, and allows distinguishing different nephropathies along with other endogenous CEST contrast.

Acknowledgements

First of all, I give my enormous gratitude to my advisor Prof. Moriel Vandsburger. With his remarkable insight and knowledge in science, Moriel has guided me through all the work that I have done and showed me the right way of doing research. He also took care of my personal issues and my career path, which was a great comfort and encouragement for me. I know for sure that I would have not reached this point of graduation without his advising and mentorship. Overall, I have no doubt that it was my greatest luck of the last 5 years to meet him as my Ph.D. advisor.

I am especially indebted to Dr. Michael Wendland. As the managing director of the Berkeley Preclinical Imaging Core (BPIC), he has always solved the problems associated with the MR scanner and my work was never delayed due to a scanner issue. He also helped and advised on my research with his excellent expertise in MR physics, which was especially invaluable at the initial stage of my research. Without his help, I would have not been able to graduate in time.

I extend my gratitude to my dissertation committee members, Prof. George Brooks and Prof. Peder Larson for their constant help and guidance. Since my qualifying exam, they have consistently provided many invaluable comments and pieces of advice during annual meetings that helped me shape my research in the right way. Their comments and questions also enabled me to write this dissertation. It was my great honor to meet them and have them on my dissertation committee.

I am also grateful to my lab mates, past and present, Wissam AlGhuraibawi, AJ Velasquez-Mao, Mark Velasquez, Bonnie Lam, Cindy Ayala, Kevin Godines, and Zeynep Ali. It was joyful to collaborate with my colleagues who all have different backgrounds, and it was a great opportunity for me to learn from and have fun with them both inside and outside of the lab.

I would also like to thank my Korean friends in Berkeley. As Ph.D. students in Berkeley engineering, these friends were always with me for discussing science and engineering in general, sympathizing with me for the hardship of research, and just having a fun time. My special thanks and best wishes go to my roommate and my best friend, Euihyun Choi. I would also like to thank Ha H. Park, Suhong Moon, and Jichan Chung and wish them the best of luck with their degree.

My cousin Dr. Jisoo Shin and her husband Dr. Jaeseung Moon also deserve my special gratitude. This couple came to Berkeley in 2019, and it was the first time that I have any relative in the US. The fact that my relatives are living only 10-minute drive away from my place gave me great comfort, especially during the pandemic era. I truly appreciate the time we spent together, and the hospitality they showed me whenever I visited their place—including aggressive welcoming from their dog Koju.

Lastly, my infinite thanks go to my parents, my brother and sister-in-law, and my lovely niece and nephew Hajeong Shin and Yoonjae Shin, who always sent me endless unconditional support from Korea.

Table of Contents

Chapter 1. Background: Renal Pathophysiology

1.1 Kidney Physiology

1.1.1 Overview of Human Kidney Structure and Function

The kidneys are organs that are responsible for regulating water, inorganic ion balance and acid-base balance as well as removing metabolic waste products and foreign chemicals from the blood. These are a pair of 10 – 12 cm long bean-shaped organs located in the retroperitoneal space[1]. The parenchyma of kidney is composed of cortex and medulla, which are in turn composed of individual filtering units called nephrons. Renal medulla is composed of multiple renal pyramids with their apex connected to minor calyx. Minor calyces merge to major calyces that are connected to the ureter through which the filtrate, urine, is transported to the bladder[2]. The major structure of the human kidney is shown in **Figure 1.1**[3].
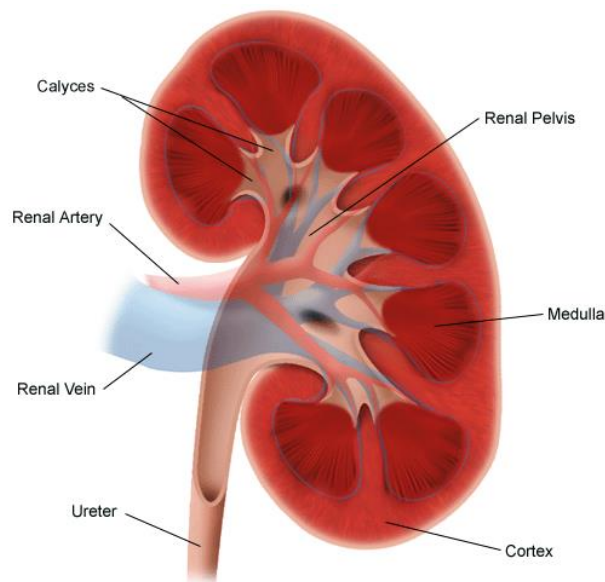
Figure 1.1 Gross anatomy of the human kidney. Adapted from ref [3].

Each kidney has approximately 1 million nephrons. Each nephron is consisted of glomerulus, a compact tuft of capillary loops, and tubules, with one end of the tubule surrounding the glomerulus with Bowman's capsule (**Figure 1.2**)[4]. Blood flows into glomerulus through afferent arteriole and leaves the glomerulus through the efferent arterioles. Substances in the blood that are less than 8 nm in size are filtered through the Bowman's capsule and enter the proximal convoluted tubule, the first segment of the tubule. This process is called the glomerular filtration. As the filtrate passes through next segments of the tubules, loop of Henle and distal convoluted tubules, important solutes such as glucose and water are reabsorbed to peritubular plasma while waste products and toxins are secreted into tubular lumen. The final product, urine, reaches the collecting duct and is transported to the renal pelvis. The detailed procedure of water reabsorption is illustrated in the next section 1.1.2.
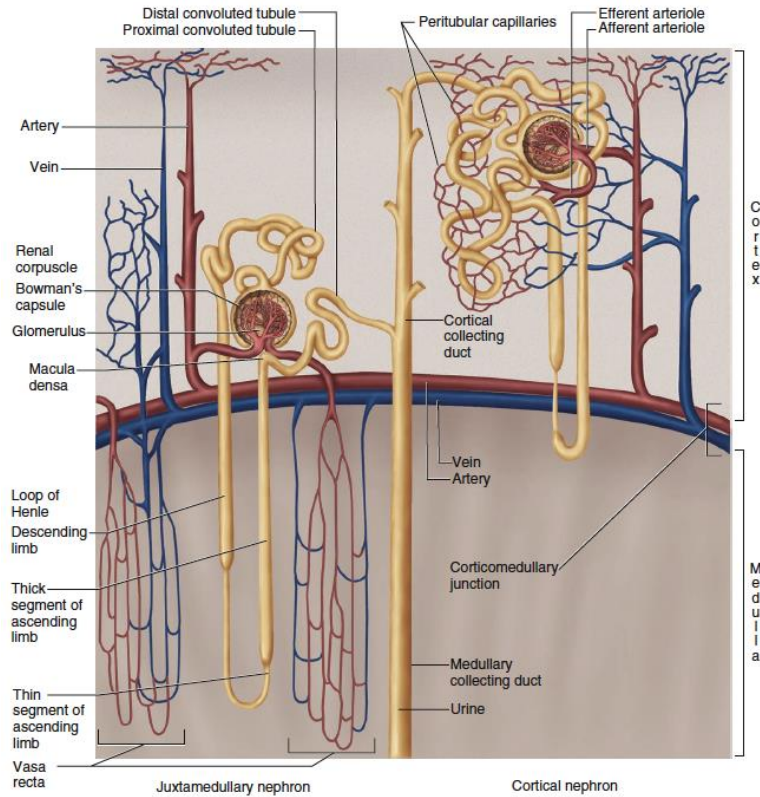
Figure 1.2. Basic structure of a nephron and collecting ducts. Adapted from ref [4].

One good approach of measuring renal filtration function is to measure the volume of fluid filtered from the glomeruli into the tubular lumen per unit time, which is known as glomerular filtration rate (GFR). In a healthy adult, the average GFR is approximately 120 mL/min[5]. The GFR can be assessed by measuring the clearance of any substance that is freely filtered but neither reabsorbed nor secreted in tubules. While our body does not produce such compounds, polysaccharide called inulin perfectly meets these requirements. Intravenously infusing inulin and measuring its excretion through urine can accurately measure the GFR, but this time-consuming and costly procedure is not practical to perform in clinical settings. To quickly estimate the GFR, clearance of metabolite called creatinine is often used as a proxy of GFR. Creatinine is a waste product from muscle cells that undergoes small amount of secretion and no reabsorption. Assuming creatinine production in our body is constant, creatinine clearance is measured by taking the concentration of creatinine in the blood into an empirical equation that accounts for other factors that may affect the creatinine measurements, such as body mass, sex, race and age[6,7]. The resulting estimated GFR (eGFR) is a clinical standard of measuring the renal filtering function.

1.1.2 Water Reabsorption and Urea Recycling

One key function of the kidney is to regulate the water and sodium balance. Both sodium and water freely pass through the Bowman's capsule and more than 99% is reabsorbed. Most of the reabsorption is done in the proximal tubule, but the fine control of reabsorption is performed in the distal convoluted tubules and collecting ducts. Sodium reabsorption is primarily done by active transport by Na^+/K^+-ATPase pumps occurring in all tubular segments except the descending

limb of the loop of Henle. Water reabsorption is by passive transport via aquaporins, dependent on sodium reabsorption and the hyperosmolarity gradient along the loop of Henle.

The hyperosmolarity gradient in the medullary interstitium is a key driver of water reabsorption and urine concentration in the collecting duct. This gradient is mainly achieved through the countercurrent multiplier system represented in the loop of Henle. The ascending limb of the loop is relatively impermeable to water compared to the descending limb, while sodium reabsorption is occurring. Since only sodium is reabsorbed and water does not diffuse out of the tubular lumen, the medullary interstitium around the ascending limb becomes hyperosmotic. In the descending limb, however, is permeable to water and the sodium reabsorption does not occur. Due to the hyperosmolarity built up by the ascending limb, water diffuses out of the tubular lumen, which makes the filtrate become more hyperosmotic as it flows down the descending limb. The filtrate reaches the highest osmolarity when it turns the corner of the loop, and the osmolarity of the filtrate starts decreasing as it flows through the ascending limb. This countercurrent system builds up the hyperosmolarity gradient in the medullary interstitium.

Another key factor that contributes to this hyperosmolarity gradient is the process called urea recycling (**Figure 1.3**)[8–10]. Urea is a major waste product from protein metabolism and the most abundant metabolite in the urine. Urea is freely filtered in the glomerulus and 50% is reabsorbed in the proximal tubule. The remaining flows through the loop of Henle, where the urea that has accumulated in the medullary interstitium is secreted into the tubular lumen. Urea is reabsorbed again in the distal convoluted tubule and cortical collecting duct. Then almost half of the urea is reabsorbed from the inner medullary collecting duct (IMCD), which is secreted to the loop of Henle as previously described. Only a small amount (~5%) of the urea reabsorbed at the IMCD is washed out by blood vessels, most of the reabsorbed urea remains in the inner medulla and contributes to the hyperosmolarity in the interstitium and drives water reabsorption.
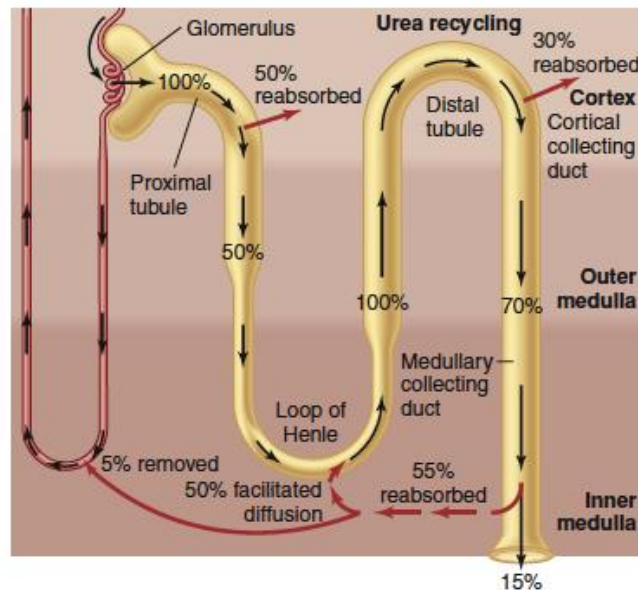
Figure 1.3 Urea recycling along renal tubules. Adapted from ref [4].

1.2 Kidney Diseases, Pathology and Diagnosis

1.2.1 Acute Kidney Injury (AKI)

Acute kidney injury (AKI) comprises many types of renal diseases that involve an abrupt decline in renal function. Based on Kidney Disease: Improving Global Outcomes (KDIGO) classification, AKI is diagnosed if 1) serum creatinine level increases by 0.3 mg/dL or more in 48 hours or 2) rises to at least 1.5-fold from baseline within a week, or 3) the urine output is less than 0.5 mL/kg/h for 6 hours[11].

There are multiple different etiologies, including but not limited to sepsis, volume depletion, hemodynamic instability and nephrotoxic drugs and contrast agents[12]. A multi-national meta-analysis studies showed that AKI affects 22% of hospital in-patients, with showing 5 times higher mortality rate than patients without AKI[13]. AKI is particularly common in patients in the intensive care unit (ICU), affecting more than 50% of ICU patients. Among these AKI patients in the ICU, 25% end up being treated with renal replacement therapy (RRT)[14].

Wide range of pathological features are observed from the biopsy and animal models of AKI. Cellular injuries on tubular epithelial cells are common histological features observed from models of ischemia-reperfusion and hypoxic injury and other cytotoxic models[15]. These cellular damages are characterized by a loss of cytostructural integrity and cell polarity with mislocation of proteins[16]. Mitochondrial damage may also occur by nephrotoxic agents such as cisplatin and resultant accumulation of reactive oxygen species (ROS) may cause oxidative stress[17]. Inflammation is also a common response to the onset of AKI, represented as significant deposition of the complement activation produce C3d on tubular basement membranes[18].

After an incidence of AKI, there are three possible outcomes: 1) Full recovery of renal function, 2) partial recovery of renal function and progression to chronic kidney disease (CKD), which is further discussed in the next section, and 3) no recovery of renal function and directly leading to end-stage renal disease (ESRD)[12]. AKI is a long-term risk factor of CKD, showing 9 times higher risk of developing CKD compared to those without AKI[19,20]. Several potential pathological mechanisms are expected to be associated with AKI-to-CKD transition[21]. Reduced vascular density after AKI may activate hypoxia-inducible pathways and pro-inflammatory processes. If substantial number of nephrons are lost as a result of AKI, hyperfiltration by remaining nephrons may occur and lead to hypertrophy of glomeruli and tubulointerstitial fibrosis.

1.2.2 Chronic Kidney Disease (CKD)

Chronic kidney disease (CKD) is typically defined as a reduction of renal function with estimated glomerular filtration rate (eGFR) less than 60 mL/min that persists for at least 3 months[22]. Approximately 10% of adults worldwide are affected by CKD, resulting in 1.2 million deaths per year[23,24]. Based on the severity and progression of renal function loss, CKD is classified into 5 stages, with the last stage called end-stage renal disease (ESRD), which is defined as a condition with eGFR < 15 mL/min, and a renal replacement therapy (RRT) such as dialysis and kidney transplant is required (**Table 1.1**)[25].

Diabetes and hypertension are the main causes of CKD[26,27]. Diabetes accounts for 30 ~ 50% of all CKD worldwide. Hyperglycemia-induced metabolic and hemodynamic changes stimulate the secretion of profibrotic cytokines and lead to increased systemic and intraglomerular

pressure[28]. Subsequently, glomerular hyperfiltration and hyperperfusion occur and glomerular hypertrophy takes place, leading to albuminuria and further decline of renal function.

Stage	Description	GFR (mL/min/1.73 m^2)
1	Kidney damage with normal or ↑ GFR	≥ 90
2	Kidney damage with mild ↓ GFR	60 – 89
3	Moderate ↓ GFR	30 - 59
4	Severe ↓GFR	15 - 29
5	Kidney failure	<15 (or dialysis)

Table 1.1 Classification of chronic kidney disease (CKD). Adapted from ref [25].

A common hallmark of CKD is fibrosis, characterized by an excessive accumulation of the extracellular matrix (ECM)[22]. The development of fibrosis can be triggered by many types of injuries such as wound, infection, metabolic disorders and inflammation. These injuries affect the epithelial and endothelial cells of renal parenchyma, stimulating inflammatory cells to recruit mesenchymal cells such as fibroblasts and myofibroblasts which ultimately produce ECM in uncontrolled fashion[29]. This process of fibrosis development becomes irreversible and self-maintained at a certain stage, progressively substituting functioning renal parenchyma with scar tissues and leading to progressive renal function loss[30].

Once the CKD is diagnosed, several strategies to preserve the renal function should be considered. Low-protein, low sodium diets are recommended in general as a lifestyle change to alleviate intraglomerular hypertension and subsequent hyperfiltration and fibrosis[31]. Pharmacological approach includes renin-angiotensin-aldosterone pathway modulators such as angiotensin-converting enzyme (ACE) inhibitors, which reduce intraglomerular pressure by inducing vasodilation of efferent arterioles[32]. If CKD progresses to ESRD even with these preservative strategies, the patient should be treated with renal replacement therapy.

1.2.3 Renal Transplantation

Renal replacement therapy (RRT) is a therapy that replaces the normal filtering function of the kidneys either with dialysis or kidney transplant. Since dialysis procedure significantly hampers the quality of life and was originally designed to be a temporary method to sustain the filtering function, renal transplant is the ultimate form of RRT currently available.

From 1988 to 2022, 523,208 patients received kidney transplants in the US, and the annual number of recipients are steadily increasing, from 8,878 in 1988 to 24,670 in 2021[33]. Although kidney transplant is the only option for ESRD patients and the needs for the allograft are increasing, only 25 ~ 30% of the patients successfully receive the transplant and 6% of patients die while waiting for a transplant each year[34].

Even after successful transplant, the function of the transplanted allograft should be carefully monitored due to various risk factors that induce graft function loss (**Figure 1.4**)[35]. Short-term factors include delayed graft function (DGF), which is defined as the need for dialysis during the first week after transplantation due to acute tubular necrosis[36]. Immune rejection, whether acute or chronic, is also a major issue associated with graft function loss[37]. Calcineurin inhibitors (CNI)

such as cyclosporin and tacrolimus are given to transplant recipients as immunosuppressives, but CNI may have nephrotoxicity which also can contribute to graft function loss[38]. BK polyoma virus, which is inactive under normal immune status, may cause nephritis when immune system is suppressed and lead to graft function loss[39]. Due to these various complications, more than 50% of allografts are lost by 10 years after the transplant and end up requiring dialysis or re-transplantation[34]. To preserve and/or slow down the loss of allograft function, multiple diagnostic measures that are also used for AKI and CKD are performed to monitor the allograft function, which will be described in the next section.
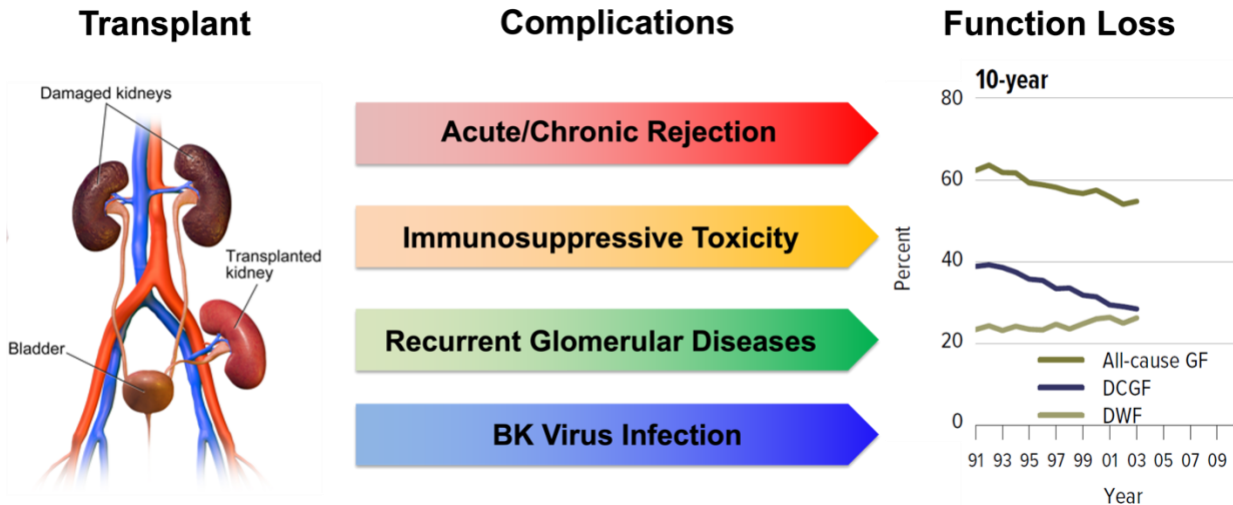
Figure 1.4 Graft function loss after renal transplant. Various complications may arise after the transplantation, which result in more than 50% of graft function loss in 10-year post-transplantation. Adapted and modified from ref [34].

1.3 Kidney Disease Diagnostics

1.3.1 Serum Creatinine Level

Serum creatinine level is the most commonly used biomarker in clinics to measure the renal filtration function. This measurement is used to calculate eGFR, which is used to define AKI and classify CKD stages. For transplant recipients, serum creatinine level is measured every 2 ~ 3 months after a year to monitor any function loss[40]. Although this approach allows quick assessment of the renal function, it is not specific to the cause of function loss and requires additional differential diagnosis. The eGFR measurement may not accurately reflect the kidney status due to the hyperfiltration by intact nephrons. This often hinders timely detection of renal function loss until 50% of the renal function is loss[41]. This late detection is also observed through histological observations as microstructural changes often precede the decline of eGFR[42,43].

1.3.2 Biopsy

Biopsy is a gold standard for identifying the underlying pathology that causes renal function loss. Biopsy is broadly indicated in conditions of unexplained acute or chronic progression of renal failure, persistent hematuria and renal allograft dysfunction[44]. For renal

transplant recipients, protocol biopsy, which is performing renal biopsy every 6 ~ 12 months, is also recommended for detecting any subclinical rejection[45,46]. For tissue sampling, two cylinders of cortex tissue with a minimal length of 1 cm and a diameter of >1.2 mm are needed[47]. 10 ~ 15 glomeruli should be sampled for examination[48]. The sampled tissue cores are divided into samples for light, immunofluorescence, and electron microscopy (**Figure 1.5**)[49].

Considering that each kidney is composed of approximately 1 million nephrons, acquiring only 10 ~ 15 glomeruli is expected to have high chance of sampling errors. Although the sampling procedure is usually guided by ultrasound imaging, the whole procedure is invasive and has a risk of developing complications such as hematuria[50]. There are also several cases that biopsy itself is contraindicated, such as small kidneys and uncontrolled hypertensions[48].
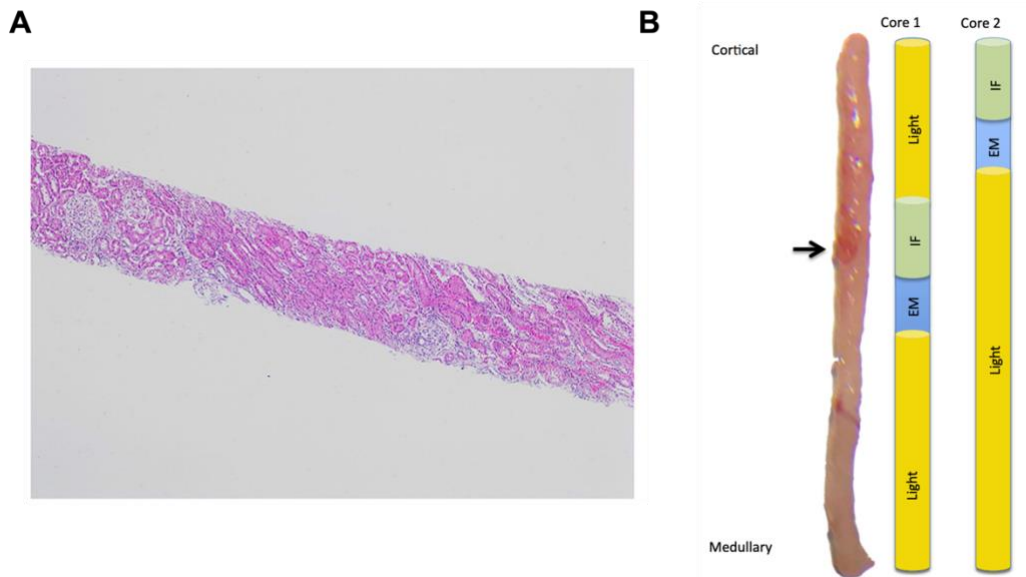
Figure 1.5 Kidney biopsy core sample. (A) hematoxylin and eosin (H&E)-stained kidney biopsy core. (B) Gross image of the biopsy core. The arrow indicates a vascular tuft, a sign of a confluence of glomeruli. Two cores are sampled and divided into samples for light (Light), immunofluorescence (IF) and electron (EM) microscopy. Adapted from refs [48, 49].

1.3.3 Medical Imaging Modalities

Ultrasonography (US) is the first-line imaging method for monitoring kidneys[50]. The US imaging is mostly focused on measuring the size and echogenicity of the kidneys (**Figure 1.6**). Kidney length in adults usually range from 10 to 12 cm, and the thickness of the cortex should be 7 ~ 10 mm[51,52]. Increased echogenicity shows correlation to interstitial fibrosis, tubular atrophy and glomerulosclerosis[53]. Advanced US techniques such as Doppler ultrasound may also allow measuring the renal blood flow[54,55]. Yet, the sensitivity and specificity of US renal imaging in general varies significantly[56].

Nuclear medicine, especially renal scintigraphy using ^{99m}Tc-MAG3 can also be used to noninvasively measure the renal function[57]. The kinetics of radioactive tracer can be analyzed and the perfusion, filtration and excretion rates can be estimated[58]. Although this technique allows

multiple aspects of renal function, it is not widely adopted in the clinics as it requires long scan time, shows high tissue background and low spatial resolution.
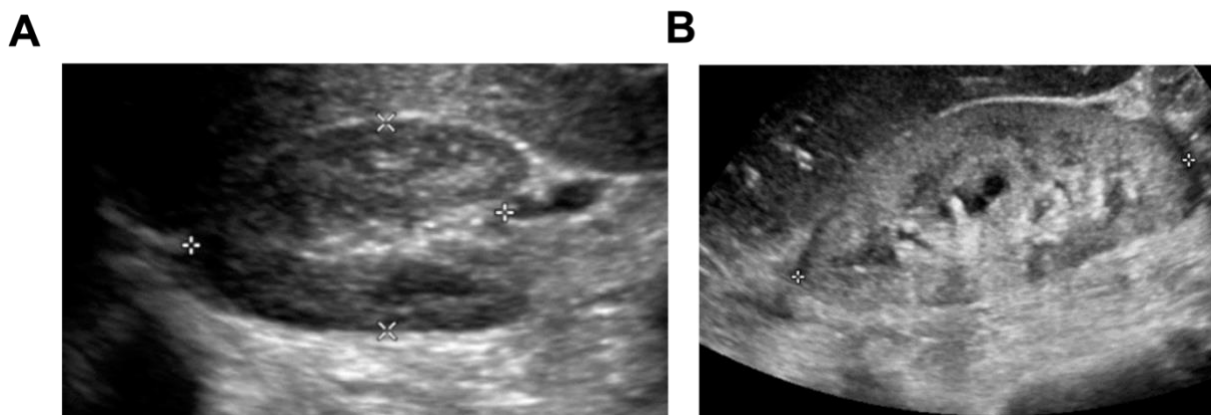
Figure 1.6 Ultrasonography (US) of human kidneys. (A) Transverse US image of a normal right kidney. (B) Longitudinal US image of a right kidney with abnormal bright renal parenchyma in a patient with multiple myeloma and AKI. Adapted from ref [53].

Similar to US, computed tomography (CT) is also focused on detecting macroscopic structural abnormalities. Observing fluid accumulation such as urinoma and hematoma and measuring the volumetric size of the kidneys are feasible via CT[59]. Dynamic contrast-enhanced CT may provide hemodynamic information such as renal blood flow and tissue perfusion, but this technique is limited due to the risk of contrast-induced nephropathy and exposure to X-ray irradiation[60,61].

Finally, magnetic resonance imaging (MRI) is used as a second-line imaging when US or CT has been non-diagnostic[62]. While MRI can be used to scan structural abnormalities with its high soft tissue contrast, angiography can also be performed to diagnose renal artery stenosis[63,64]. However, MR angiography often requires gadolinium-based contrast agents, which can cause nephrogenic systemic fibrosis in cases of GFR < 30 mL/min[65,66]. Still, MRI has large potential of being used for renal imaging since multiple types of contrasts that reflect different aspects of physiological features can be achieved by varying the scan protocol. Several novel MR techniques that do not require contrast agents, such as diffusion-weighted imaging and blood oxygenation level-dependent MRI are being developed and tested for their utilities in identifying parenchymal damages and associated renal function loss[67]. In the next chapter, some of these novel MR techniques that are focused on imaging molecular events will be described.

Chapter 2. Background: Molecular Magnetic Resonance Imaging

2.1 Principles of Magnetic Resonance Imaging

Magnetic resonance imaging (MRI) is based on the concept of nuclear spins, which can be quantitatively explained by quantum mechanics. Still, the macroscopic behavior of the sum of nuclear spins can be described by classical electrodynamics. Since this section is intended to give only a brief introduction of the principles MRI, only the classical description of MR phenomenon is treated. For complete coverage of the principles of MRI and the quantum mechanical basis of MR signal formation, readers are referred to [68–70].

2.1.1 B_0 field: Magnetization and Precession

Atoms with odd numbers of protons possess a nuclear spin angular momentum, or for simplicity called spins. Among those spins, hydrogen is the most abundant in our body (mostly due to water, H_2O) and the most sensitive spin. In most cases, MR signals and images are created from hydrogen spins.

Once the external magnetic field, which is often termed as B_0 field, is applied, spins align parallel or anti-parallel to the direction of that field. The direction of B_0 field is often set to z-direction. The ratio of the parallel and anti-parallel spin populations follows the Boltzmann distribution. Typically, there is an excess of 4 out of a million in the parallel state, forming a net magnetization vector with which the MR signal is formed.

If the net magnetization is made to point in a different direction than the B_0 field, the magnetization vector shows precessional behavior around the direction of the B_0 field. The frequency of this precession, which is termed Larmor frequency, is determined by the strength of B_0 field and the gyromagnetic ratio, a constant unique for different nuclear species.

$$\omega = \gamma B \tag{2.1}$$

ω is the Larmor frequency, B is the magnetic field applied (B_0), and γ is the gyromagnetic ratio, which is approximately 42.57 MHz/T for the hydrogen. In clinical settings, B_0 is usually 1.5 or 3 T. To generate MR signal, additional radiofrequency (RF) magnetic field tuned to the Larmor frequency is applied to the spins, which subsequently starts oscillating at the Larmor frequency.

2.1.2 B_1 field: Excitation and Relaxation

The RF field applied to nutate the spins is called the B_1 field. This field tuned at the Larmor frequency is applied in the xy-plane and the spins aligned to the B_0 field tips away from the z-direction as it starts rotating around the direction of the B_1 field. The angle that the net magnetization vector rotates depends on the duration and the strength of the applied B_1 field, which are typically a few milliseconds and a few microtesla, respectively. This instant flip of aligned spins into xy-plane is referred as excitation. Once the spins are excited at a predetermined flip angle and the RF field is off, these spins start precessing again around the z-direction. The

precession or oscillation of the magnetization vectors induce an electromotive force (EMF) in an RF receiver coil centered around the xy-plane. The EMF signal recorded via the receiver coil is used to reconstruct the MR image.

While the magnetization vectors precess in the xy-plane around the B_0 field direction after the RF field is turned off, these vectors also start returning to their equilibrium state. This process is called relaxation. The transverse portion (in xy-plane) of the magnetization starts decaying after the excitation pulse, and the longitudinal portion (z-direction) of the magnetization recovers its original magnitude before the excitation pulse. The time constant that determines the rate at which the longitudinal magnetization returns to equilibrium is called T_1, and this relaxation process is termed spin-lattice relaxation or longitudinal relaxation. Similarly, the time constant determining how fast the transverse magnetization decays is called T_2, and this relaxation process is called spin-spin relaxation. The T_1 and T_2 relaxation after 90° RF pulse can be described as follows

$$M_z = M_o(1 - e^{-t/T_1}) \tag{2.2}$$

$$M_{xy} = M_o e^{-t/T_2} \tag{2.3}$$

M_z is the longitudinal magnetization, and M_{xy} is the transverse magnetization. M_0 is the net magnetization at the equilibrium.

Microscopically, these relaxation times are dependent on the random fluctuations of the magnetic field generated by the motion of surrounding magnetic dipoles. This means that T_1 and T_2 relaxation times are affected by the surrounding environment, such as molecular structures and the state of materials. Thus, different biological tissues have different T_1 and T_2 times, and several examples are shown in **Table 2.1**[69]. Due to these differences in relaxation times, the contrast between different tissue can be generated by controlling the timing and amplitude of RF pulse as well as the timing of the signal readout.

Tissue	T_1 (ms)	T_2 (ms)
White matter	600	80
Gray Matter	950	100
Cerebrospinal Fluid	4500	2200
Muscle	900	50
Fat	250	60
Blood	1200	100-200*

Table 2.1 Typical T_1 and T_2 values of biological tissues at 1.5 T. *Arterial blood has higher T_2 values than venous blood. Adapted from [69].

2.1.3 Gradient Field

When the spins are exposed the B_0 field, they all precess at the same frequency. Since the RF receiver coil encompasses the entire region of interest, the MR signals are recorded in the form

of a single time waveform. This means it is impossible to distinguish the signals generated from different spatial locations if B_0 is the only field applied.

For spatial localization of the MR signals, additional linear gradient magnetic fields are applied on top of the B_0 field. For instance, if a gradient G is applied in the x-direction, then the applied magnetic field is $B_0 + Gx$. This means nuclear spins along the x-direction are exposed to different field strength and have different precession frequencies. Thus, the spatial locations of the spins can be recorded as different Larmor frequencies. In this case, Fourier transform can be applied to the total sum of spin oscillations that are recorded as a single time waveform, and the contribution from each frequency can be measured, which translates to the spatial location of the origin of the signal.

2.1.4 Chemical Shift

Chemical shift is a displacement of the resonance frequency of a nuclear spin due to the shielding effect created by surrounding electrons. This effect can be described as follows.

$$B_{eff} = B_0(1 - \sigma) \tag{2.4}$$

B_{eff} is the effective field that the nuclear spins are exposed to, and σ is the shielding constant, which is a function of chemical environment.

Since the magnetic field changes based on the chemical environment, the same nucleus will have different Larmor frequency based on the chemical environment. This difference in Larmor frequency is also linearly dependent on the B_0 field strength, as Larmor frequency itself is linearly proportional to the B_0 field strength. Chemical shift is often defined in a form of parts per million (ppm) with respect to a reference frequency ω_r. If the resonant frequency of the target nuclear spin is ω_s, then the chemical shift δ is defined as follows.

$$\delta = \frac{\omega_s - \omega_r}{\omega_r} \times 10^6 \tag{2.5}$$

In human body the two most abundant types of hydrogens are those in water and in fat. Although fat is composed of many types of hydrogens ($-CH_2$, $-CH_3$, etc.), it is assumed to have 3.5 ppm chemical shift from water. As such, different molecules or chemical structures can be identified as distinct peaks in a nuclear magnetic resonance (NMR) spectrum.

2.2 Chemical Exchange Saturation Transfer (CEST)

2.2.1 Principles of CEST

Chemical exchange saturation transfer, or CEST, is a molecular MRI technique that generates contrast from a molecule of interest by applying saturation pulses tuned to the offset frequency (chemical shift) of exchangeable protons on the molecule and recording the subsequent reduction in the water signal (**Figure 2.1**)[71]. The saturation pulses are RF fields that are turned on longer than the excitation pulses to equalize the number of two spin populations in two energy states so that the net magnetization disappears[72]. While the protons on the molecule of interest, or solute, are being saturated, these protons may physically exchange with protons on other molecules such as water. The dipole-dipole interaction also exchanges the magnetization with the one in other molecules. As saturated spins are transferred to the free water pool, the water signal is reduced. This process is repeated multiple times as unsaturated water protons are also transferred to the solute, which again are saturated and return to the water pool. The repetition of this process makes saturated spins accumulate in the water pool, which translates to the reduction of the water signal. The difference between the water signal before and after applying the saturation pulse generates the contrast and reflects the presence of the solute of interest.

One advantage of CEST is that the signal from the molecule of interest is amplified[73,74]. NMR spectroscopy or magnetic resonance spectroscopy (MRS) record MR signals that are directly coming from the solutes, which usually have much lower concentration compared to water protons (110 M) in our body. Thus, the low signal-to-noise ratio (SNR) is inevitable. CEST leverages the chemical exchange between the solute and water to accumulate the saturated spins in the water pool, which results in the amplification of the MR signal from the solute. Consequently, CEST shows higher SNR and retains high spatial resolution and molecular specificity.
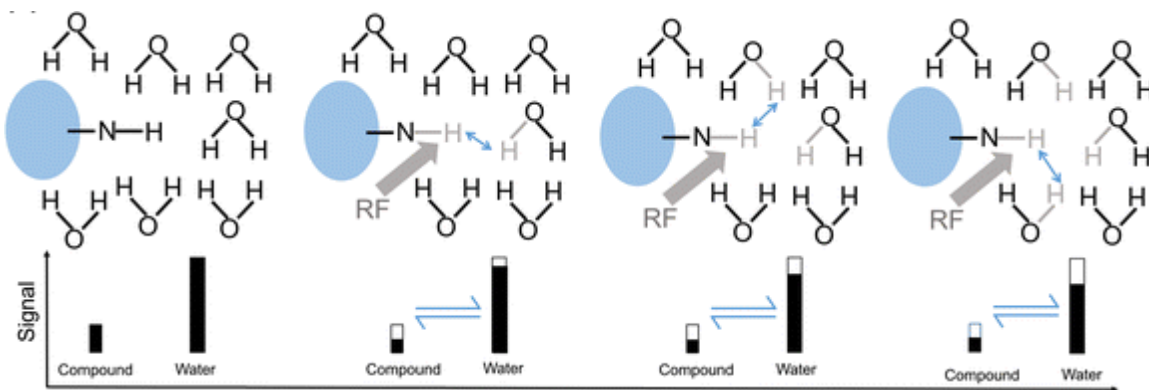
Figure 2.1 The process of CEST contrast generation. In the two-pool system, in this case water and amide (-NH) protons, RF saturation pulses are applied at the resonant frequency of amide protons while these protons exchange with free water protons. This process is repeated, and the saturated protons accumulate in the water pool, resulting in the reduction of water signal. Adapted from ref [71].

2.2.2 CEST Data Acquisition

A general pulse sequence for CEST acquisition is shown in **Figure 2.2A**. A train of RF pulses are applied first to saturate the magnetization, and the readout sequence for recording water signals follows. Readout sequences are designed to be as short as possible to minimize the relaxation after saturation[75]. This saturation-readout sequence is repeated with varying the offset frequency that the saturation RF pulses are tuned to. These offset frequencies are often symmetrically around the water resonant frequency, which is set to 0 ppm. The water signals recorded along the saturated offset frequencies can be expressed as a spectrum, which is termed Z-spectrum (**Figure 2.2B**)[76]. The significant signal reduction (almost to 0) at 0 ppm reflects the direct water saturation by the RF pulses. If other molecules with exchangeable protons exist and the resonating frequency of those protons fall in the range of the acquired Z-spectrum, it will be reflected in the Z-spectrum as a signal reduction.
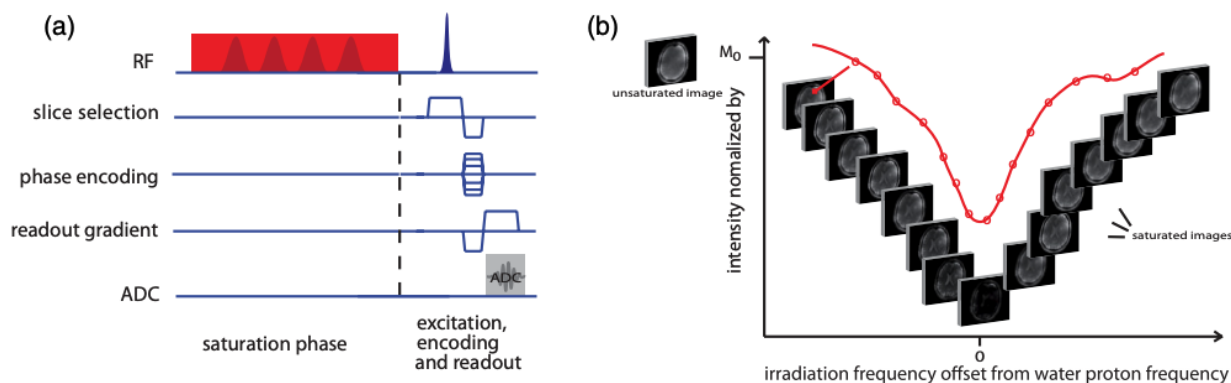
Figure 2.2 (A) A typical pulse sequence for CEST MRI. A train of RF pulses precede the readout part of the sequence for saturation. Red block in the RF part indicates a case when continuous wave pulse is used, instead of pulsed saturation. After the saturation phase, excitation, encoding and readout part follows. (B) An example Z-spectrum and associated MR images. Multiple offset frequencies are irradiated with saturation pulses and water signals are recorded from each offset frequency. Due to the direct water saturation, water signal reduction becomes more evident in the images acquired with saturation at the offset frequencies closer to 0 ppm. Adapted from ref [76].

Saturation scheme should be carefully tailored for the target molecule. Many parameters that define the saturation scheme, such as pulse amplitude, shape, duration and duty cycle, affect the Z-spectrum and thus the CEST contrast measured. The offset frequency ($\Delta\omega$) and exchange rate (k_{ex}) of the target exchangeable protons are crucial factors that should be taken into account when choosing the saturation scheme. If the offset frequency of the exchangeable is too close to the water resonant frequency, the solute peak may coalesce with the water peak and the CEST effect might not be detected, which is called a spillover effect[77]. To avoid the spillover effect, it is advised to lower the saturation power so that two peaks on the Z-spectrum can be well resolved[78]. In terms of exchange rate of the protons, fast exchanging protons ($k_{ex} \gg \Delta\omega$) often require high saturation power to ensure sufficient saturation before the solute protons transfer to the water pool[79]. The duty cycle of saturation pulses also affects the CEST contrast. For fast exchanging

protons, the delay time between the saturation pulses is modeled only as relaxation time for the protons that have been saturated and transferred to the water pool, whereas for the slowly exchanging ($k_{ex} \ll \Delta\omega$) protons this delay time is also used for additional transfer of saturated protons[80].

Field inhomogeneity should be concerned while acquiring a full Z-spectrum. B_0 field inhomogeneity results in the discrepancy between the prescribed offset frequency of the RF pulse and the actual offset frequency that is saturated. This ends up in inaccurate measurement of CEST contrast at a specific offset frequency. To correct the B_0 field inhomogeneity, water saturation shift referencing (WASSR) method is often adapted[81]. This method acquires an additional Z-spectrum with very low saturation power and narrow range offset frequencies (usually -2 ~ 2 ppm or less) to check the actual offset frequency at which the water is saturated (e.g. the offset frequency where the largest signal reduction is observed). This approach allows how much B_0 shift is present at each voxel and the full Z-spectrum at each voxel can be shifted accordingly to correct for the field inhomogeneity.

2.2.3 CEST Data Analysis

To measure the CEST contrast, magnetization transfer ratio asymmetry (MTR$_{asym}$) is calculated. This method allows a simple measurement of CEST contrast by calculating the difference (asymmetry) between the signal intensity at the target offset frequency and the signal at the conjugate frequency.

$$\text{MTR}_{\text{asym}} = \frac{S_{ref} - S_{lab}}{S_O} \qquad (2.6)$$

S_{ref} is the signal intensity at the conjugate frequency, and S_{lab} is the one at the target frequency. S_0 is the signal intensity without the saturation pulses. This method is based on an assumption that the direct water saturation is symmetric so that taking the difference between the target and conjugate frequencies can effectively remove the spillover effect from the direct water saturation[81]. Although this method is a good approach of measuring the CEST contrast when a two-pool (solute and water) model can be established, the Z-spectra acquired in vivo usually contain multiple exchangeable protons, representing various mobile proteins and metabolites[77,82]. For instance, amide (-NH) protons often generate the CEST contrast at 3.5 ppm, and aliphatic protons at -3.5 ppm through relayed nuclear Overhauser ehnacement (NOE) effect[83,84]. In this case, the CEST contrast is generated at both target and the conjugate frequency, and the MTR$_{asym}$ cannot accurately measure the contrast.

To measure the CEST contrast at multiple offset frequencies simultaneously, the full Z-spectrum is often decomposed into multiple Lorentzian functions (**Figure 2.3**) as follows[77].

$$Z(\Delta\omega) = 1 - \sum_{i}^{n} L_i \tag{2.7}$$

$$L_i(\Delta\omega) = A_i \, \frac{\dfrac{\gamma_i^2}{4}}{\dfrac{\gamma_i^2}{4} + (\Delta\omega - \omega_i)^2} \tag{2.8}$$

Z is the full Z-spectrum, and c is the baseline of the spectrum, which is usually set to 1. L_i represents a Lorentzian function for a specific proton pool, which is defined by an amplitude A_i, full width at half maximum γ_i, and an offset from the frequency of water protons ω_i. The Z-spectrum acquired in vivo are often modeled as 5 ~ 7 Lorentzian functions representing amine (-NH_2), amide, water, aliphatic protons and semi-solid macromolecule pools[82,85,86]. The amplitude of each Lorentzian function is assumed to be reflecting the concentration of each exchangeable proton pool.
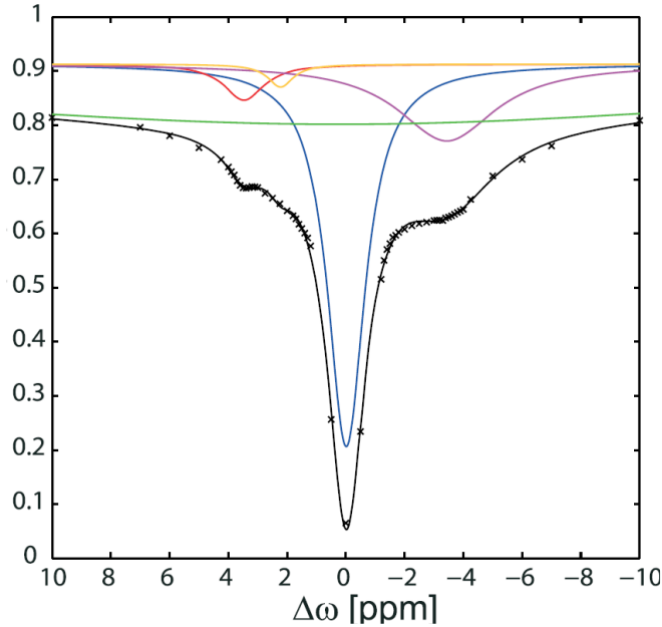
Figure 2.3 Lorentzian decomposition of an *in vivo* Z-spectrum. Multiple exchangeable proton pools including amide (red), amine (yellow), water (blue), aliphatic protons (purple) contribute to the full Z-spectrum, and each can be represented as a single Lorentzian function. Semi-solid macromolecules (green) are also shown as a broad Lorentzian peak. Adapted from ref [82].

Chapter 3. In vivo imaging of urea recycling via CEST MRI

3.1 Synopsis

Renal function is characterized by concentration of urea for removal in urine. We tested urea as a chemical exchange saturation transfer (CEST) MRI contrast agent for measurement of the concentrating capacity of distinct renal anatomical regions. CEST contrast of urea was examined using phantoms with different concentrations and pH levels. Ten C57BL/6J mice were scanned twice at 7T, once following intraperitoneal injection of 2M 150 µL urea and separately following an identical volume of saline. Kidneys were segmented into regions encompassing the cortex, outer medulla and inner medulla and papilla to monitor spatially varying urea concentration. Z-spectra were acquired before and 20 minutes after injection, with dynamic scanning of urea handling performed in between via serial acquisition of CEST images acquired following saturation at +1ppm. Phantom experiments revealed concentration and pH dependent CEST contrast of urea that was both acid and base catalyzed. Z-spectra acquired before injection showed significantly higher CEST contrast in the inner medulla and papilla ($2.3 \pm 1.9\%$) compared to the cortex ($0.15 \pm 0.75\%$, $P = 0.011$) and outer medulla ($0.12 \pm 0.58\%$, $P = 0.008$). Urea infusion increased CEST contrast in the inner medulla and papilla by $2.1 \pm 1.9\%$ (absolute), while saline infusion decreased CEST contrast by $-0.5 \pm 2.0\%$ (absolute, $P = 0.028$ vs. urea). Dynamic scanning revealed that thermal drift and diuretic status are confounding factors. Overall, urea CEST has a potential of monitoring renal function by capturing the spatially varying urea concentrating ability of the kidneys.

3.2 Introduction

Measurement of kidney function is typically performed via either measurement of serum creatinine levels or via estimation of glomerular filtration rate (eGFR).[41,22] While these methods enable easy assessment of the global function of both kidneys and are used to diagnose acute kidney injury (AKI) and chronic kidney disease, neither provide spatial information regarding the extent of kidney damage either within or between kidneys. Further, compensatory hyperfiltration by intact nephrons limits detection of renal failure via measurement of serum creatinine levels or eGFR to cases where kidney function is reduced by more than fifty percent.[87] Non-invasive imaging of renal structure and perfusion is routinely performed using modalities including ultrasound[50], computed tomography (CT)[62] and magnetic resonance imaging (MRI)[88]. Ultrasound is the most widely used for aiding the diagnostic workup of patients with kidney diseases[50] via identification of anatomical abnormalities including altered kidney mass, urinary tract obstruction, and increased echogenicity of renal parenchyma.[67] However, whether anatomical characteristics derived from these images correlate with underlying renal function remains controversial.[50,53] In contrast, measurement of renal perfusion using doppler ultrasound[54], contrast enhanced CT[62], and dynamic contrast enhanced MRI (DCE-MRI) with compartmental modeling[89] have been pursued to assess kidney function. However, perfusion is an indirect indicator of kidney function since renal function can be compromised by parenchymal damage in the presence of preserved renal perfusion. Additionally, many CT and MRI contrast agents are either contraindiciated or considered high risk for patients with insufficient renal function.[60] Finally, while renal scintigraphy

can be used to measure renal blood flow, filtration, and excretion[90], scintigraphy is limited by long scan times, poor spatial resolution and use of radioactive tracers.[91]

Beyond imaging of renal perfusion and GFR, the corticomedullary gradient of the solutes sodium and urea, which regulate water reabsorption and urine concentrating functions of the kidney, have been probed as potential imaging markers of renal function.[92,93] For example, previous studies using Na-MRI demonstrated a maintained intrarenal sodium gradient in kidneys with healthy function[94], and altered intrarenal sodium gradients in diseased kidneys.[95,96] Similarly, significant reabsorption of urea from the inner medullary collecting duct (IMCD) maintains hyperosmolarity in the inner medulla, thereby driving water reabsorption and urine concentration.[97] Measurement of the intrarenal distribution of urea may provide a measurement of renal function, particularly in diseases that alter urea transporter expression or the capacity of the inner medulla to concentrate urea including sepsis induced acute kidney injury.[98]

Chemical exchange saturation transfer (CEST) MRI is an emerging molecular MRI technique that allows for the frequency selective irradation of target protons within specific functional groups including hydroxyl (-OH), amine ($-NH_2$) and amide (-NH) groups and subsequent detection following saturation transfer to the bulk water pool.[74,78,99,100] Urea has 4 identical amine protons that resonate at +1 ppm relative to water, and in fact was one of the first molecules tested in CEST-MRI.[101] The potential use of urea as an endogenous CEST agent for imaging of kidney urea concentration was also demonstrated previously.[102] In this study we examine whether administration of urea can be used to generate dynamic CEST contrast for quantitative imaging of the spatially varying urea concentrating capacity of the kidney. The CEST properties of urea were first assessed using phantom experiments. Next, *in vivo* imaging was performed before and serially after intraperitoneal urea administration. The impact of temperature and B_0 drift during imaging is further examined for the monitoring of dynamic urea handling.

3.3 Materials & Methods

3.3.1 Phantom Experiment

Urea solutions with different concentrations and pH values were prepared. For phantoms with different concentrations, urea (U4883, Sigmal Aldrich, St. Louis, MO) was dissolved in distilled deionized water and pH was adjusted to 6. Concentrations of 100, 200, 400, 600 and 800 mM urea solution were prepared in glass capillary tubes, which were placed in a 2% agar gel. Similarly, 200, 400, and 800 mM urea solutions with different pH values were prepared in NMR tubes and were placed in agar gel. Phantoms were scanned with a 7T preclinical MR system (PharmaScan, Bruker, Ettlingen, Germany) and a 40 mm transmitter/receiver volume coil (Bruker). A gradient echo sequence (TR/TE = 6.4 / 3.1 ms, matrix = 64 × 64, FOV = 35 mm × 35 mm, slice thickness = 3 mm, flip angle = 10º) with saturation preparation (100 Gaussian pulses, peak B_1 = 0.5 μT, pulse duration = 50 ms, duty cycle = 50%, total saturation time = 10 s) at 31 equally distributed offsets from -3 to 3 ppm was used to acquire z-spectra. B0 inhomogeneity was corrected by using a smoothing spline interpolation and an internal referencing method as previously described.[103]

3.3.2 Animal Experiments

All animal experiments were performed in accordance with the Institutional Animal Care and Use Committee (IACUC) guidelines. Ten 9-week-old C57BL/6J mice (5 male and 5 female) were purchased from Jackson Laboratory (Bar Harbor, ME). Mice were anesthetized with $1.5 - 3\%$ isoflurane gas and were kept warm on a heating bed. A PE-10 tube was inserted into the peritoneal cavity before the mouse was transferred into the MR scanner. Each mouse was scanned twice within a one-week interval, first with urea infusion and then with saline. During each scan, respiration rate was monitored and mouse body temperature was maintained at 37 °C using a circulating water bed.

In vivo imaging was performed using the same scanner and coil as those used for phantom experiments. First, T2-weighted images were acquired using a RARE sequence (TR/TE = 2500 / 52 ms, NA = 2, RARE factor = 8, matrix = 256 × 256). Next a gradient echo sequence (TR/TE = 6.4 / 3.1 ms, 2 segments, matrix = 192 × 192, FOV = 35 mm × 35 mm, slice thickness = 2 mm, NA = 1) with saturation preparation (continuous wave pulse, $B_1 = 0.3$ µT, pulse duration = 500 ms) at 21 offsets from -1 to 1 ppm was used to acquire a spectrum necessary for water saturation shift reference (WASSR) correction via calculation of B0 maps.[81,104] Afterwards, a complete CEST-encoded z-spectrum was acquired (70 Gaussian pulses, $B_1 = 0.6$ µT, pulse duration = 50 ms, duty cycle = 50%, total sat time = 7 sec) to generate images ranging from -6 to 6 ppm with 0.2 ppm step size (total scan time = 25 min). Simulation results from both phantom and animal experiment saturation schemes showed similar Z-spectra (Figure 3.1). After acquiring the first z-spectra, dynamic imaging was performed by repeatedly acquiring images with CEST preparation at +1 ppm offset from water over 20 minutes. A separate scan with saturation at -1 ppm was also performed immediately prior to the dynamic scan. During the dynamic scan, an image with CEST preparation at -300 ppm was acquired after every 7 images acquired with CEST preparation at +1ppm in order to perform post-acquisition thermal drift correction. After 5 minutes of dynamic scanning, a bolus of either 150 µL of 2M urea or 150 µL of 0.9% saline was administered through the intraperitoneal infusion line. The amount of urea administered was determined from previous mouse renal physiology studies.[10,105] After 20 minutes of dynamic scanning an additional full Z-spectrum set of CEST-weighted images were acquired (both WASSR and CEST).

3.3.3 Imaging Data Analysis

All imaging data was analyzed using custom-written code in MATLAB (MathWorks, Natick, MA). Regions-of-interest (ROIs) were drawn on a T2-weighted image to segment the cortex, outer medulla and inner medulla and papilla of the kidney. These ROIs were transferred to CEST-weighted images to generate regional z-spectra from each part of the kidney. The z-spectra from each kidney region were fit using a sum of 4 Lorentzian functions representing water, urea, nuclear overhauser effects (NOE) and magnetization transfer (MT) pools:

$$Z(\Delta\omega) = 1 - \sum_{i=1}^{4} L_i \qquad (3.1)$$

18

With

$$L_i = A_i \frac{\gamma_i^2/4}{\gamma_i^2/4 + (\Delta\omega - \omega_i)^2} \tag{3.2}$$

in which A_i, γ_i and ω_i represent amplitude, full width at half maxium (FWHM) and relative resonance frequency of each pool to water respectively.[82]

  Urea CEST contrast was calculated as the asymmetric magnetization transfer ratio (MTRasym) using the following equation:

$$\text{MTRasym } (\%) = 100 \times \frac{S\,(-1\,ppm) - S\,(+1\,ppm)}{S_0} \tag{3.3}$$

in which S_0 represents the signal intensity of a reference image with saturation at +300pm, while S (-1 ppm) and S (+1 ppm) represent the signal intensities from images saturated at -1 ppm and +1 ppm, respectively. For each mouse, voxwel-wise MTRasym maps were calculated and overlaid on T_2-weighted anatomical images to observe the urea CEST effect in each part of the kidney. The change in MTRasym before and after the infusion of either urea or saline was also recorded for each part of the kidney.

3.3.4 Analysis of dynamic urea imaging

  Calculation of MTRasym at each time point during dynamic imaging was performed using equation (3.3) with each +1ppm CEST weighted image, and constant -1 ppm weighted and -300 ppm (S_0) weighted images from prior to infusion. The resultant time curve of MTRasym was normalized by subtracting the average of the first 8 MTRasym values recorded prior to or saline infusion, yielding dynamic measurements of ΔMTRasym. A discrete Gaussain filter was applied to smooth the time curve.

3.3.5 Statistical Analysis

  All statistical analyses were done using Prism 8 (GraphPad Software, San Diego, CA). Normality of the data was confirmed by Shapiro-Wilk test. Two-way repeated measures analyis of variance (ANOVA) was used for comparing the MTRasym change induced by urea and saline infusion, followed by Holm-Sidak post-hoc test. Adjusted p-values of 0.05 or less were considered statistically significant. All the data are expressed as mean ± standard deviation.
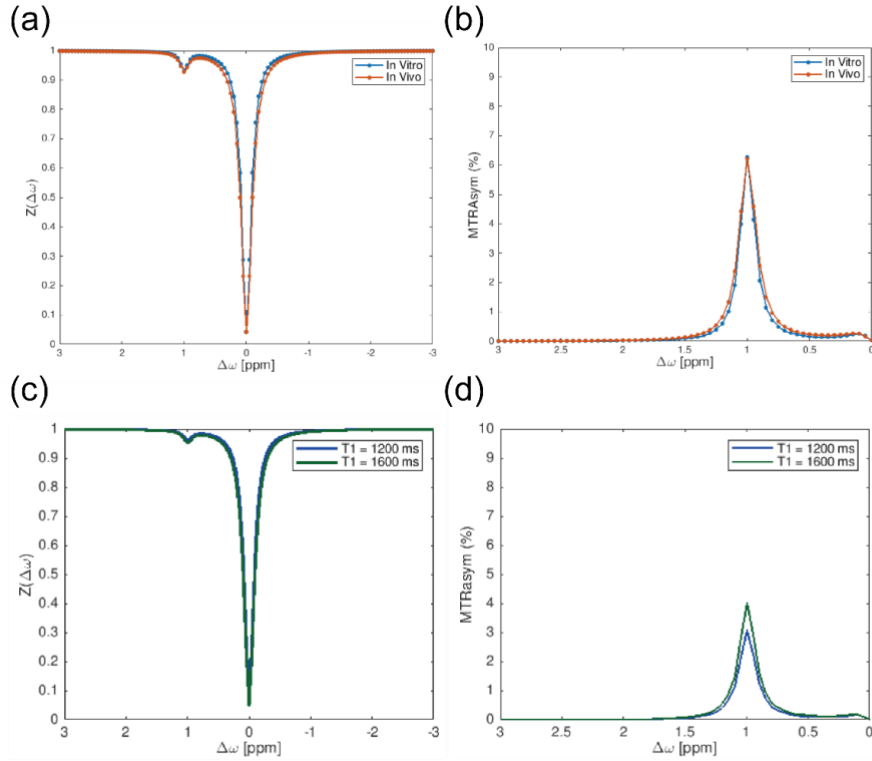
Figure 3.1 Simulation results from saturation schemes that were used for phantom experiments (In Vitro) and animal experiments (In Vivo). (a) Simulated z-spectra with 300 mM urea at 7T. (b) MTR asymmetry calculated from (a). (c) Simulated z-spectra with different T1 values (1200 and 1600 ms). (d) MTR asymmetry calculated from (c) reveal that the increase in native T1 times leads to an increase in MTR_{asym} from 3.1% to 4.0%.

3.4 Results

Phantoms containing urea solution revealed both concentration and pH-dependent CEST contrast at 1ppm (Figure 3.2). In phantoms containing increasing concentrations of urea (100 to 800 mM) at a fixed pH of 6, MTRasym increased linearly from 3.4 to 20.7% as shown in Figure 3.2a – c. Variation of pH at a constant urea concentration of 800 mM demonstrated pH dependent changes in CEST contrast consistent with both acid and base catalysis (Figure 3.2d – f), with MTRasym values that decreased from 17.0 to 7.9% when pH increased from 6.25 to 7, and increased again to 9.8% at pH 7.5. Similar pH-dependence in MTRasym was also observed in 200 and 400 mM urea solutions as shown in Figure 3.2.
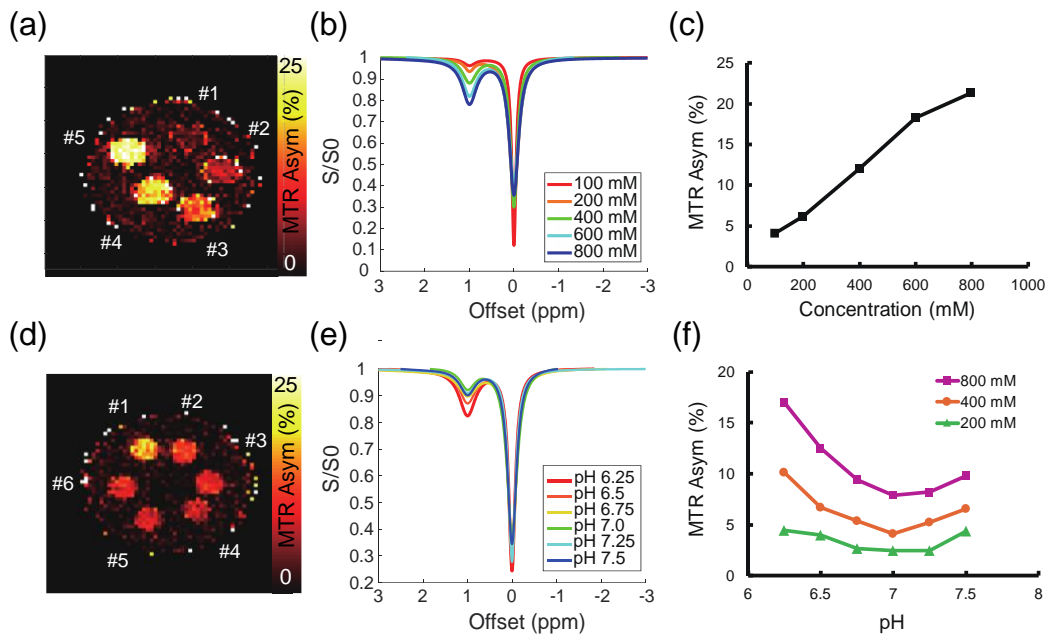
Figure 3.2 Concentration and pH-dependent responses of urea phantoms. (a) MTR asymmetry map of a phantom with different concentrations (#1: 100, #2: 200, #3: 400, #4: 600 and #5: 800 mM) of urea at pH 6. (b) Z-spectra from urea phantoms with different concentrations shown in (a). (c) Concentration-dependent urea MTR asymmetry. (d) MTR asymmetry map of a phantom with different 800mM urea at varying pH (#1: 6.25, #2: 6.5, #3: 6.75, #4: 7.0, #5: 7.25, #6: 7.5). (e) Lorentzian-fitted z-spectra from urea phantoms shown in (d). (f) pH-dependent urea MTR asymmetry at different concentrations.

Representative axial images in a male mouse are shown in Figure 3.3. High resolution T2-weighted images were used to segment three kidney regions: cortex, outer medulla and inner medulla and papilla as shown in Figure 3.3a. Corresponding images acquired without CEST-weighting (Figure 3.3b) and with urea CEST-weighting (1 ppm) prior to urea infusion (Figure 3.3c) demonstrate preserved signal to noise when using peak saturation power of 0.6 μT. Following urea infusion, identical CEST-weighting results in lower signal in the kidneys and liver compared to the pre-infusion image (Figure 3.3d). Representative maps of urea CEST contrast derived from CEST-weighted images are shown in Figure 3.4 with values constrained to within the kidneys. Prior to infusion, modest urea CEST contrast can be observed in the inner medulla and papilla (dashed boundaries). Infusion of urea generates a substantial increase in urea CEST contrast in the inner medulla and papilla that is not observed following saline infusion.
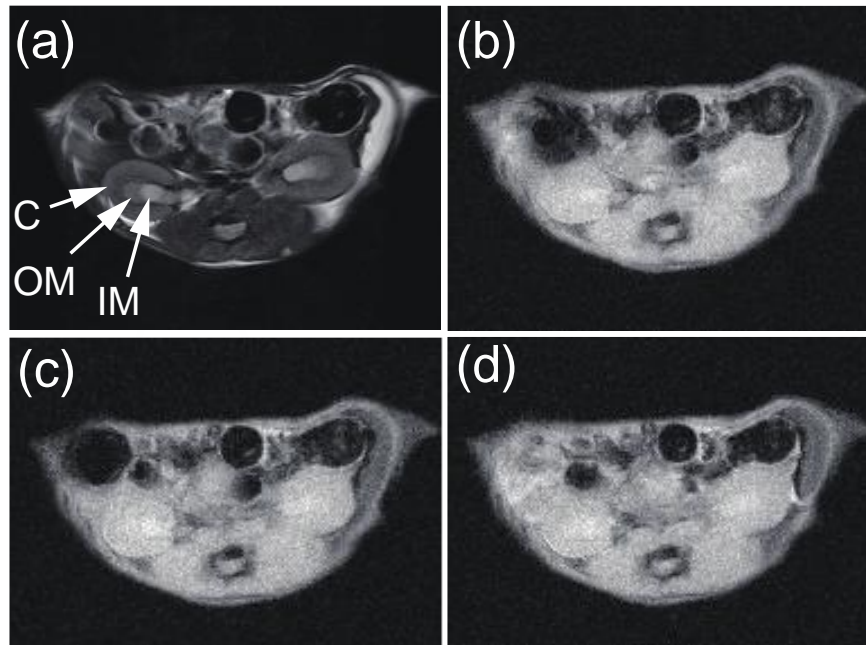
Figure 3.3 Magnitude-reconstructed images of urea-infused mouse. (a) High resolution T_2-weighted anatomical image delineating cortex (C), outer medulla (OM) and inner medulla and papilla (IM+P) of the kidneys. (b) Unsaturated S0 image. (c) Raw CEST image with saturation at 1 ppm before urea infusion. (d) Raw CEST image with saturation at 1ppm after urea infusion.
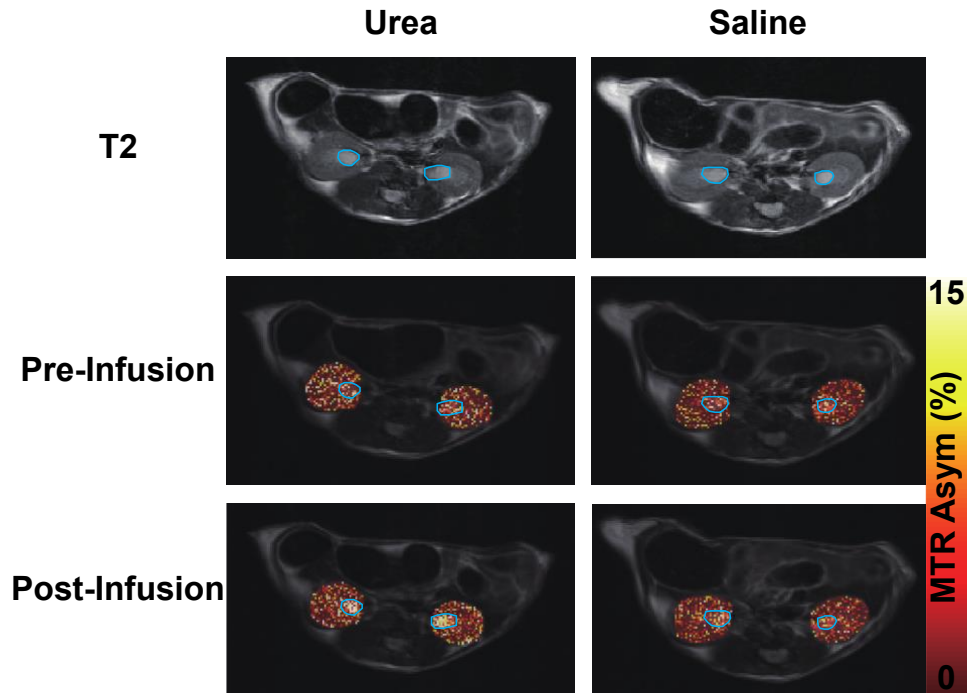
Figure 3.4 In vivo MTR asymmetry maps acquired before and after infusion of either urea or saline. Pseudo color-coded +1 ppm MTR asymmetry maps are overlaid on anatomical T_2-weighted images. The inner medulla and papilla of each kidney is delineated with a blue line. MTR_{asym} values increase significantly in the inner medulla and papilla following urea infusion, but not following saline infusion.

Representative regional z-spectra derived from images acquired before and after urea infusion are shown in Figure 3.5. Prior to urea infusion, saturation transfer at +1 ppm is observed in the inner medulla and papilla, but not the outer medulla or cortex. After urea infusion, saturation at +1 ppm in the inner medulla and papilla is visibly increased, while the cortex and outer medulla do not show any changes in saturation transfer. While baseline saturation transfer at +1ppm was similar in mice that received infusion of saline, infusion of saline did not result in changes in saturation transfer at +1ppm as shown in Figure 3.6. The Lorentzian fitting of Z-spectra also revealed increased MT after urea and saline infusion (Figure 3.7, Table 3.1).
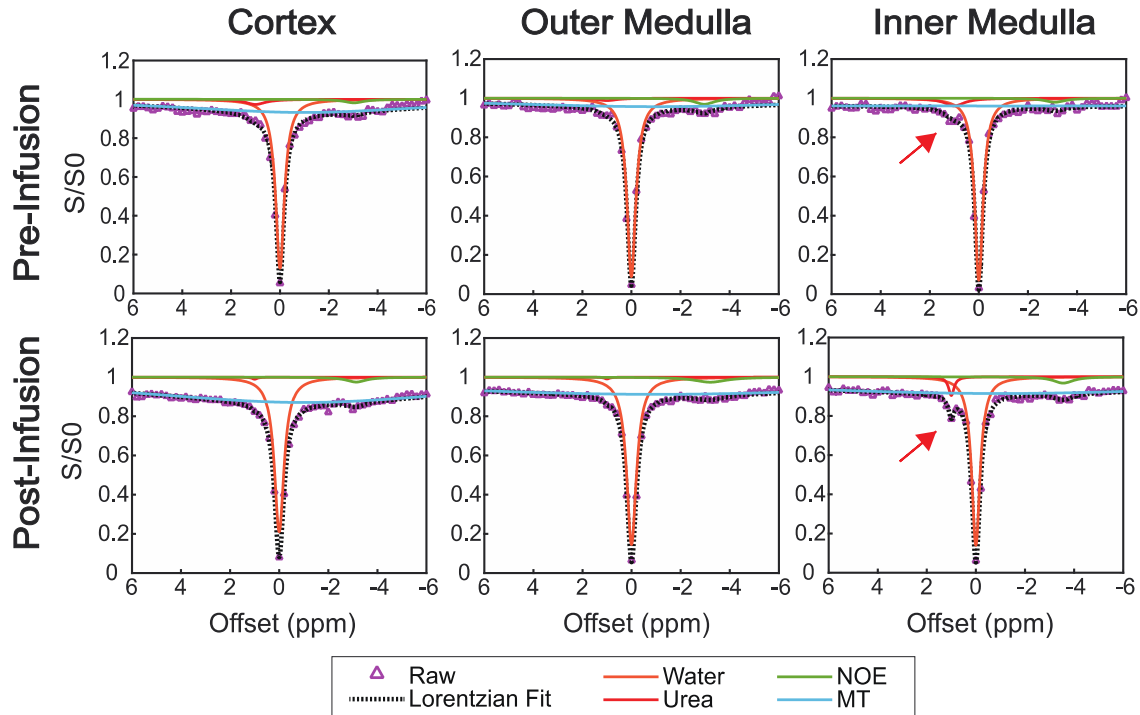
Figure 3.5 Representative z-spectra with 4-pool Lorentzian fitting acquired from each part of the kidney before and after urea infusion. Each Lorentzian function shows the contribution of each pool to the measured z-spectra. Red arrows indicate increased urea CEST contrast at +1 ppm after infusion of urea. Other parts of the kidney do not show changes in saturation transfer at +1ppm.

Regional MTRasym measurements both before and after the infusion of either urea or saline are shown in Figure 3.8. Before urea infusion MTRasym in the inner medulla and papilla $(2.3 \pm 1.9\%)$ was significantly higher than that in the cortex $(0.15 \pm 0.75\%, P = 0.011)$ and outer medulla $(0.12 \pm 0.58\%, P = 0.008)$. After urea infusion, significantly increased MTRasym values were observed in the inner medulla and papilla compared to corresponding pre-infusion values $(4.4 \pm 3.2\%, P = 0.02)$. The increase of urea concentration was further confirmed via measurement of both total kidney homogenate urea content and post-infusion urine urea concentration (Figure 3.9). In contrast, values in the cortex $(0.67 \pm 0.65\%, P = 0.17)$ and outer medulla $(0.61 \pm 0.66\%, P = 0.17)$ did not change significantly following urea infusion (Figure 3.8a). The difference in MTRasym between the inner medulla and papilla and other regions increased significantly following urea infusion $(P = 0.009$ vs. cortex; $P = 0.008$ vs. outer medulla). When the same mice

were imaged one week later for infusion of saline, similar pre-infusion MTRasym values were measured in the inner medulla and papilla (2.7 ± 2.2%), cortex (0.54 ± 1.2%, P = 0.045 vs. inner medulla and papilla) and outer medulla (0.33 ± 0.55%, P = 0.015 vs. inner medulla and papilla) as shown in Figure 3.8b. After saline infusion, MTRasym values were unchanged from pre-infusion values in the cortex (0.67 ± 1.0%, P = 0.835 vs. pre-infusion), outer medulla (0.33 ± 0.68%, P = 0.992 vs. pre-infusion), and inner medulla and papilla (2.2 ± 2.6%, P = 0.835 vs. pre-infusion). When normalized for pre-infusion urea CEST contrast, ΔMTRasym values in the cortex (0.13 ± 0.71% saline vs. 0.52 ± 1.1% urea, p = 0.362) and outer-medulla (0.002 ± 0.57% saline vs. 0.49 ± 0.82% urea, p = 0.226) were greater following urea injection but failed to reach statistical significance (Figure 3.8c). However, significantly different ΔMTRasym values in the inner medulla and papilla were observed between saline (-0.50 ± 2.0%) and urea (2.1 ± 1.9%, p = 0.028 vs. saline) infusions.
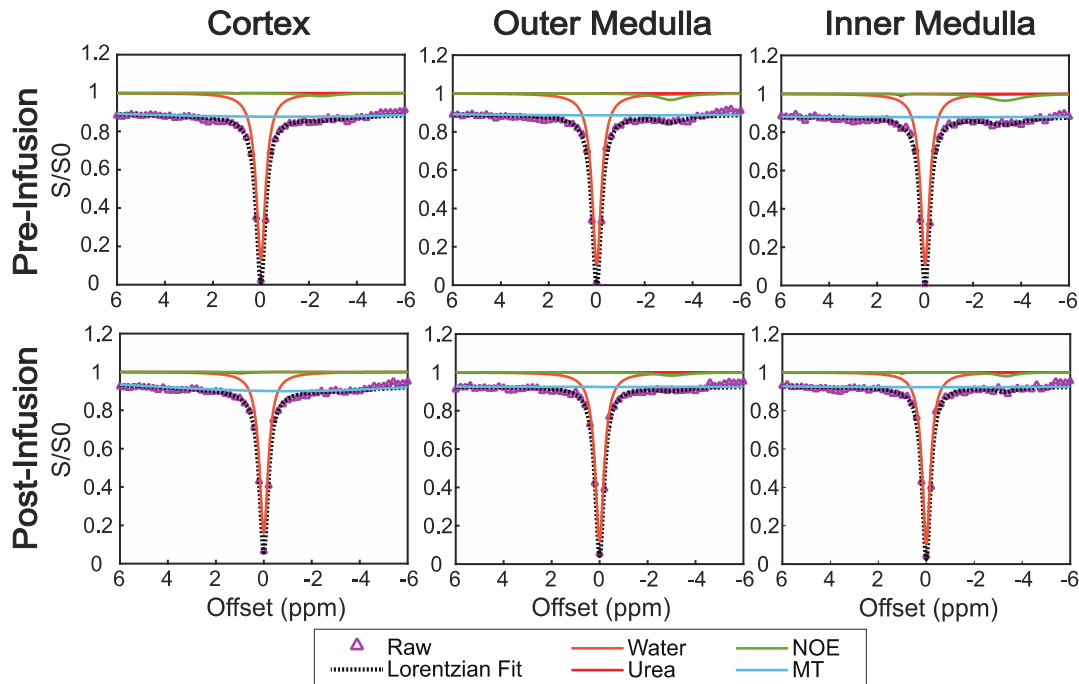
Figure 3.6 Representative z-spectra with 4-pool Lorentzian fitting acquired from each part of the kidney before and after saline infusion. Saline adminsitration did not generate any difference in z-spectra, including the inner medulla. The red arrow in the inset in pre-infusion inner medullary z-spectra (top right) indicates the urea contrast at 1 ppm.

Dynamic urea-enhancement imaging was performed by repeatedly acquiring +1ppm CEST-weighted images following infusion of either urea or saline. Calculation of regional urea CEST-contrast via comparison of such images to -1ppm and S_o images acquired prior to infusion reveals a dynamic increase in CEST contrast in all three anatomical regions that is highest in the inner medulla and papilla (Figure 3.10). However, repeated imaging of the same anatomical position with RF irradiation at +1ppm induces drift in the signal intensity of non-CEST weighted (S_o) images as shown in Figure 3.10b. Calculation of dynamic urea-enhancement using normalization to S_o images acquired after every seven +1ppm weighted images eliminates changes in urea CEST contrast in the cortex and outer medulla (Figure 3.10c). In addition, urea CEST-

contrast in the inner medulla and papilla reaches a plateau approximately 500 seconds after the infusion of urea (Figure 3.10c). Importantly, even after correction for S_o drift the results of dynamic urea enhancement were variable, with some mice generating enhancement patterns that failed to stabilize as shown in Figure 3.10d.
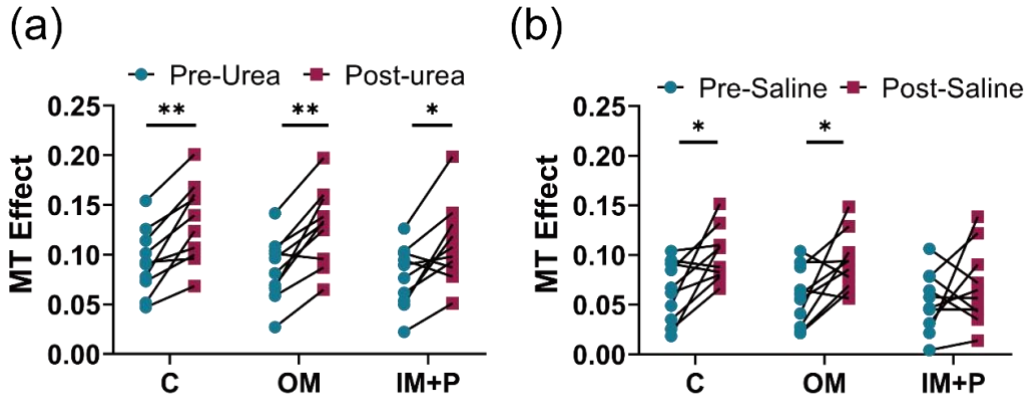
Figure 3.7 Magnetization transfer (MT) effect measured by Lorentzian fitting before and after injection of either (a) urea or (b) saline (**P < 0.01, *P < 0.05).

	Urea			**Saline**		
	Pre-injection	Post-injection	P-value	Pre-injection	Post-injection	P-value
C	0.093±0.033	0.132±0.04	0.0015	0.063±0.03	0.101±0.027	0.035
OM	0.085±0.032	0.129±0.039	0.0013	0.058±0.03	0.092±0.029	0.044
IM+P	0.078±0.031	0.111±0.041	0.0136	0.053±0.03	0.068±0.039	0.358

Table 3.1 Statistical analysis of data shown in Figure 3.7.

3.5 Discussion

In this study, we demonstrated the feasibility of using urea as a CEST agent for imaging the urea concentrating capcaity of the kidney inner medulla. Phantom experiments were used to establish the concentration and pH-dependent CEST effects of urea in physiological conditions at 7T. Separately, *in vivo* z-spectra acquired before and after intraperitoneal infusion of either saline or urea revealed inner medulla-specific enhancement of CEST contrast at +1 ppm after urea infusion. Voxel-wise calculation of MTRasym at +1ppm revealed spatial enhancement of urea CEST contrast in the inner medulla and papilla in response to urea infusion.

Urea is filtered across the glomerulus in the cortex, further concentrated via active sodium transport driven water reabsorption in the tubular system, and significantly reabsorbed at the IMCD through urea transporters UT-A1 and UT-A3. The capacity to concentrate urea at the inner medulla is a key measure of kidney function. In agreement with prior studies by Dagher et al.[101] and Vinogradov et al.[102], we observed baseline urea CEST contrast in the inner medulla of all mice. Prior studies have used intravenous injection of 150 mM hyperpolarized ^{13}C-labeled urea in

combination with ^{13}C-MRI to probe the urea concentrating capacity of the medullary compartment of the kidney via measurement of a sequentially increasing ^{13}C signal between the cortex and medulla in rats.[93] While the ^{13}C signal of the cortex plateaud within 15 seconds of urea injection, the medullary signal gradually increased throughout the imaging window of 50 seconds under normal physiological conditions, and increased faster following antidiuretic stimulation. In a similar study performed by Reed et al.[106], multiexponential analysis revealed that extraction of ^{13}C urea to the extravascular space can be assessed by quantification of the long T2 relaxation time (> 2.5 sec) component fraction. These findings confirm that imaging of urea reflects the underyling function of urea transporters in the medullary compartment at large. When using hyperpolarized imaging to probe kidney urea concentrating activity, an intravenous injection and lower relative spatial resolution are used in order to obtain as much dynamic data as possible given the constraints imposed by loss of hyperpolarization. In contrast, urea CEST-MRI can be used to acquire higher spatial resolution images that enable differentiation of different regions of the medulla. However, urea CEST-MRI requires several seconds of RF irradiation to weight the initial longitudinal magnetization and is further constrained by T_1 relaxation during data acquisition. Subsequently, we utilized an intraperitoneal injection of urea for slower delivery to the kidney and to enable measurement of changes in regional urea CEST contrast. Our findings of increased urea CEST contrast in the inner medulla following intraperitoneal injection mirrors the urea concentrating patterns observed in the aforementioned studies, but highlights the unique concentrating capacity of the inner medulla. Importantly, in order to perform dynamic urea CEST imaging, post injection Z-spectra were only acquired 20 minutes after urea injection, potentially limiting our measurement of an absolute change in urea CEST contrast in the inner medulla that may have peaked earlier after urea infusion. The time course of urea concentration change in the urine after urea injection (Figure 3.9) also suggests that the CEST contrast at 1 ppm could be affected by variations in the urea concentration during the Z-spectra acquisition, which took 25 minutes.

Dynamic imaging of urea CEST contrast was performed in this study in an attempt to quantify the kinetics of urea handling, transport, and concentration of the kidney. Even before the infusion of urea, a steady increase of MTRasym was observed in all parts of the kidney, which continued during urea infusion (Figure 3.10a). In order to determine whether hydration conditions may have contributed to this drift, dynamic CEST imaging of the brain was performed and demonstrated a similar drift in MTRasym (Figure 3.11). These findings suggest that the hydration condition of tissue was not a cause of MTRasym drift. Measurement of the sigal intensity on a non-CEST weigthed reference (S_0) image during the same period revealed a steady decrease over the dynamic scan timeframe (Figure 3.10b). This phenomena was previously reported by Desmond et al., which showed an exponential decrease in S_0 image signal intensities due to thermal drift, likely caused by repeated RF irradiation required for CEST contrast generation.[107] Subsequently, CEST contrast that is repeatedly calculated from steadily decaying CEST-weighted images and a single S_0 image acquired at the start of a dynamic study will not accurately reflect the CEST contrast generated by urea. In order to correct for this drift we acquired S_0 images at fixed intervals during dynamic scanning and calculated CEST contrast using each S_0 image for a fixed window of weighted images. Subsequent dynamic measurements of MTRasym revealed inadequate sensitivity to monitor changes in urea concentration in the cortex and outer medulla when using an intraperitoneal infusion protocol. Measurement of complete Z-spectra after infusion confirmed the absence of detectable urea CEST contrast in the same two regions, suggesting that such correction eliminated falsely elevated regional urea CEST contrast values seen in initial dynamic scanning results. Importantly, even after correction, the results of dynamic urea CEST imaging

remained mixed. While several mice demonstrated enhancement of urea CEST contrast with a steady state plateau following infusion (Figure 3.10c), others demonstrated rapid enhancement and loss of urea CEST contrast (Figure 3.10d). Further, while accounting for thermal drift, dynamic imaging does not correct for B_0 field drift, which has previously been shown to generate a significant artifact in dynamic CEST imaging.[108,109] In contrast, the acquisition of complete Z-spectra removes the influences of the aforementioned processes, however at the cost of scan times that are not suitable for dynamic imaging.
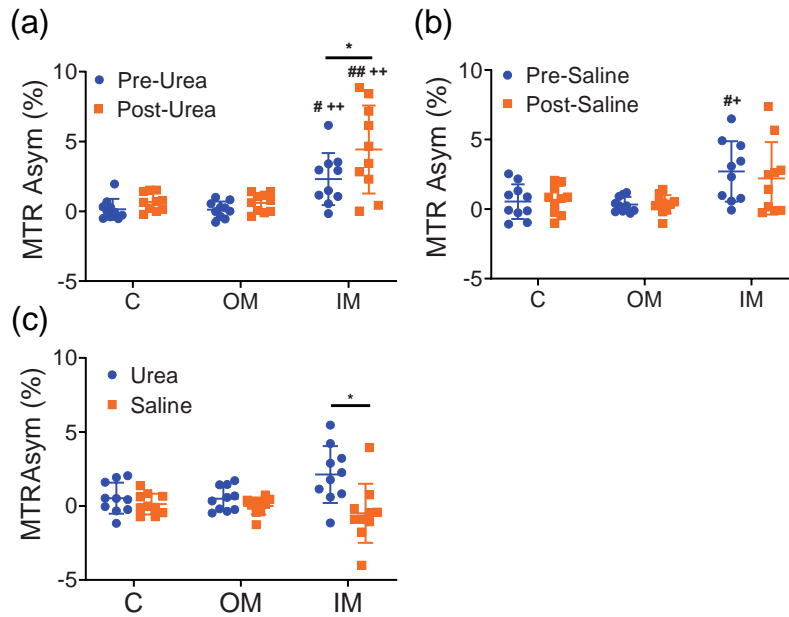
Figure 3.8 (a) MTR asymmetry (MTRasym) measured from each region of the kidney before and after the infusion of urea. (b) MTRasym measured before and after the infusion of saline. (c) The change in MTRasym following infusion of urea was greatest in the inner medulla and papilla. No changes in MTRasym were observed following saline infusion. *P < 0.05, #P < 0.05 vs. cortex (C), ##P < 0.01 vs. C, +P < 0.05 vs. outer outer medulla (OM), ++P < 0.01 vs. OM.
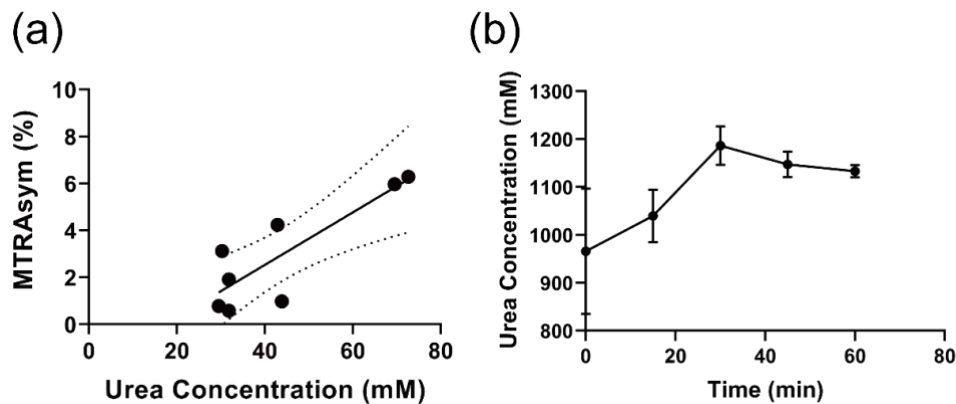
Figure 3.9 Validation of urea concentration and MTR asymmetry measurement. (a) Correlation of urea concentration in kidney homogenate and MTR asymmetry measured in the inner medulla and papilla after urea infusion ($R^2 = 0.726$, P = 0.0072). (b) Urea concentration measured from mouse urine before (t = 0) and after urea infusion.
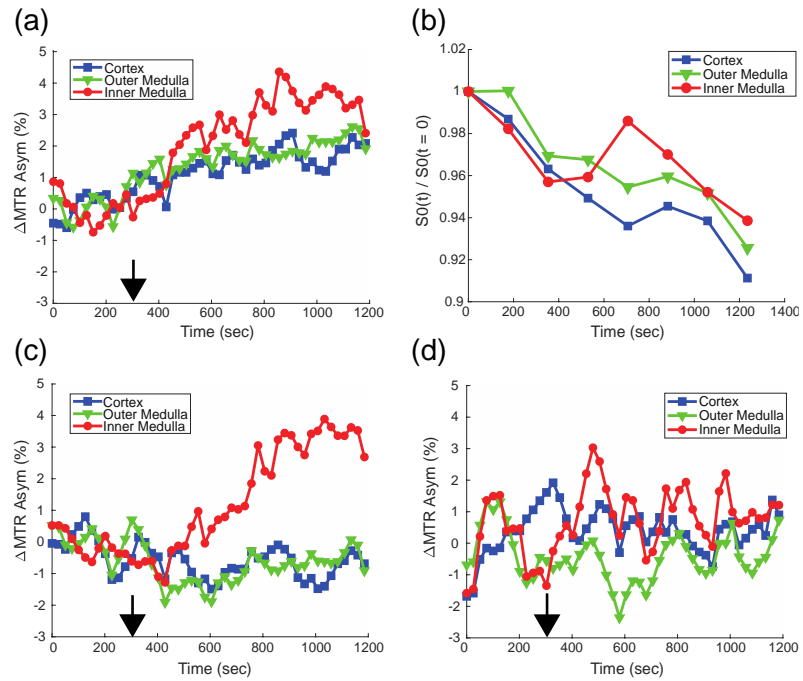
Figure 3.10 Dynamic time curves of MTR asymmetry change and S_0 image signal intensity in each part of the kidney. (a) Dynamic measurement of MTR_{asym} without thermal drift correction reveals a steady increase in MTR_{asym} in each part of the kidney following urea infusion. (b) Normalized signal intensities of S_o images acquired during dynamic scanning reveal a time dependent decrease in S_o values, likely due to thermal drift. (c) When dynamic MTR_{asym} measurements from (a) are corrected for thermal drift by accounting for the decrease in S_o image signal intensities over time (b), changes in MTR_{asym} are only observed in the inner medulla and papilla. (d) While such correction enabled dynamic measurement in some mice, others still demonstrated highly noisy dynamic measurements with early peaks in inner medulla and papilla MTR_{asym} and rapid declines. Black arrows indicate the time point when the urea infusion was made.

Urea CEST contrast measured in both the cortex and outer medulla was minimal either before or after urea infusion. Phantom experiments revealed a urea CEST detection threshold of 100-200 mM at physiological pH levels (Figure 3.2). However, the plasma concentration of urea in the cortex is between 5 to 10 mM.[9] Although urea concentration increases in the tubule due to water reabsorption, the low urea permeability in the outer medulla limits the concentration gain only to the intraluminal pool.[97] Renal CEST imaging using iopamidol[110–113] has been extensively performed for estimation of the intranreal pH gradient, which has been shown to decrease from pH 7.0 in cortex to 6.6 in the inner medulla.[110] At pH 7.0, the exchange rate of urea protons enters the slow exchange regime.[114] The combination of lower concentrations and slow exchange rate thus make detection of urea CEST contrast with pulsed CEST-MRI highly unlikely in the cortex and outer medulla. In contrast, the tubular urea concentration is significantly increased as filtrate approaches the inner medulla and is transferred to the interstitium due to the high urea permeability. Subsequently, the concentration of urea increases to the range of several hundred millimolar[98] and enters the detectable concentration range for pulsed CEST-MRI. Further, urea is both acid and base catalyzed[114], increasing the exchange rate of urea protons to the intermediate range in the more acidic environment of the inner medulla. Our findings suggest that fast exchange-sensitive approaches such as variable delay multiple pulse (VDMP) CEST-MRI, T1rho imaging, or T2-

exchange methods may be more appropriate for measurement of urea handling in the cortex and outer medulla.[115,116] These approaches may be also useful for isolating urea CEST contrast from other metabolites in the kidney that produce CEST effect at the same offset.[117]
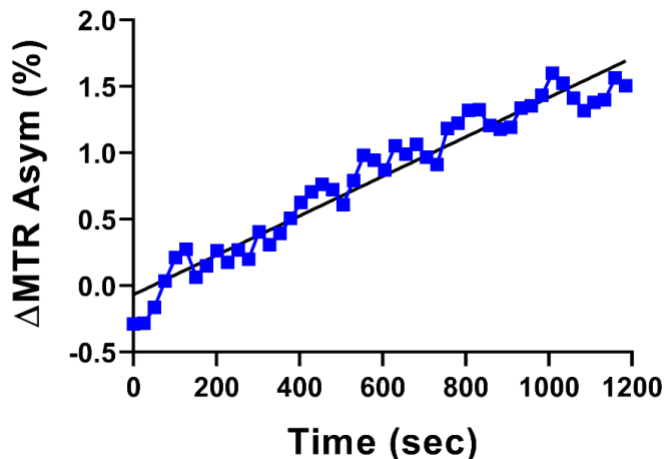
Figure 3.11 A representative dynamic time curve of MTR asymmetry change acquired from the mouse brain. Dynamic CEST scans of the brain were performed on three additional mice in order to examine whether MTR_{asym} signal drift observed in the kidney would be replicated in an organ not susceptible to hydration changes. The same saturation parameters were used as for kidney imaging with a different readout protocol (TR/TE = 9.0/3.1 ms, Matrix = 128 × 128, FOV = 28 mm × 28 mm, FA = 20°). Neither urea nor saline were infused. An average increase in MTR_{asym} of 1.72 ± 0.10 % (absolute) over 20 minutes was observed (n = 3 mice) in the brain. Linear fitting of acquired dynamic curves (black line) had an average slope of $(1.081 \pm 0.372) \times 10^{-3}$ %/sec.

Phantom experiments showed that urea CEST contrast is dependent on both concentration and pH, which may confound the quantification of urea in the kidney. Importantly, urea CEST contrast varied over the relevant physiological range of kidney pH (6.5 - 7.4), suggesting that changes in MTRasym between pre- and post-infusion may have been affected by variations in pH. The pH effect will be more confounding in the case of diseased kidneys with altered pH. In addition to pH, differences in T1 relaxation times between kidney regions can influence subsequent measurements of urea CEST contrast. For example, prior studies at 7T have reported T1 times of approximately 1200 ms in the cortex and approximately 1600 ms in the medulla.[118] Longer T1 times within tissue will result in enhanced CEST contrast due to sustained spin saturation in comparison to tissue regions with shorter T1 times. Simulation of the effect of lengthened T1 times (Figure 3.1) reveals an increase in urea CEST contrast of 0.9% (absolute) for the aforementioned T1 times at constant urea concentration and pH. Our results suggest that in future studies, measurement of urea CEST contrast between each part of the kidney should utilize T1-correction methods such as apparent exchange-dependent relaxation (AREX) in order to isolate differences in CEST contrast attributable to changes in urea concentration alone.[119]

The use of urea as a common food additive, and the endogenous capacity of the kidney to concentrate and remove urea from blood are advantageous for the application of urea as a CEST contrast agent. However, unlike iodinated contrast agents or ^{13}C based tacers that have no spectral background signal, the resonance frequency of the target amine protons within urea is only separated by 1 ppm from the resonant frequency of water and within the spectral range of other endogenous metabolites. Subsequently, the design of saturation schemes should be optimized to

minimize direct water saturation both through necessary reduction in peak saturation power and the bandwidth of saturation pulses. Additionally, since urea also has a slow exchange rate at physiological pH[114], saturation at 1ppm requires the use of RF pulses with weak amplitude for a longer duration than comparable iodinated agents. Subsequently, acquisition of compelte Z-spectra requires longer experimental times and is more influenced by temperature and B_0 drifts over time. This represents a potential limitation to human application, where additional concerns regarding reduced spectral separation of urea and water at of lower B_0 fields and increased spatial B_1 inhomogeneity further complicate interpretation of urea CEST images.[120] Given these limitations, the use of urea CEST may be limited to probing discrete urea concentrating activities of kidneys, as opposed to measurement of dynamic processes.

Several limitations to this study merit further discussion. First, since the study was designed to probe dynamic urea enhancement in the kidney, acquisiton of post-infusion Z-spectra took place 20 minutes after cessation of infusion. Subsequently, the peak change in MTRasym measured in the inner medulla and papilla was likely below the maximum peak contrast that could be generated following urea infusion. Given that our results suggest that dynamic imaging of urea CEST contrast may not be possible, future studies could probe an alternative late ehancement approach, analogous to that employing gadolinium for scar imaging, where Z-spectra are acquired at a fixed time after intravenous injection of urea that corresponds to the timepoint of maximal urea concentration in the inner medulla. Second, in comparison to previous dynamic CEST imaging studies performed in the brain[121,122], dynamic imaging in the kidneys may be affected by peristalsis of the digestive tract, or physiological responses to anesthesia. Lastly, the diuretic states of mice were not controlled in this study, which can significantly impact the urea permeability of the inner medulla. The expression levels of the urea transporters UT-A1 and UT-A3 in the inner medullary collecting duct (IMCD) can vary dynamically by up to 400% depending upon diuretic state.[123] In the antidiuretic state, urea transporters are expressed at a higher density in the IMCD. Subsequently, significantly more urea accumulates in the inner medulla concomitant with greater water reabsorption, leading to higher urea concentration in the IM. During diuresis, UT-A1 and A3 levels decrease and less urea accumulates in the IM. Since diuretic state was not controlled in this study, it is likely that we observed higher variability of urea concentration in the IM both before and after infusion of either urea or saline than would be observed in studies where diuretic state is tightly controlled prior to imaging. Further, the subsequent changes in T1 and T2 times of urine based on urea concentration may also have contributed to the variability in observed urea CEST contrast. Variable diuretic states between mice, or within an imaging session, would have influenced both the baseline urea MTRasym measurement and the change in this measurement following infusion of either urea or saline.

3.6 Conclusion

In this study, we presented the feasibility of utilizing urea as a CEST contrast agent for probing renal function with spatial specificity. Concentration and pH-dependent CEST effects of urea in physiological condition were characterized through phantom experiments. In parallel to established kidney physiology and previous urea imaging studies[93,101,102,106], this study confirmed the capacity of CEST-MRI to detect changes in urea concentration in the inner medulla of the mouse kidney. While dynamic imaging of urea handling would provide substantial benefit, confounding factors including S_o drift and tight diuretic control need to be considered.

Chapter 4. Technical Optimization: Delayed urea differential enhancement CEST (dudeCEST)-MRI

4.1 Synopsis

We demonstrate a method of delayed urea differential enhancement CEST (dudeCEST) for probing urea recycling action of the kidney using expanded multi-pool Lorentzian fitting and apparent exchange-dependent relaxation (AREX) compensation. T_1 correction of urea CEST contrast by AREX was tested in phantoms. Nine mice were scanned at 7T following intraperitoneal injection of 2M 150 μL urea, and later saline. T_1 maps and Z-spectra were acquired before, and 20 and 40 minutes post-injection. Z-spectra were fit to a 7-pool Lorentzian model for CEST quantification and compared to urea assay of kidney homogenate. Renal injury was induced by aristolochic acid in seven mice and the same scan protocol was performed. AREX corrected for variable T_1 times in phantoms. Urea CEST contrast at +1 ppm increased significantly at both time points following urea injection in the inner medulla and papilla. When normalizing the post-injection urea CEST contrast to the corresponding baseline value, both urea and saline injection resulted in identical fold changes in urea CEST contrast. Urea assay of kidney homogenate showed a significant correlation to both AREX ($R^2 = 0.4687$, $P = 0.0017$) and non-T_1-corrected Lorentzian amplitudes ($R^2 = 0.4964$, $P = 0.0011$). Renal injury resulted in increased T_1 time in the cortex and reduced CEST contrast change upon urea and saline infusion. Overall, delayed urea enhancement following infusion can provide insight into renal urea handling. In addition, changes in CEST contrast at 1.0 ppm following saline infusion may provide insight into renal function.

4.2 Introduction

Renal function is assessed through the measurement of serum and urine biomarkers, such as creatinine, and subsequent estimation of glomerular filtration rate. These approaches enable rapid assessment of overall renal function and are widely used for the diagnosis of major renal diseases such as acute kidney injury (AKI) and chronic kidney disease (CKD).[22,41] However, these methods do not provide spatial information on the extent of the injury, and the compensatory hyperfiltration by intact nephrons often limits the detection of renal failure until 50% of the function is lost.[87] Therefore, invasive biopsies are often needed for detection and monitoring of gradual and progressive renal function loss in cases such as human immunodeficiency virus-associated nephropathy[124] and post-transplantation allograft failure.[35,125] Non-invasive imaging methods that can quantitatively measure renal function may address the aforementioned challenges by providing spatially specific renal function measurements without repetitive biopsies. Medical imaging modalities including ultrasonography,[50] CT,[62] and MRI[88] are widely performed and studied for this purpose, but currently, these are limited to observing structural or perfusion abnormalities, which do not always correlate with underlying renal function.[53,67]

The corticomedullary gradient of the solutes in the kidney is another potential imaging marker of renal function. Urea is a major component of the solutes that form a corticomedullary gradient, comprising 50% of the hyperosmolarity in the inner medulla through urea transporter-mediated recycling.[8] The significant reabsorption of urea in the inner medullary collecting duct (IMCD) drives water reabsorption and consequently urine concentration.[97] The disruption of the

intrarenal urea gradient was observed in sepsis-induced AKI mouse models, in which the urea transporter expression was altered.[98] Similarly, hyperpolarized MRI with ^{13}C-labeled urea as a contrast agent revealed compromised urea gradients within the kidneys of mice with diabetic nephropathy.[126]

Chemical exchange saturation transfer (CEST) MRI is a molecular MRI technique that allows the detection of specific exchangeable protons[74,78,127] including 4 chemically identical amine protons on urea[101]. Recently, we showed that CEST-MRI can be used to monitor the intrarenal gradient of urea and quantify the accumulation of additional urea following infusion in the inner medulla and papilla (IM+P).[128] However, dynamic urea enhancement CEST imaging proved challenging as the rate of enhancement was variable, and differences in T_1 times and the exchange rate of protons were not accounted for. Among these factors affecting CEST contrast, changes in T_1 times is an especially crucial factor to be corrected as distinct anatomical regions in the kidney have significantly different T_1 values.[118] Further, dynamic CEST-MRI during urea infusion caused significant variability presumably due to B_0 field shift and thermal drift.[108,109,128]

Delayed contrast enhancement approaches are commonly used to limit the impact of variable contrast agent delivery. Here, we propose an approach of delayed urea differential enhancement CEST (dudeCEST) with T_1 correction via measurement of the apparent exchange dependent relaxation (AREX)[119]. The feasibility of applying AREX for T_1 correction was first tested in urea phantom experiments. In vivo imaging was performed before, 20 minutes after, and 40 minutes after either urea or saline administration to observe the CEST contrast change over time. The CEST contrast quantification was validated by the urea assay of kidney homogenate after the last scan. The potential application of this method to kidney disease was also tested in a renal injury mouse model.

4.3 Materials & Methods

4.3.1 Phantom Experiment

Urea solutions with different T_1 relaxation times were prepared. Urea (U4883; Sigma Aldrich, St. Louis, MO) was dissolved in phosphate buffered saline, achieving 500 mM concentration and mixed with different amounts of gadolinium chelate (0, 0.05, 0.075, 0.1, 0.2 and 0.5 mM; Magnevist) to generate T_1 values that ranged from 500 ms to 3500 ms. NMR tubes filled with these T_1-adjusted urea solutions were placed in 2% agar gel. Phantoms were scanned with a preclinical MR system (PharmaScan; Bruker, Ettlingen, Germany) at 7T with a 40-mm transmitter/receiver volume coil (Bruker, Billerca, MA). A gradient-echo sequence (TR/TE = 6.4/3.1 ms. Flip angle = 10º, Matrix = 192 × 192, FOV = 3.5 cm × 3.5 cm, Slice thickness = 2 mm, In-plane resolution = 182 μm× 182 μm) with saturation preparation (70 Gaussian pulses, B_1 = 0.6 μT, pulse duration = 50 ms, duty cycle = 50%, total sat time = 7 sec) at 61 offset frequencies from -50 to +50 ppm was used to acquire Z-spectra. Pre-infusion Z-spectra were acquired from +50 to -50 ppm in decreasing frequency order, and two post-infusion Z-spectra were acquired in the opposite direction. The scan time for each offset image was approximately 13 seconds, which resulted in a total scan time of 13 min 28 sec for a full z-spectrum. T_1 maps were acquired by an inversion recovery sequence with a single-shot gradient-echo readout (Inversion times: 100, 200, 400, 600, 800, 1000, 1400, 1800, 2200, 3000, 4000, 5000, 6000, 7000, 8000 ms; TR/TE = 4.3/2.1

ms, Flip angle = 10º, Matrix = 192 × 192, FOV = 3.5 cm × 3.5 cm, Inversion recovery time = 8 sec, In-plane resolution = 182 μm× 182 μm).

4.3.2 Animal Experiments

All animal experiments were performed in accordance with the Institutional Animal Care and Use Committee guidelines. Nine 8 – 12-week-old male C57BL/6J mice were purchased from Jackson Laboratory (Bar Harbor, ME). Mice were anesthetized with 1.5% ~ 3% isoflurane gas on a heating bed. A PE-10 tube was inserted into the peritoneal cavity for infusion of urea and saline during the scan, and the mouse was transferred for imaging using identical instrumentation as previously described. Each mouse was scanned twice within a 5 – 10 day interval, once with the injection of urea (150 μL, 2M) and the other with saline (150 μL). Imaging consisted of the acquisition of a T_2-weighted image (RARE factor = 8, TR/TE = 2500/52 ms, Matrix = 256 × 256, FOV = 3.5 cm × 3.5 cm, In-plane resolution = 137 μm× 137 μm, number of average = 2), a T_1 map, an unsaturated image, and CEST-weighted images (same parameters as phantom experiments) that were acquired before injection, and 20 and 40 minutes post-injection. All mice were euthanized immediately after the second scan (n = 5 for saline scan and n = 4 for urea scan). Kidneys were harvested and homogenized to determine total urea content through an assay (QuantiChrom Urea Assay Kit, BioAssay Systems, Hayward, CA).

To test the feasibility of the dudeCEST method in a disease setting, renal injury was induced in seven additional mice using aristolochic acid (AA) as previously described[129]. Briefly, mice received intraperitoneal injection of 5 mg / kg body weight AA (Acros Organics, Geel, Belgium) dissolved in a 1:1 mixture (volumetric) of H_2O and polyethylene glycol (Acros Organics). AA was administered every 24 hours up to 7 days before the MR scan. MR scan protocols and parameters were same as those for normal mice, with three mice infused with urea and four mice infused with saline during the scan.

4.3.3 Imaging Data Analysis

All acquired images were analyzed by a custom-written code in MATLAB (Mathworks, Natick, MA). For B_0 correction, two-pool (water and semi-solid macromolecules) Lorentzian fitting was applied for each Z-spectrum from a single voxel after excluding offset frequencies of ±1 ~ ±5 ppm.[86] The cortex, outer medulla (OM) and inner medulla and papilla (IM+P) were segmented on T_2-weighted images. Region-of-interest (ROI)-averaged Z-spectra from each kidney region were analyzed for measuring CEST contrast. Before Lorentzian fitting, consistent signal drift was corrected by fitting a biexponential function to the signals acquired with saturation at ±20, ±30, ±40, ±50 ppm, normalized to the signal intensity of the first image (+50 ppm for pre-infusion Z-spectra and -50 ppm for post-infusion Z-spectra). This biexponential interpolation generated a correction factor for each offset frequency image.[107] After the signal drift correction, two-step seven-pool Lorentzian fitting was performed, with each pool representing water, urea, amine group, amide group, semi-solid macromolecules (MT), nuclear Overhauser effect (NOE) around -3.5 ppm or NOE around -1.6 ppm (NOE2).

In the first step fitting, three-pool (water, MT and urea) Lorentzian fitting was applied after excluding data points at offset frequencies of -5 ~ -0.6 ppm and +1.6 ~ +5 ppm.

$$Z(\Delta\omega) = c - \sum_{i}^{n=3} L_i$$

With

$$L_i(\Delta\omega) = A_i \; \frac{\frac{\gamma_i^2}{4}}{\frac{\gamma_i^2}{4} + (\Delta\omega - \omega_i)^2}$$

c is the baseline of the Z-spectrum, which was set to the average of Z(+50 ppm) and Z(-50 ppm). Each Lorentzian function, representing a specific pool i (L_i), is defined by an amplitude A_i, full width at half maximum γ_i, and an offset from the frequency of water protons ω_i.

After the first fitting, offset frequencies that were excluded were re-introduced and seven-pool Lorentzian fitting was applied. During this process, Lorentzian function parameters determined from the first step fitting were fixed except the amplitude of the urea pool. The lower boundary of the urea amplitude was set to be 60% of the amplitude determined from the first step fitting to account for the spillover effect from adjacent pools such as amine protons.

The peak amplitude of the Lorentzian function representing the urea pool (LA_{ur}) was used as a non-T_1-corrected urea CEST contrast. For T_1-corrected contrast, AREX was calculated as previously described. In brief, AREX in pulsed CEST is expressed as follows[119]:

$$AREX = \left(\frac{1}{Z_{lab}} - \frac{1}{Z_{ref}}\right) R_{1a} = R_{ex} DC$$

in which DC is the duty cycle of saturation pulses, and R_{ex} is the exchange-dependent relaxation rate. R_{1a} is the longitudinal relaxation rate of water. For the analysis from Lorentzian-fitted Z-spectra, Z_{lab} and Z_{ref} are defined as follows[130]:

$$Z_{lab}(\Delta\omega) = c - \sum_{i}^{n=7} L_i$$

$$Z_{ref}(\Delta\omega) = c - \sum_{i}^{n=6} L_i$$

Z_{ref} is composed of all Lorentzian functions except the one that represents the urea pool. Since pure R_{ex} is obtained via normalizing AREX by DC, we used AREX / DC as a T_1-corrected urea CEST contrast.

Urea CEST contrast maps, either T_1-corrected or not, were also generated. For non-T_1-corrected CEST maps, the asymmetric magnetization transfer ratio (MTR_{asym}) was calculated voxel-wise as follows:

$$MTR_{asym} = \frac{S(-1\,ppm) - S(+1\,ppm)}{S_0}$$

where S is the signal intensity of either unsaturated image (S_0) or saturated image at the designated frequency.

AREX / DC maps were generated by using the original definition of Z_{lab} and Z_{ref}:

$$Z_{lab} = \frac{S(+1\,ppm)}{S_0}; \quad Z_{ref} = \frac{S(-1\,ppm)}{S_0}$$

MTR_{asym} and AREX / DC maps were overlaid on corresponding T_2-weighted images.

For correlation of CEST contrast and urea assay results, weighted average of 40-minute post-infusion contrast measurements, both LA_{ur} and AREX / DC, from the cortex (65%), OM (20%) and IM+P (15%)[131] were used to approximate the urea content in the whole kidney.

4.3.4 Statistical Analysis

All statistical analyses were done using Prism 8 (GraphPad Software, San Diego, CA). The normality of the data was confirmed by the Shapiro-Wilk test and visual inspection of quantile-quantile (QQ) plot. Two-way repeated measures analysis of variance was used for comparing the T_1, LA_{ur} and AREX change induced by urea and saline infusion, followed by Tukey post-hoc test. Sidak's post-hoc test was used for comparing the absolute change of contrast induced by urea and saline infusion. For analyzing fold change of contrast, mixed-model effects analysis with Sidak's post-hoc test was performed as several data points were excluded due to very low contrast values before infusion of either urea or saline. A two-tailed t-test was used for comparing the urea concentration in the kidney homogenate from urea-infused and saline-infused mice. Pearson's r was used for correlation between urea assay results and CEST contrast. Adjusted p-values of 0.05 or less were considered statistically significant. All the data are expressed as mean ± standard deviation unless indicated otherwise.

4.4 Results

       In phantoms, the Lorentzian amplitude of the urea pool increased linearly with T_1, while AREX remained constant over the range of T_1 times tested (Figure 4.1). Increasing the gadolinium concentration from 0 to 0.5 mM shortened the T_1 time from 3432 ms to 555 ms, as shown in Figure 4.1A. An MTR_{asym} map and Z-spectra reveal how phantoms with the same concentration of urea have different CEST contrast depending on underlying T_1 times (Figure 4.1A, B). In contrast, maps of AREX / DC demonstrate the same contrast level regardless of underlying T_1 (Figure 4.1A). The correlation between the T_1 time and CEST contrast further reveals that MTR_{asym} linearly depends on the T_1 time while AREX is not affected (Figure 4.1C).
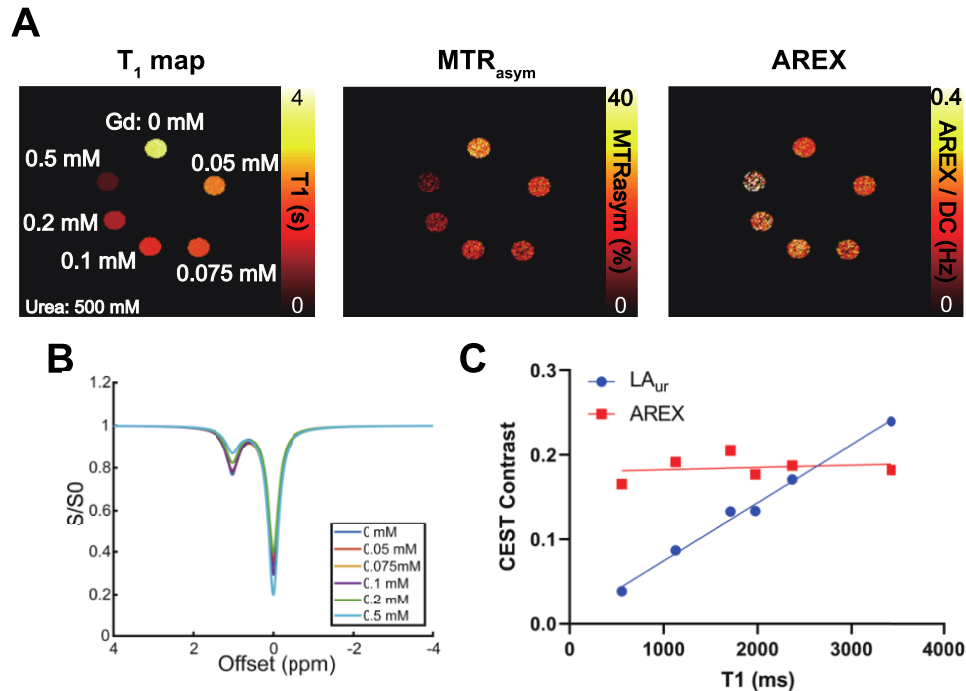
Figure 4.1 The effect of T_1 times on urea CEST contrast and compensation via AREX. (A) T_1 map, MTR_{asym} map, and AREX / DC map of urea phantoms (500 mM) with different amounts of gadolinium (Gd) mixed. (B) Z-spectra acquired from phantoms shown in (A). (C) CEST contrast dependence on T_1 values.

       T_2-weighted images were used to delineate distinct anatomical regions in the kidney (Figure 4.2A). T_1 mapping revealed substantially different T_1 times between anatomical regions (cortex = 1247 ± 39 ms, OM = 1361 ± 44 ms, IM+P = 2028 ± 63 ms, P < 0.0001 for all pairwise comparisons; Figure 4.2B). Infusion of urea increased the T_1 time in the IM+P at 20 minutes post infusion to 2092 ± 76 ms (P = 0.0258 vs. pre-infusion), while the cortex showed a decrease in T_1 times from 1265 ± 50 ms to 1239 ± 49 ms between 20 minutes and 40 minutes after the infusion (P < 0.0001). T_1 times did not change significantly in the OM. In the case of saline infusion, a consistent decrease of T_1 from 1248 ± 30 ms to 1233 ± 20 ms at 20 minutes (P = 0.0104) and to 1222 ± 16 ms at 40-minutes post-infusion (P = 0.0292) was observed in the cortex. The IM+P also demonstrated reduced T_1 at 40 minutes after infusion from 2123 ± 67 ms to 2068 ± 51 ms (P = 0.0412; Figure 4.2D).

36

To assess the advantage of using 7-pool fitting, we compared the goodness of fit to that of 4-pool (amine, amide and NOE2 excluded) and 6-pool (NOE2 excluded) fitting (Figure 4.3). 4-pool fitting failed to capture both the excluded pools and frequently the urea pool despite evident urea contrast in raw Z-spectra (Figure 4.3A). The addition of amine and amide pools improved both the overall spectrum fitting and urea offset frequency fitting (Figure 4.3B). When 7-pool fitting was applied, signal reductions around -1.6 ppm are also captured as a second NOE pool and the overall Z-spectrum fitting is further improved (Figure 4.3C). The goodness of fit was quantitatively compared between 4-pool and 7-pool fitting by measuring normalized mean squared error (NMSE). 7-pool fitting showed better NMSE than 4-pool fitting from Z-spectra acquired from any region or time points, justifying its use for further analysis (Table 4.1).
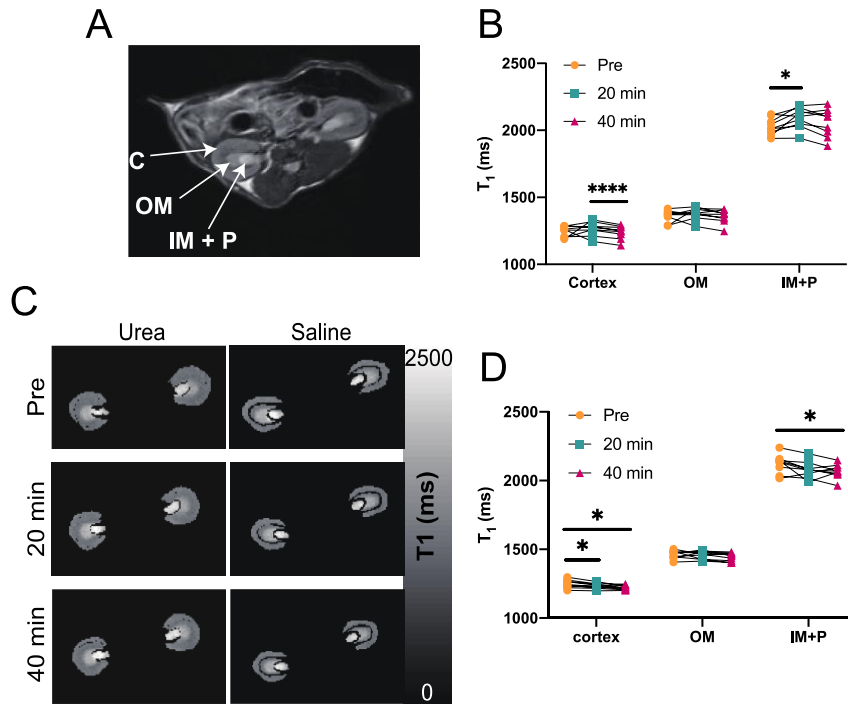
Figure 4.2 T_1 variability between mouse kidney regions. (A) T_2-weighted anatomical image segmenting the kidney into cortex (*C*), outer medulla (*OM*) and inner medulla and papilla (*IM+P*). (B) T_1 values from the urea-infused mice. (n = 9; *P = 0.0258, ****P < 0.0001) (C) T_1 maps of kidneys acquired before and after the infusion of either urea or saline. (D) T_1 values from the saline-infused mice. (n = 9; *P < 0.05)

Infusion of urea substantially increased CEST contrast at 1 ppm in the IM+P at 20- and 40-minutes post bolus infusion as shown in representative Z-spectra in Figure 4.4. Other proton pools did not show significant changes over time after the urea infusion (Figure 4.4 and Figure 4.5). Interestingly, in mice receiving infusion of saline, CEST contrasts for the urea pool also increased, although the degree of enhancement was greater in mice with higher baseline contrast levels (Figure 4.4 and Figure 4.6). Other pools did not show significant changes while NOE contrast decreased in the cortex and OM and NOE2 in the cortex only (Figure 4.5). Similar patterns were observed when CEST contrast of urea was plotted pixelwise using either AREX / DC calculation or MTR$_{asym}$ as shown in Figure 4.7. Maps of urea-infused mice showed increased contrast at the IM+P, but not from other regions (Figure 4.7). In contrast, both AREX / DC and MTR$_{asym}$ maps

from saline-infused mice showed varying degrees of contrast changes in the IM+P only. In general, AREX / DC maps have lower contrast-to-noise ratio (CNR) compared to MTR$_{asym}$ maps due to the added noise from T_1 maps. For instance, the CNR between IM+P and the skeletal muscle around the vertebrae was 4.87 at 20-minute post-infusion of urea for MTR$_{asym}$, while the corresponding AREX / DC map had CNR of 4.17 (Figure 4.7).
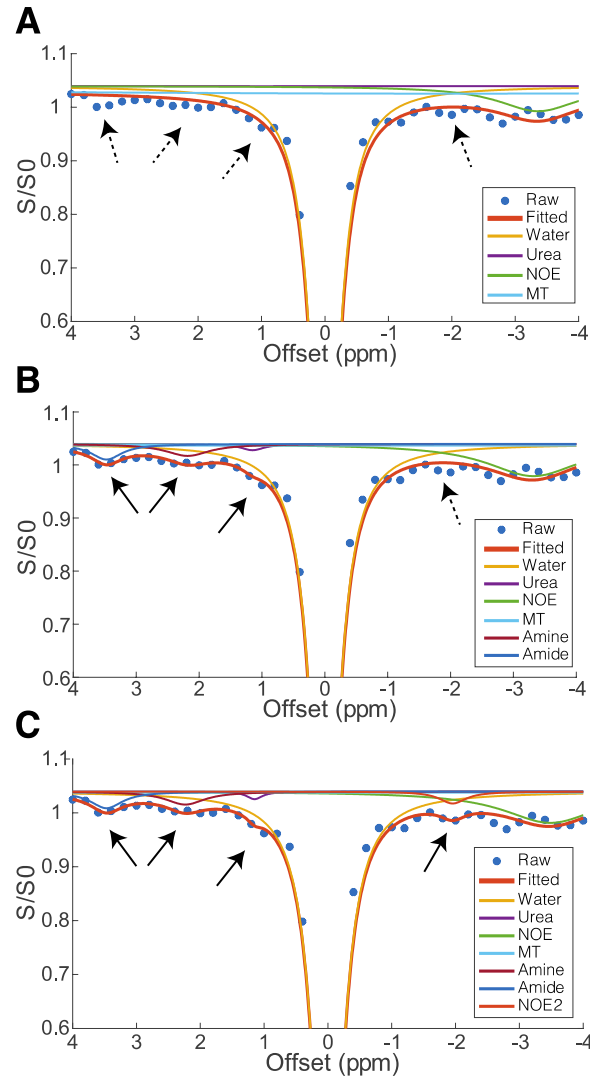
Figure 4.3 Lorentzian fitting of acquired Z-spectra with (A) 4-pool, (B) 6-pool and (C) 7-pool Lorentzian functions. Dashed arrows indicate where the fitting is not sufficiently capturing the CEST contrast. Solid arrows indicate improved fitting by adding additional pools.

Measurements of urea CEST contrast based on Lorentzian fitting are shown in Table 4.2 and Figure 4.6. Urea infusion resulted in significantly increased LA$_{ur}$ in the IM+P at both 20 minutes (P = 0.0116) and 40 minutes (P = 0.0076) after infusion. The other two regions did not show significant changes over time. Significantly higher LA$_{ur}$ was observed from the IM+P compared to the OM at all time points upon urea infusion. The IM+P LA$_{ur}$ measurements were also significantly higher than that of the cortex at 20 minutes (P = 0.0201) and 40 minutes (P =

0.0107) after the urea infusion. Saline infusion showed an increase of LA$_{ur}$ in the OM after 20 minutes (P = 0.0198), but decreased at 40 minutes compared to 20-minutes measurement (P = 0.0388). Significant increases in LA$_{ur}$ over time were observed in the IM+P at 20-minutes (P = 0.0277) and 40-minutes post-infusion (P = 0.0072). No significant change over time was observed in the cortex.

		7-pool			4-pool		
		Pre	20 min	40 min	Pre	20 min	40 min
Urea	C	0.995±0.002	0.993±0.003	0.994±0.003	0.993±0.003	0.991±0.004	0.991±0.004
	OM	0.994±0.003	0.992±0.004	0.993±0.004	0.992±0.004	0.990±0.005	0.991±0.005
	IM+P	0.991±0.003	0.990±0.005	0.988±0.006	0.989±0.004	0.987±0.005	0.986±0.006
Saline	C	0.995±0.002	0.995±0.002	0.995±0.003	0.992±0.002	0.993±0.002	0.993±0.003
	OM	0.993±0.002	0.994±0.002	0.993±0.003	0.990±0.002	0.992±0.002	0.991±0.003
	IM+P	0.990±0.002	0.992±0.003	0.991±0.002	0.987±0.002	0.989±0.004	0.989±0.002

Table 4.1 Normalized mean squared error measured from 7-pool fitting and 4-pool fitting as an assessment of goodness of fit.
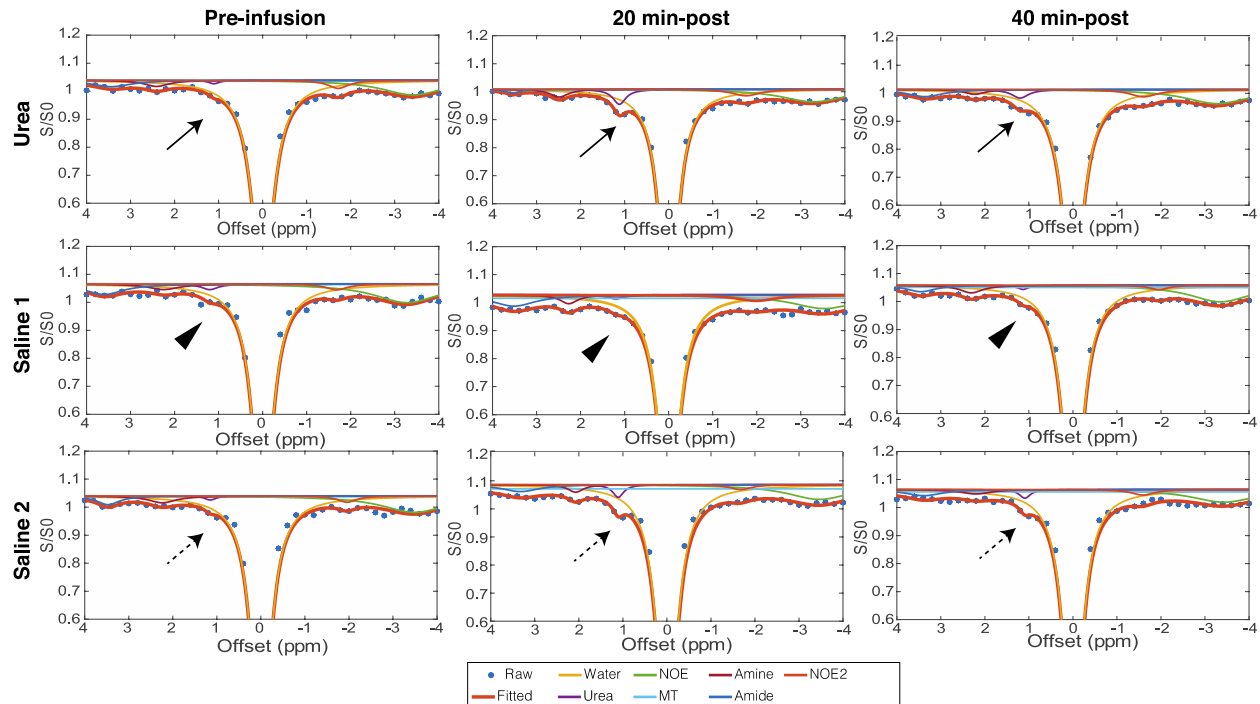
Figure 4.4 IM+P Z-spectra with 7-pool Lorentzian fitting acquired from before and after the infusion of urea or saline. Each Lorentzian function represents the contribution from each pool to the measured Z-spectra. Solid arrows indicate the increasing CEST contrast at +1 ppm after infusion of urea. Saline 1 shows representative Z-spectra from mice that did not show significant changes in CEST contrast at +1 ppm after saline infusion (arrowheads). Saline 2 shows increasing +1 ppm CEST contrast after saline infusion (dashed arrows).
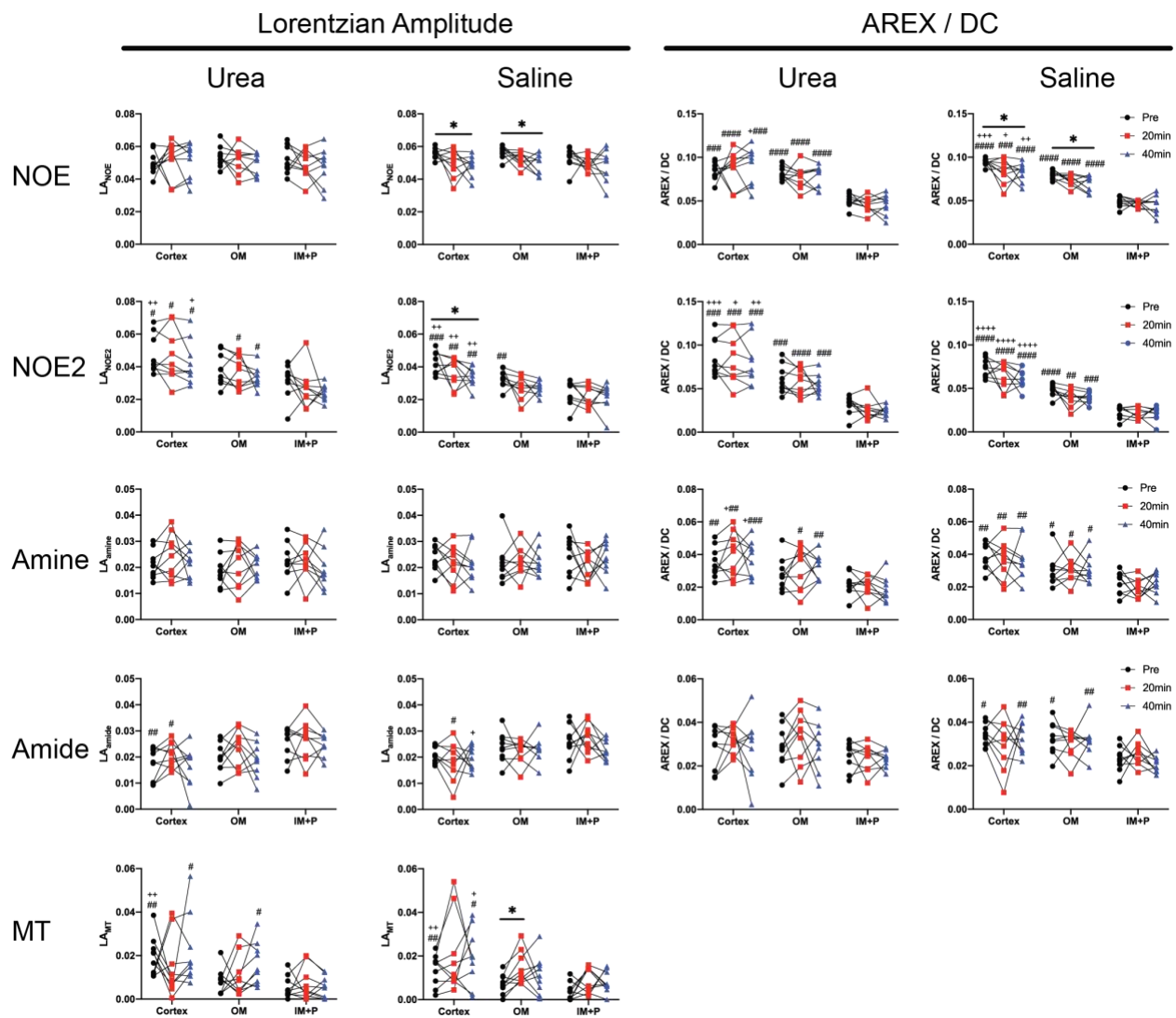
Figure 4.5 Lorentzian amplitudes of proton pools other than urea derived from 7-pool fitting. (*P < 0.05; $^\#$P < 0.05 vs. IM+P, $^{\#\#}$P < 0.01 vs. IM+P, $^{\#\#\#}$P < 0.001 vs. IM+P, $^{\#\#\#\#}$P < 0.0001 vs. IM+P; $^+$P < 0.05 vs. OM, $^{++}$P < 0.01 vs. OM, $^{+++}$P < 0.001 vs. OM, $^{++++}$P < 0.0001 vs. OM)
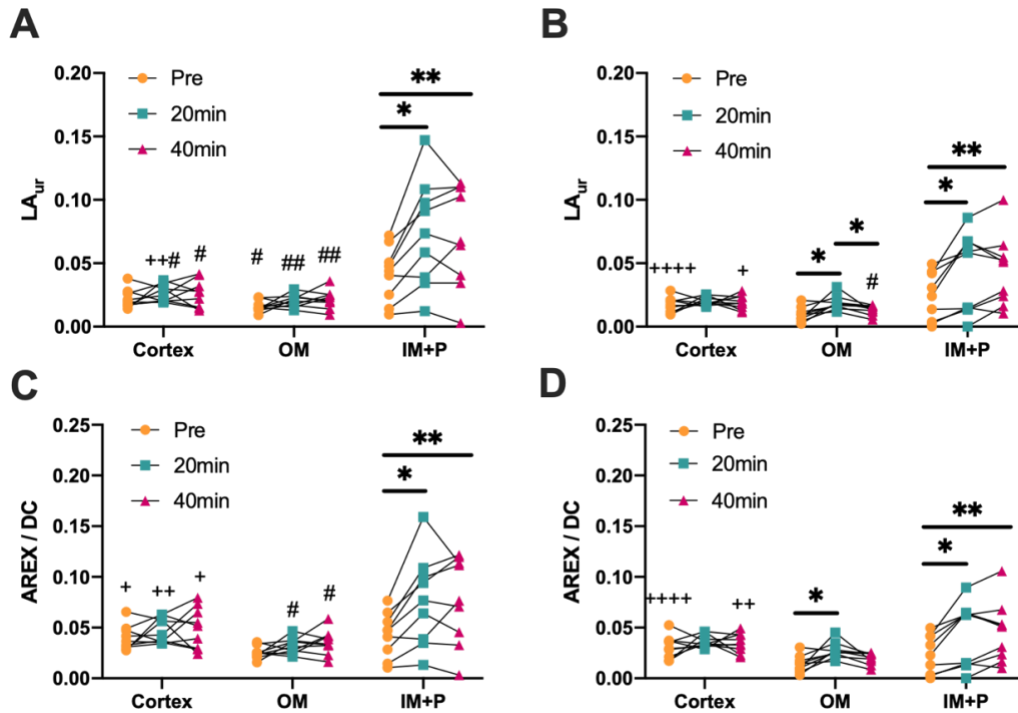
Figure 4.6 LA_{ur} and AREX / DC measured before and after the infusion of either urea or saline. (A) Lorentzian amplitude of the urea pool (LA_{ur}) measured from each region of the kidney before and after the injection of urea. (B) LA_{ur} measured from each region of the kidney before and after the injection of saline. (C) AREX / DC measured from each region of the kidney before and after the injection of urea. (D) AREX / DC measured from each region of the kidney before and after the injection of saline. ($^*P < 0.05$, $^{**}P < 0.01$; $^+P < 0.05$ vs. OM, $^{++}P < 0.01$ vs. OM, $^{++++}P < 0.0001$ vs. OM; $^\#P < 0.05$ vs. IM+P, $^{\#\#}P<0.01$ vs. IM+P)
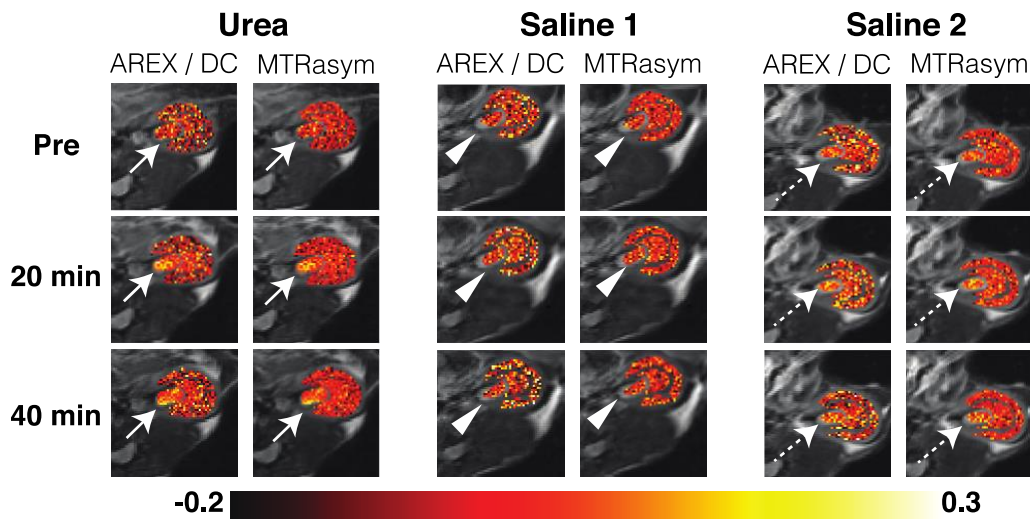
Figure 4.7 AREX / DC and MTR_{asym} maps (1 ppm) acquired before and after the infusion of either urea or saline. Urea infusion increases both AREX / DC and MTR_{asym} in the IM+P (solid arrows). Saline 1 shows an example of mice that do not cause the CEST contrast increase (arrowheads). Saline 2 shows an example of increased CEST contrast in the IM+P upon the saline infusion (dashed arrows).

		LA$_{ur}$			AREX / DC		
		Pre	20 min	40 min	Pre	20 min	40 min
Urea	C	0.022±0.007	**0.026±0.007**	**0.026±0.011**	0.04±0.012	0.047±0.012	0.05±0.02
	OM	**0.016±0.005**	**0.02±0.005**	**0.021±0.008**	0.025±0.006	**0.032±0.008**	**0.035±0.012**
	IM+P	0.041±0.022	0.074±0.042*	0.072±0.04**	0.043±0.022	0.077±0.045*	0.077±0.043**
Saline	C	0.017±0.006	0.02±0.004	0.019±0.005	0.031±0.011	0.036±0.006	0.035±0.009
	OM	0.01±0.006	0.019±0.006*	**0.013±0.004**	0.014±0.008	0.028±0.008*	0.02±0.006
	IM+P	0.023±0.019	0.042±0.031*	0.045±0.028**	0.023±0.019	0.043±0.032*	0.046±0.03**

Table 4.2 Urea CEST contrast measurements from each anatomical region of the mouse kidney before and after infusion of urea or saline. Bold fonts indicate statistical significance between IM+P. (*$P < 0.05$, **$P < 0.01$ vs. Pre)

Correction of CEST contrast for regional differences in native T$_1$ times results in different spatial patterns of baseline urea CEST contrast as shown in Table 4.2. Parallel to LA$_{ur}$ measurements, the baseline AREX / DC measurements show that the cortex has significantly higher urea CEST contrast than the OM, while the significant difference between the OM and IM+P shown in LA$_{ur}$ measurements is not observed in AREX / DC. Both LA$_{ur}$ and AREX / DC show no significant difference between the cortex and IM+P. AREX / DC significantly increased 20 minutes after urea infusion at the IM+P ($P = 0.0125$), and the increased AREX / DC was maintained at 40 minutes after the infusion ($P = 0.007$). A Region-wise comparison revealed that AREX / DC from IM+P at 20 minutes and 40 minutes post-infusion were significantly higher than those from the OM. The cortex showed significantly higher AREX / DC than the OM before ($P = 0.0154$), 20 minutes ($P = 0.0019$) and 40 minutes ($P = 0.0436$) after the urea infusion. Contrary to the LA$_{ur}$ measurements that showed significant differences between the cortex and the IM+P at 20- and 40-minute post-infusion, AREX / DC measurements did not differ between these regions at all time points. Saline infusion showed similar results, with AREX / DC in the IM+P increasing at 20-minutes post-infusion ($P = 0.0202$) and 40-minutes post-infusion ($P = 0.0087$). AREX / DC values in the OM increased at 20-minutes post-infusion only ($P = 0.0218$). The cortex also showed significantly higher AREX / DC than OM before ($P < 0.0001$) and 40 minutes ($P = 0.0041$) after the saline infusion. No significant difference between the IM+P and either the cortex or OM were observed.

The magnitude of change in CEST contrast was also compared between saline and urea infusions (Table 4.3 and Figure 4.8). The LA$_{ur}$ increase at 20 minutes after the urea infusion was significantly higher in the IM+P than the cortex ($P = 0.0283$) or OM ($P = 0.01$). The greater increase of LA$_{ur}$ in the IM+P than in either the cortex ($P = 0.01$) or OM ($P = 0.0063$) was also observed 40 minutes after the urea infusion. Saline infusion showed a comparable increase of LA$_{ur}$ at both 20 minutes and 40 minutes post-infusion to that from urea infusion in all regions. However, no significant difference between IM+P and other regions were observed. The magnitude of AREX / DC increase from before the urea infusion to 20 minutes after was significantly higher in the IM+P than the OM ($P = 0.0104$). Similar to LA$_{ur}$ measurements, saline infusion showed a comparable degree of AREX / DC increase to that from urea infusion in all regions at both 20-minutes and 40-minutes post-infusion, while no significant differences were observed in region-wise comparison.

	20 min - Pre				40 min – Pre			
	LA_{ur}		AREX / DC		LA_{ur}		AREX / DC	
	Urea	Saline	Urea	Saline	Urea	Saline	Urea	Saline
C	**0.004±0.01**	0.003±0.008	0.007±0.016	0.006±0.014	**0.004±0.014**	0.002±0.008	0.01±0.024	0.004±0.014
OM	**0.004±0.007**	0.009±0.008	**0.007±0.011**	0.013±0.012	**0.005±0.011**	0.003±0.007	**0.01±0.017**	0.005±0.011
IM+P	0.032 ±0.025	0.019±0.017	0.034±0.026	0.02±0.017	0.031±0.022	0.021±0.015	0.034±0.024	0.023±0.017

Table 4.3 Absolute increase of urea CEST contrast measured over time. Bold font figures indicate statistical significance between IM+P.
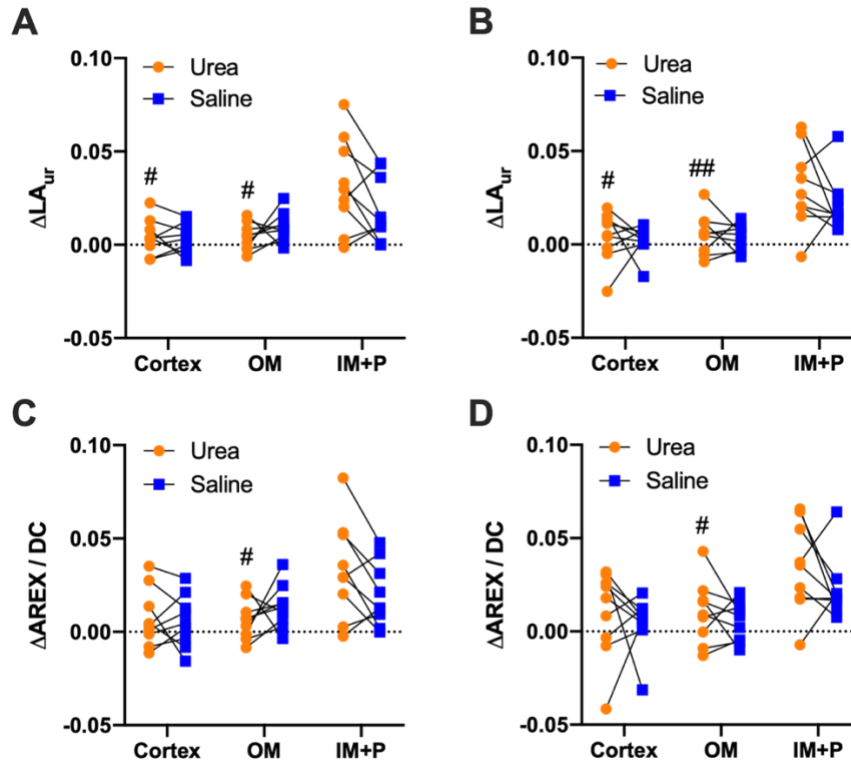
Figure 4.8 The increase of LA_{ur} and AREX / DC from infusion of either urea or saline. (A) LA_{ur} increase measured at 20 minutes after the infusion of either urea or saline. (B) LA_{ur} increase from pre-infusion to 40 minutes post-infusion. (C) The increase of AREX / DC measured at 20 minutes post-infusion. (D) The increase of AREX / DC measured at 40 minutes from the pre-infusion state. ([#]$P < 0.05$ vs. IM+P, [##]$P < 0.01$ vs. IM+P).

The CEST contrast increase was further analyzed measuring the ratio between post- and pre-infusion contrasts (Table 4.4 and Figure 4.9). Both urea and saline infusion caused approximately 1.3 ~ 2.0-fold increase of LA_{ur} at 20 minutes post-infusion from all kidney regions. No significant differences were observed among kidney regions or between urea and saline infusions. The ratio between 40-minute post-infusion LA_{ur} and pre-infusion measurements showed similar patterns of contrast increase. The fold increase measurements of AREX / DC mirrored the results from LA_{ur} fold increase measurements at both 20-minute and 40-minute post-infusion. No significant differences between urea and saline-infused groups were observed in all the regions and across time points.

		20 min / Pre				40 min / Pre			
		LA$_{ur}$		AREX / DC		LA$_{ur}$		AREX / DC	
		Urea	Saline	Urea	Saline	Urea	Saline	Urea	Saline
Normal	C	1.3±0.572	1.359±0.658	1.265±0.51	1.378±0.67	1.281±0.552	1.227±0.451	1.318±0.537	1.262±0.469
	OM	1.376±0.587	2.053±1.362	1.346±0.534	2.05±1.407	1.543±1.023	1.295±0.719	1.568±0.942	1.316±0.733
	IM+P	1.809±0.51	1.766±0.683	1.785±0.493	1.807±0.639	1.674±0.631	1.807±0.469	1.712±0.615	1.892±0.546
Renal injury	C	1.523±0.974	0.959±0.248	1.566±0.959	0.944±0.269	1.269±0.588	0.913±0.182	1.290±0.577	0.905±0.184
	OM	1.222±0.512	0.891±0.088	1.303±0.551	0.901±0.072	0.750±0.257	1.173±0.081	0.798±0.277	1.219±0.062
	IM+P	1.547±0.648	0.823±0.316	1.656±0.705	0.839±0.340	0.711±0.451	1.005±0.275	0.752±0.484	1.034±0.272

Table 4.4 Fold increase of urea CEST contrast in normal mice and renal injury model measured by normalizing to pre-infusion measurements.

Measurement of urea concentration from the kidney homogenate showed significantly higher urea concentration (P = 0.002) from the kidneys of mice infused with urea (32.6 ± 8.7 mM) than the saline-infused group (18.5 ± 3.9 mM; Figure 4.10A). Urea assay results also revealed similarly significant correlations with both LA$_{ur}$ (R^2 = 0.4964, P = 0.0011; Figure 4.10B) and AREX / DC (R^2 = 0.4687, P = 0.0017; Figure 4.10C) measurements.

The results from the renal injury model are summarized in Figure 4.11. Compared to normal mice, AA-administered mice showed reversed contrast between the cortex and OM from T$_2$-weighted anatomical images (Figure 4.11A). T$_1$ maps showed less contrast between the cortex and OM, compared to normal mice. T$_1$ times from each region before any infusion were 1693 ± 101 ms, 1555 ± 132 ms, and 2203 ± 89 ms for the cortex, OM and IM+P, respectively, which are all higher than the same regions from normal mice. Both MTR$_{asym}$ and AREX / DC maps showed less contrast between the IM+P and other regions, and both urea and saline infusion did not generate significant contrast enhancement as was observed in normal mice (Figure 4.11B, Table 4.4). Both MTR$_{asym}$ and AREX/DC values for each kidney region are detailed in Table 4.4. The ratiometric analysis of contrast change showed that urea induces 1.3 ~ 1.7-fold increase of LA$_{ur}$ and 1.2 ~ 1.5-fold increase of AREX / DC in 20-minute post-infusion. However, 40-minute post-infusion measurements show decrease of LA$_{ur}$ and AREX / DC (fold < 1) from the OM and IM+P (Table 4.4). Saline infusion did not generate contrast changes, both LA$_{ur}$ and AREX / DC, across all time points with fold changes ranging 0.8 ~ 1.2.
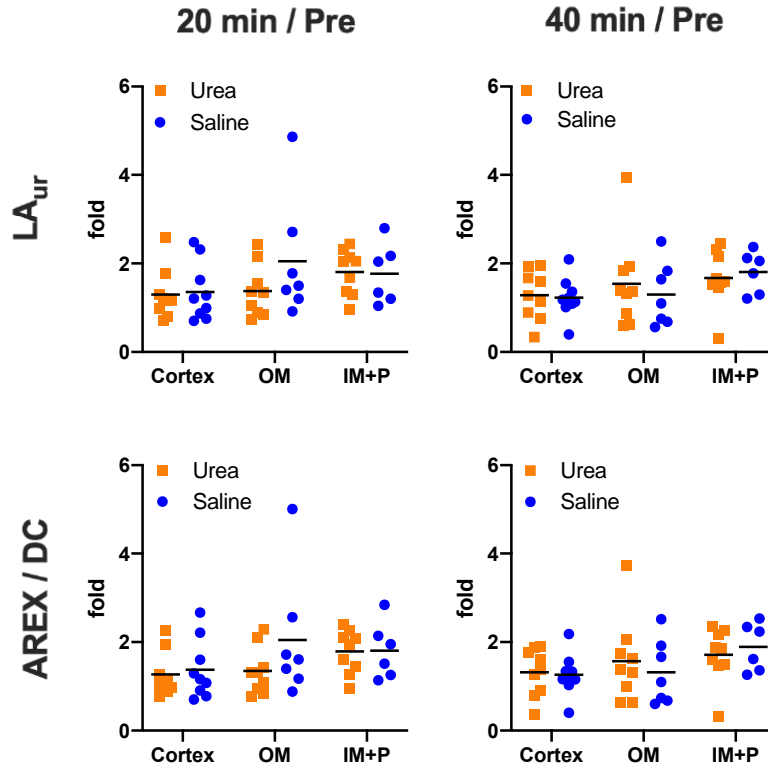
Figure 4.9 Ratiometric analysis of urea CEST contrast increase from infusion of urea or saline. Either Lorentzian amplitude (LA_{ur}) or AREX / DC measured at 20 minutes (20 min / Pre) or 40 minutes (40 min / Pre) after the infusion of urea or saline was normalized by the contrast measured before the infusion to calculate fold increase of urea CEST contrast.
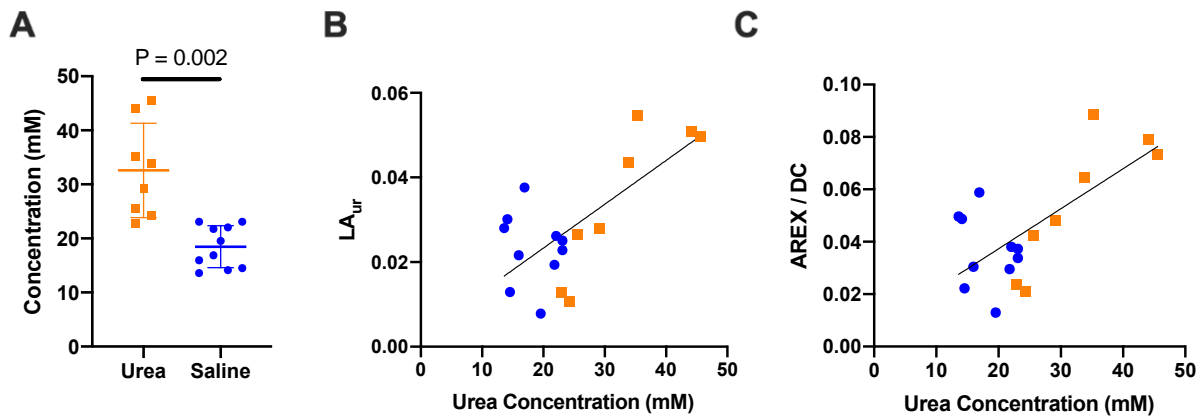
Figure 4.10 Validation of urea CEST contrast by kidney homogenate urea assay. (A) Comparison of urea concentrations from the kidney homogenate from urea-infused mice and saline-infused mice. (B) Correlation between kidney homogenate assay and LA_{ur} measurement (R^2 = 0.4964, P = 0.0011). (C) Correlation between kidney homogenate assay and AREX measurement (R^2 = 0.4687, P = 0.0017). Circles indicate saline-infused group, and squares indicate urea-infused group
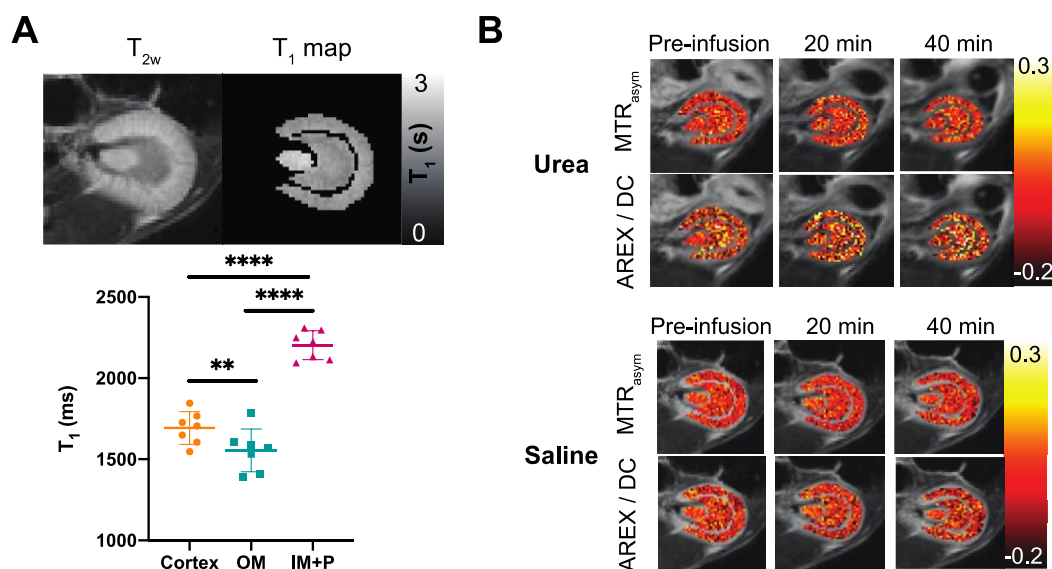
Figure 4.11 dudeCEST imaging of AA-induced nephropathy model. (A) T_2-weighted anatomical image, corresponding T_1 map and T_1 measurements from each anatomical region of the kidney (**$P < 0.01$, ****$P < 0.0001$). (B) CEST contrast maps of diseased mouse kidneys before and after infusion of urea and saline. Whereas healthy mice demonstrate a gradient from the cortex to IM+P, the kidneys of injured mice demonstrate greater enhancement in outer kidney regions in response to urea and saline relative to the IM+P. The use of AREX further compensates for injury induced changes in T_1 relaxation times in each kidney region.

4.5 Discussion

In this study, we demonstrated the importance of using an expanded multi-pool Lorentzian fitting algorithm for analysis of renal Z-spectra alongside AREX compensation for the impacts of differences in regional T_1-times when measuring urea CEST contrast. Phantom experiments showed that conventionally measured urea CEST contrast (MTR$_{asym}$) is highly dependent on T_1 times such that even the same concentration of urea generates increasing contrast with increasing T_1 times, whereas AREX removes the effect of T_1 times upon quantified CEST contrast. Second, we demonstrated that a delayed urea enhancement (dudeCEST) approach consistently highlights the IM+P specific increase of CEST contrast at 20 minutes after urea infusion. Further, when combined with appropriate AREX measurement this can enable non-invasive assessment of the urea recycling action of the IMCD as validated via urea assay results from kidney homogenate. When accounting for baseline levels of urea CEST contrast in the kidney, the infusion of saline alone induces an aggregate 1.8-fold increase in urea CEST contrast at 20 and 40 minutes after infusion that is identical in magnitude to that seen in response to urea infusion. Further, in case of renal injury model, significant increases of T_1 times are observed from all regions, with particularly large increase in the cortex, and the fold increase of urea CEST contrast upon saline infusion is severely attenuated.

In this study we fit each Z-spectrum to a sum of 7 Lorentzian functions in order to quantify CEST contrast generated by multiple metabolite pools, magnetization transfer, and multiple NOE populations. Previously, we used a 4-pool Lorentzian fitting approach (water, urea, single NOE, and MT) to isolate the contribution from a urea pool to the Z-spectrum.[128] However, recent studies

have demonstrated the potential CEST contrast originating from exchangeable amine and amide protons within various renal metabolites.[117] The addition of Lorentzian functions representing these pools achieved better fitting both around +2 ~ +4 ppm of a Z-spectrum and around the urea pool (Figure 4.3). Similarly, compared to our prior study we added a second NOE pool (NOE2) around -1.6 ppm to our fitting of the Z-spectrum. This new NOE pool has recently been identified as a potential CEST imaging marker for tumors and ischemic stroke.[132,133] It was also reported that this pool becomes more evident in a Z-spectrum when using a lower saturation power (0.25 – 1 μT)[134], which encompasses the saturation power (0.6 μT peak amplitude) used in this study. Adding these pools in the analysis improved overall Z-spectra fitting as assessed by NMSE and more accurately captured urea CEST contrast than in our prior study. Further, this enabled investigation into potential additional contrast changes among other metabolites (Figure 4.5) that may demonstrate meaningful changes in settings of kidney disease. However, it is important to note that our saturation scheme was designed for slowly exchanging urea protons and is significantly different from the schemes used for other metabolites and MT, which require stronger B_1 amplitude and shorter saturation times. Subsequently, alternate saturation schemes may provide more robust measurement of these additional metabolites. In addition, the use of a smaller number of pools will have a greater impact on quantification of urea CEST contrast than on measurement of renal CEST contrast following injection of iodinated contrast agents, that resonate further downfield, as is performed for ratiometric CEST based renal pH imaging.[110,112,135–137]

The importance of T_1 correction for quantifying the CEST effect without underlying contamination is supported by previous studies that implemented AREX for other organs. For example, Zaiss et al. showed that after compensating for T_1 relaxation times, the amide CEST contrast between glioblastoma and contralateral normal brain tissue decreases, while the NOE CEST contrast increases.[138] Similarly, compensation for vastly different regional T_1 times is crucial in comparing differences in CEST contrast between different anatomical regions in the kidney. Previously Hueper et al. measured T_1 times of the cortex (1270 ms) and OM (1200 ~ 1600 ms) of mouse kidneys at 7T that are consistent with our T_1 measurements.[118] Theoretically, assuming urea concentration of 300 mM, this magnitude of T_1 difference can generate up to 0.9% (absolute) difference in MTR_{asym} and has been previously confirmed using numerical simulation.[80,128] Our phantom studies validated this simulation result by showing that LA_{ur} measured from 500 mM urea phantoms was linearly dependent on T_1 times. In contrast, when using AREX as a measurement of CEST contrast, this linear dependency on T_1 times was removed, indicating that AREX is a better quantification method for comparing urea concentrations in distinct anatomical regions of the kidney. While the patterns of elevated urea CEST contrast in the IM+P following urea injection were similar regardless of which quantification method was used, differences in regional baseline contrast values were observed between simple measurement of the Lorentzian amplitude and AREX correction. Importantly, changes to both the intra-renal metabolite gradient and regional T_1 times occur in cases of kidney injury and failure. Subsequently, our data suggest that continued compensation for underlying differences in T_1 times via AREX is crucial for further application of CEST imaging of the kidney.

Dynamic imaging of urea handling in previous hyperpolarized ^{13}C MRI studies demonstrated the feasibility of monitoring both urea handling and renal perfusion.[93,106,139] Similarly, CEST-MRI has been used to measure the dynamic glucose enhancement (DGE) of brain tumors.[121,140,141] In our prior study we attempted to perform dynamic CEST-MRI of the kidney following infusion of urea in order to measure the kinetics of renal urea handling.[128] However,

several confounding factors including thermal drift and B_0 field shift during infusion hindered reproducible acquisition of dynamic curves, and acquisition of post-infusion Z-spectra was performed long after likely peaks in CEST contrast.[108,109] In this study we aimed to test whether delayed enhancement of urea CEST contrast in the kidney at specific time points following bolus injection could be used to assess the urea concentrating capacity of the kidney. This delayed enhancement approach, when combined with AREX correction for changes in T_1 times, revealed significant enhancement of CEST contrast in the IM+P upon urea injection at both 20 and 40 minutes post infusion. The magnitude of urea CEST contrast at both time points was substantially greater than that observed in our prior study, likely due to earlier measurement time following injection. In addition, in contrast to our prior study, the use of AREX revealed significant changes in urea CEST contrast at 20 minutes post injection in the cortex relative to the inner medulla, suggesting that the use of multiple post-injection delay times could provide unique assessment for each kidney region. Finally, in contrast to our prior study which showed no impact of saline infusion upon urea CEST contrast, the bolus injections of either saline or urea yielded the same increase of urea CEST contrast when normalizing for baseline urea CEST contrast, particularly in the IM+P (Table 4.4). Importantly, the ratiometric similarities were observed when comparing either Lorentzian amplitude or when AREX/DC was used to remove the potential influence of changes in T_1 times due to infused substance. This suggests that increased labeling efficiency resulting from volumetric expansion of the free water pool, particularly in the IM+P where urea concentrations are relatively high under normal physiological conditions, contributes substantially to changes in measured urea CEST contrast. Additionally, saline infusion may alter the pH level in the kidney and thereby increase the exchange rate of urea protons. Further investigation is needed to clarify the mechanisms by which saline infusion results in increased urea CEST contrast in the kidney. However, this finding implies the possibility that changes in urea CEST contrast in response to higher doses of saline could be used to non-invasively assess renal function without the safety concerns associated with urea.

The results from renal injury model study also support the importance of T_1 time correction and the potential of using saline for probing renal function. In response to renal injury increased T_1 times were observed in all regions, with the most significant increase of 500 ms in the cortex. The regionally variable change of T_1 relaxation over time due to renal disease progression influences the urea CEST contrast and complicates the quantification of the intrarenal urea gradient. Without T_1 correction, comparison of renal urea content between normal and diseased kidneys and longitudinal assessment of urea content change may not be accurate. Furthermore, mice with AA-induced renal injury showed less responsiveness to the infusion of urea and saline than normal mice showed, in terms of fold increase of CEST contrast from pre-infusion state. This implies that urea CEST contrast change upon infusion of saline can be utilized for diagnosis of diseases that involve progressive renal function loss.

There are several limitations to this study that warrant further discussion. The urea concentration in the kidney, especially in the IM+P, can significantly vary based on the diuretic state of mice. Previous study showed that urea permeability of IMCD can vary up to 400% based on the diuretic state of mice[123]. Tightly controlling the diuretic state may reduce the variability of baseline urea concentration, response to urea or saline infusion, and the corresponding urea CEST contrast measurements. In order to correct for signal drift in the acquired Z-spectra, we used ± 20 $\sim \pm 50$ ppm offset images as proxies of unsaturated images and applied biexponential fitting. Although we observed minimal or no MT effect in these offset frequency ranges, any unaccounted

MT would reduce the precision of subsequent correction. In future studies, a larger number of unsaturated images interspersed in the Z-spectra should be acquired as previously described.[107,142] Next, although we assumed that the CEST contrast at +1 ppm is solely from urea, many metabolites in the kidney have labile protons that resonate around the same frequency as urea. The concentration of each metabolite is too low to be detected by CEST-MRI, but collectively they can alter the Z-spectra, as demonstrated by a previous study that showed the Z-spectra from urea phantoms become similar to that from urine only after adding other +1 ppm-resonating kidney metabolites.[117] The contribution from these other metabolites may in fact explain relatively high CEST contrast detected from the cortex and OM in this study. Considering the urea recycling action of the IMCD, IM+P should have up to 100-fold higher urea concentration than the cortex and OM in a physiological condition.[10] Yet, the cortex and OM showed comparable AREX and LA_{ur} before infusing either urea or saline, implying that other metabolites that have a higher concentration in the cortex and OM may have affected the CEST contrast measurement. For better quantification of urea CEST contrast, exchange rate-selective methods such as variable delayed multi-pulse (VDMP) method[115,116] may be useful as urea protons have a slow exchange rate compared to other +1 ppm-resonating metabolites.[117] Lastly, although we corrected for a significant difference in T_1 times between kidney regions, the effect of pH level on the exchange rate of urea protons remains uncorrected. Previous studies on measuring intrarenal pH gradients showed that the pH becomes more acidic from the cortex (7.0 ~ 7.3) to the IM+P (6.3 ~6.6).[110,143,144] Since urea is both acid- and base-catalyzed, the exchange rate of urea protons becomes slowest at neutral pH and increases as the pH becomes either more acidic or basic.[145] Through a phantom study, we previously showed that in a physiological kidney pH range, the MTR_{asym} from 800 mM of urea can change up to 9% (absolute units).[128] Thus, for better quantification of an intrarenal gradient of urea through CEST, the pH effect should also be taken into account. This may be achieved by acquiring multiple Z-spectra with different B_1 amplitudes and applying omega plot analysis, which will enable quantification of concentration and exchange rate of urea protons simultaneously.[146,147] However, the feasibility of applying omega plot analysis to urea CEST should be further investigated as a previous urea CEST study demonstrated that this method may not be applicable to protons with a slow exchange rate.[80,117]

4.6 Conclusion

In this study, we demonstrated a delayed urea differential enhancement (dudeCEST) approach for probing the urea recycling action in the IM+P. The urea CEST contrast increased substantially in the kidney at 20 minutes and 40 minutes after the infusion of urea, with the IM+P showing the largest effect. T_1 mapping showed significantly different T_1 times in distinct anatomical regions of the kidney, and the correction for T_1 using AREX resulted in a strong correlation between subsequent contrast and underlying urea concentration as assessed via assay of kidney homogenate. Normalized changes in urea CEST contrast revealed a possible use for saline injection as a safe contrast agent for the assessment of renal function via CEST-MRI. Less degree of CEST contrast change upon infusion of saline and significantly increased T_1 times observed from the diseased kidneys also support the potential usage of saline for renal imaging and the need for T_1 correction.

Chapter 5. Disease Application: Noninvasively differentiating acute and chronic injuries via CEST and qMT imaging

5.1 Synopsis

Standardized blood tests often lack adequate sensitivity and specificity to capture the gradual progression of renal injuries. We suggest a multiparametric molecular MRI approach as a noninvasive tool for monitoring renal function loss and distinguishing different types of renal injuries. Chemical exchange saturation transfer (CEST) and quantitative magnetization transfer (qMT) imaging were performed on cisplatin and aristolochic acid (AA)-induced nephropathy mouse models. AA model showed disrupted spatial gradients of urea in the kidney and significantly decreased nuclear Overhauser enhancement (NOE) CEST and qMT contrast. The cisplatin model showed slightly decreased qMT contrast only. Correlation of MR parameters to histological features showed that NOE CEST and qMT imaging are sensitive to both acute and chronic injuries, while urea CEST shows a significant correlation only to acute injuries. These results indicate that our multiparametric approach allows comprehensive and totally noninvasive monitoring of renal function and histological changes for distinguishing different nephropathies.

5.2 Introduction

Standardized blood tests such as serum creatinine level (SCr) and blood urea nitrogen (BUN) are widely used for the diagnosis of renal diseases[22,41]. While these tests are effective in measuring the renal function represented by the estimated glomerular filtration rate (eGFR), the hyperfiltration by intact nephrons often hinders the detection of renal functional decline until 50% of the function is lost[87]. This late detection of renal function loss is critical especially in clinical scenarios that accompany the gradual progression of renal function loss after an acute injury, such as acute kidney injury (AKI)-to-chronic kidney disease (CKD) transition and delayed graft rejection after renal transplant [20,35]. Since the gradual accumulation of renal injuries is often not picked up by blood tests, there is currently no reliable method other than biopsy to detect such subtle damages in the kidneys in a timely manner[148,149]. Also, the incidence of acute injuries often elevates the risk of an additional episode of acute injuries, requiring follow-up monitoring of pathological status of the kidney to track and distinguish progression to CKD and an incidence of AKI[150].

Medical imaging can aid such repeated monitoring of the kidney in a noninvasive manner. Currently, however, medical imaging modalities such as ultrasound, computed tomography (CT), and magnetic resonance imaging (MRI) are mostly limited to detecting structural abnormalities such as the size of the kidney, cysts, and tumors [50,62]. Functional imaging methods such as Doppler ultrasound and contrast-enhanced CT and MRI are focused on perfusion only and do not report parenchymal injuries [67,88]. More importantly, contrast agents used for CT and MRI perfusion imaging are contraindicated to renal disease patients and may induce nephrogenic systemic fibrosis [61,66]. Thus, a noninvasive imaging method that directly and comprehensively reports the renal function and the underlying tissue alterations is urgently needed.

Chemical exchange saturation transfer (CEST) imaging is a novel molecular MRI technique that generates contrast from a molecule of interest by using radiofrequency saturation at the offset frequencies of exchangeable protons on the molecule of interest to label the magnetic

moment and bias the subsequent signal intensity as a function of chemical exchange. [74,127,151]. Recently, we demonstrated the feasibility of quantitative imaging of urea in the healthy mouse kidneys [128,152] using CEST-MRI. Similarly, others have demonstrated the ability to monitor renal pH using CEST-MRI contrast agents [113,135,137,153]. Urea is a major component of the spatial osmolarity gradient in the kidney through which fine tuning of water reabsorption is achieved [8–10]. As previous mouse studies have shown disrupted urea gradients in the kidney upon the onset of sepsis-induced AKI and diabetic nephropathy, we hypothesized that the aforementioned urea CEST MRI method can be a useful tool for noninvasively monitoring the progression of renal diseases [98,126].

Renal injuries often involve various cellular and molecular level alterations, such as tubular cell necrosis, apoptosis, and fibrosis development. These diverse patterns of renal injuries may not be accurately captured by a single urea CEST contrast and require other MR parameters that reflect different characteristics of the injury. Since CEST MRI is performed by saturating multiple offset frequencies around the resonant frequency of water, CEST contrast from other exchangeable protons can be harnessed simultaneously for a thorough investigation of renal pathology. For instance, CEST contrast from aliphatic and olefinic protons generated via relayed nuclear Overhauser enhancement (NOE) is widely studied for imaging brain tumors and infarction from ischemia [138,154]. The NOE CEST contrast has also shown the potential of detecting nephropathies in a mouse study [155,156]. Similarly, quantitative magnetization transfer (qMT) contrast from semisolid macromolecules can also be achieved by targeting far offset frequencies and extracting the relative pool-size ratio (PSR) of the bound water pool [157,158]. This method has shown to be sensitive to fibrosis, a hallmark of CKD, in multiple preclinical renal studies [159,160]. Overall, these methods may complement urea CEST MRI by providing different aspects of renal pathology, allowing comprehensive investigation of renal function and tissue integrity.

5.3 Results

5.3.1 Validating cisplatin and AA nephropathy models by blood tests

To confirm the development of renal injuries from cisplatin and AA administration, blood urea nitrogen (BUN) and SCr were measured over time from mice. Blood tests showed significant increases in BUN and SCr in both the cisplatin and AA groups (Figure 5.1). The BUN of the cisplatin group significantly increased at week 2 compared to week 0 (23.55 ± 2.50 to 39.38 ± 11.01mg/dL; P = 0.0032), and an increase in SCr was evident at week 3 (0.115 ± 0.049 to 0.242 ± 0.119 mg/dL, P = 0.0326). The AA group showed substantial increases of both BUN (27.31 ± 6.62 to 64.44 ± 12.86 mg/dL, P = 0.0008) and SCr (0.12 ± 0.07 to 1.64 ± 1.27 mg/dL, P = 0.0074) 5 days after the initiation of AA injections. Overall, blood tests indicated the progression of renal injuries in both cisplatin and the AA group, but the extent of renal function loss was more severe in the AA group.

5.3.2 In vivo CEST and qMT MRI scans of cisplatin and AA nephropathy models

After the disease models were validated by blood tests, the mice from the two disease models were scanned with MRI in order to quantify T_1 relaxation times, acquire CEST z-spectra, and measure pool-size ratio by qMT. Each series of acquisitions was performed twice per scan,

before and after the infusion either 150 μL of saline or 2M urea, in order to observe the renal response to the infusion as a change of urea CEST. Both models showed significant increases in T_1 times in the cortex (Figure 5.2). The Cisplatin group showed increased T_1 times in the cortex at week 1 compared to the baseline (1182±34 to 1292±80 ms, P = 0.0011), which was sustained up to week 3 (1276 ms, P = 0.0009; Figure 5.2C). Similar changes were transiently observed in the outer medulla (OM) at week 1 (1455±70 to 1523±85 ms, P = 0.0399. In contrast, the AA group showed larger increases in T_1 values at day 5 in the cortex (1207±56 to 1516±94 ms, P < 0.0001) as shown in the representative T_1 maps (Figure 5.2B).
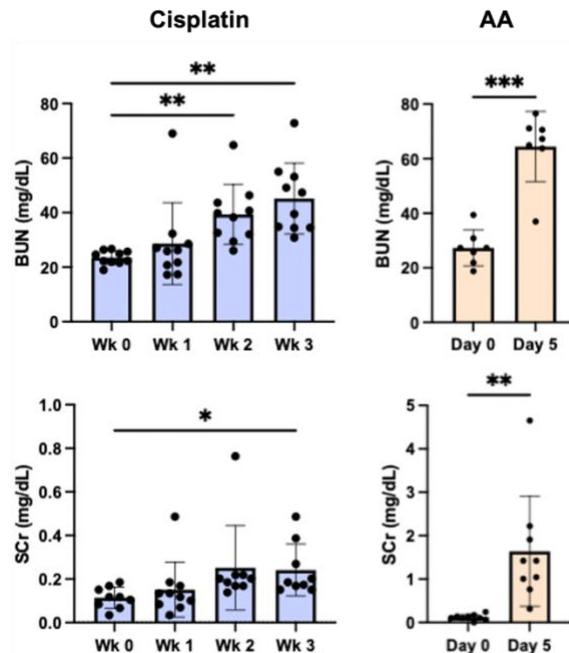
Figure 5.1 Blood tests for cisplatin and aristolochic acid (AA)-induced nephropathy models. The cisplatin group shows a steady increase of both blood urea nitrogen (BUN) and serum creatinine (SCr) level. BUN starts showing a significantly higher level than the week 0 baseline from week 2, and SCR from week 3, indicating chronic development of renal injuries. AA group shows more acute and severe development of renal injuries reflected by a much more significant increase of both BUN and SCr in 5 days. *P < 0.05, **P < 0.01, ***P < 0.001.

For the measurement of CEST contrast from urea, the CEST contrast at 1 ppm was corrected for T_1 times based on the apparent exchange-dependent relaxation (AREX) method (Figure 5.2A) [119]. The spatial gradient of urea AREX contrast was measured by normalizing the urea AREX from the OM and inner medulla and papilla (IM+P) to that from the cortex (Figure 5.3A). The spatial gradient of urea AREX did not change over time in the cisplatin group, whereas the AA group showed significant increases of the OM-to-cortex urea AREX ratio as a function of disease progression. The ratio increased from 0.511±0.116 to 0.773±0.215 (P = 0.0003) in the urea-infused subgroup. Similarly, the ratio increased from 0.531±0.124 to 0.843±0.141 (P = 0.0001) in the saline-infused group. This trend of a disrupted urea AREX gradient between the OM and the cortex is observed in the urea AREX maps overlaid on T_2-weighted anatomical images (Figure 5.3B).
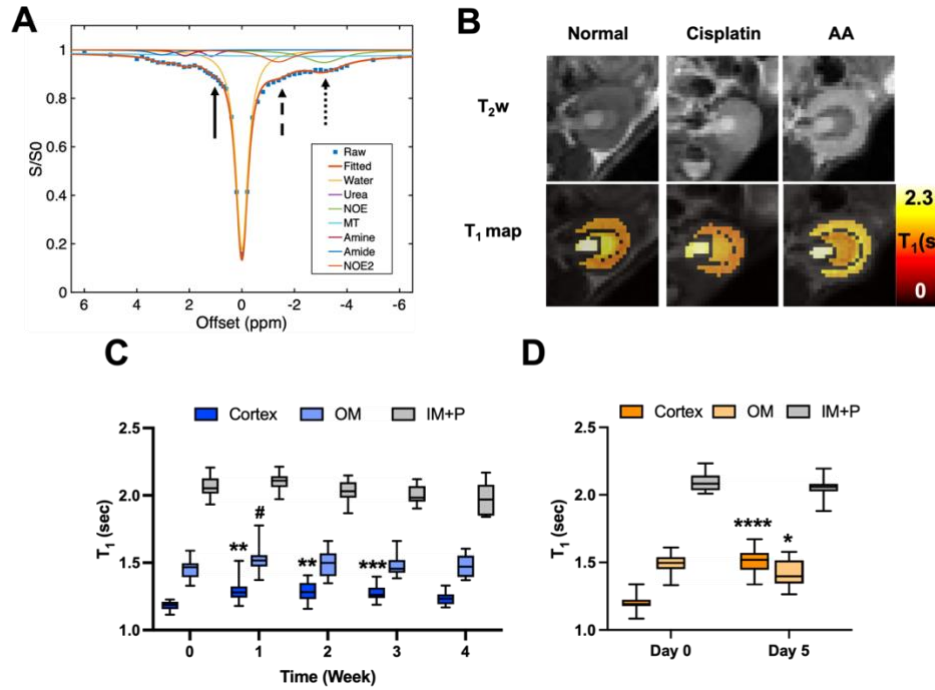
Figure 5.2 In vivo multi-parametric MRI results. (A) A representative Z-spectrum derived from a series of CEST-MR images and localized to the mouse cortex is analyzed via 7-pool Lorentzian fitting. Urea contrast at 1 ppm, NOE contrast at -1.6 ppm, and NOE contrast at -3.5 ppm are indicated by a solid arrow, dashed arrow, and dotted arrow, respectively. (B) Representative T_2-weighted (T_2w) anatomical images and T_1 maps of cisplatin and AA nephropathy models reveal structural and parametric changes induced by kidney injury. The AA group showed reversed contrast in the cortex and the outer medulla in T_2w images and increased T_1 times in the cortex as a function of injury, likely due to the expansion of the free water pool by tubular dilation. In parallel, T_1 times in the cortex and outer medulla increased significantly in both the cisplatin group (C) and the AA group (D) despite different manifestations of kidney injury. *#P<0.05, **P<0.01, ***P<0.001, ****P<0.0001 vs. week/day 0.

The renal response to the infusion of either urea or saline was further assessed by measuring the fold change of urea AREX contrast following infusion of either saline or urea (Figure 5.3C). The fold change of urea AREX contrast, either with an infusion of saline or urea, did not change over injury progression in the cisplatin group. The AA group, on the other hand, showed a decreased response in the cortex (1.433±0.456 to 0.993±0.319, P = 0.039) and the OM (1.556±0.406 to 0.951±0.337, P = 0.0055) compared to the baseline measurement. The saline infusion did not cause any changes in urea AREX contrast in both healthy and injured conditions.

On top of urea CEST, NOE CEST contrasts at -3.5 ppm and -1.6 ppm were also recorded from the full z-spectra and corrected for T_1 times via AREX (Figure 5.4). Similar to urea AREX results, the cisplatin group did not show significant changes in NOE contrasts at both -3.5 ppm and -1.6 ppm over time. The AA group showed significant decrease of NOE AREX at -3.5 ppm (0.104±0.014 to 0.076±0.012, P < 0.0001) and -1.6 ppm (0.096±0.021 to 0.072±0.011, P = 0.0001) in the cortex (Figure 5.4A). NOE AREX was preserved in other regions in the kidney. NOE AREX maps also show a significant decrease of contrast in the AA group while no change is observed from the cisplatin group (Figure 5.4B).
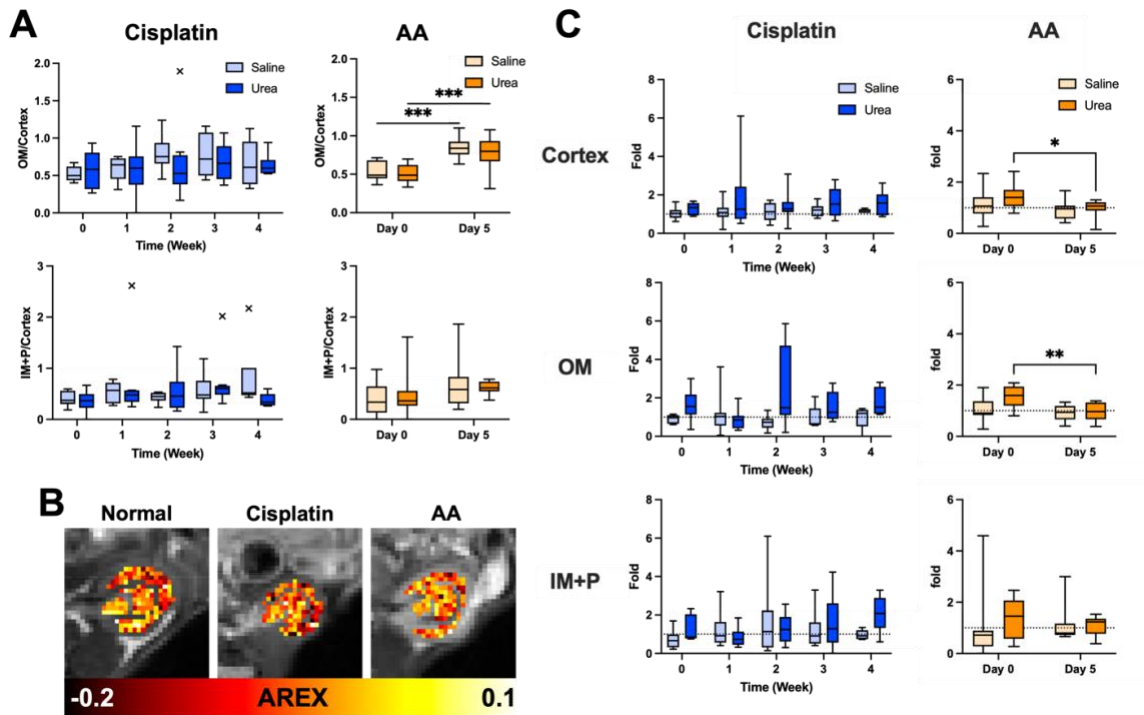
Figure 5.3 Urea CEST contrast measurements. (A) The spatial gradient of urea contrast was calculated by normalizing AREX measurements at the outer medulla (OM) and the inner medulla and papilla (IM+P) to the corresponding measurements at the cortex. Measurements of the spatial gradient of urea AREX in the cisplatin group showed no changes over time whereas the AA group showed a significant increase of normalized OM contrast from both saline and urea-infused subgroups. ***$P < 0.001$. (B) Representative Urea AREX maps of normal and diseased kidneys show preserved urea AREX contrast in the cisplatin group, while the AA group shows increased contrast in the OM, resulting in the decrease of contrast gradient between the cortex and OM. (C) The fold change of urea AREX upon infusion of either saline or urea was calculated by dividing the post-infusion urea AREX measurement by the pre-infusion measurement. The kidney response to urea or saline infusion did not change in the cisplatin group, while the AA group shows decreased fold change upon urea infusion in the cortex and OM at day 5. *$P < 0.05$, **$P < 0.01$.

Finally, qMT spectra were acquired at two saturation powers with 7 offset frequencies each and fitted to Ramani equation to extract a semi-solid macromolecular pool-size ratio (PSR; Figure 5.5A) [161]. In this study, the cisplatin group showed slight decreases of PSR in the cortex at weeks 2 (0.045 ± 0.005, $P = 0.0481$) and 3 ($0.04c\pm0.005$, $P = 0.0386$) compared to baseline measurements at week 0 (0.05 ± 0.005; Figure 5.5C). Much more significant decreases of PSR were detected from the AA group upon injury initiation in the cortex (0.047 ± 0.003 to 0.032 ± 0.005, $P < 0.0001$; Figure 5.5D). Both groups did not show any changes of PSR in other regions of the kidney. This trend of PSR decrease is again well represented in the qMT contrast maps shown in Figure 5.5B.

5.3.3 Comparing CEST and qMT parameters to histological analysis

After in vivo MR scans were complete the mice were euthanized and the kidneys were collected for histological analysis. Hematoxylin and eosin staining showed marked tubular

necrosis in the AA group and moderate areas of tubular atrophy in the cisplatin group (Figure 5.6A). Sirius red staining revealed interstitial fibrosis in the cisplatin group, whereas the AA group did not show significant changes in collagen content. Semi-quantitative histological scores also showed significantly larger extents of acute injuries, such as tubular necrosis (3.75 ± 0.87 vs. 1.00 ± 0.43, P = 0.001), degeneration (3.50 ± 0.90 vs. 1.50 ± 0.90, P = 0.0017), and dilation (3.67 ± 0.89 vs. 2.00 ± 0.74, P = 0.0038) in the AA group compared to the cisplatin group (Figure 5.6B). Chronic features of renal injuries such as tubular atrophy (1.92 ± 0.79 vs. 0.42 ± 0.51, P = 0.001) and interstitial fibrosis (1.50 ± 0.52 vs. 0.25 ± 0.45, P = 0.0002) were significantly more evident in the cisplatin group than the AA group. These histological scores were correlated with MR parameters that showed significant changes upon disease progression (Figure 5.7). Spearman rank correlation showed that PSR and NOE AREX at -1.6 ppm are negatively related to acute injuries and positively related to chronic injuries. The T_1 time in the cortex also showed a significant correlation to all the histological features, but in the opposite fashion: positively correlated to acute injuries and negatively correlated to chronic injuries. Urea AREX at the OM and NOE AREX at -3.5 ppm were only sensitive to acute injuries. As a visual representation of how multiparametric analysis can distinguish acute and chronic injuries, mouse histology data were clustered based on T_1, PSR, and urea AREX (Figure 5.7C). This clustering demonstrates that a combination of CEST and qMT parameters can clearly distinguish kidneys with acute injuries from those with chronic ones.
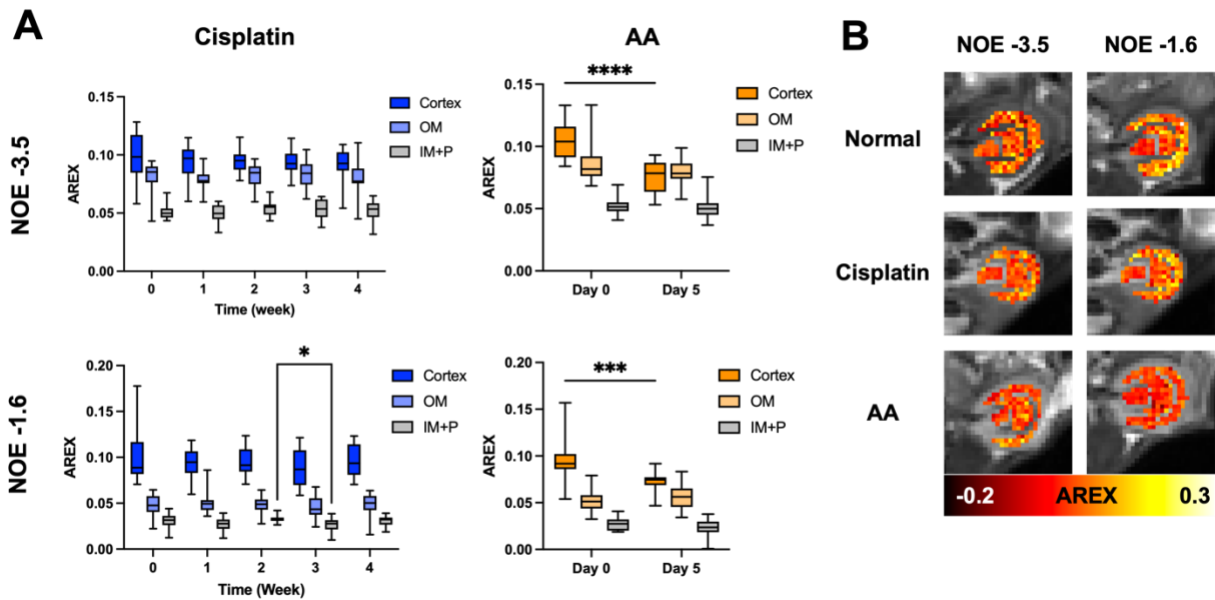
Figure 5.4 NOE CEST contrast measurements. (A) NOE AREX measurements at -3.5 and -1.6 ppm offset frequencies show no or little changes in the NOE contrast in the cisplatin group. The AA group, however, shows a significant decrease of contrast in the cortex at both -3.5 and -1.6 ppm, possibly due to the disruption of cellular membranes and alterations in mobile proteins. *P < 0.05, ***P < 0.001, ****P < 0.0001. (B) NOE AREX maps overlaid on T_2-weighted images. AA group shows a significant decrease of the contrast at both -3.5 and -1.6 ppm in the cortex compared to the normal mice.
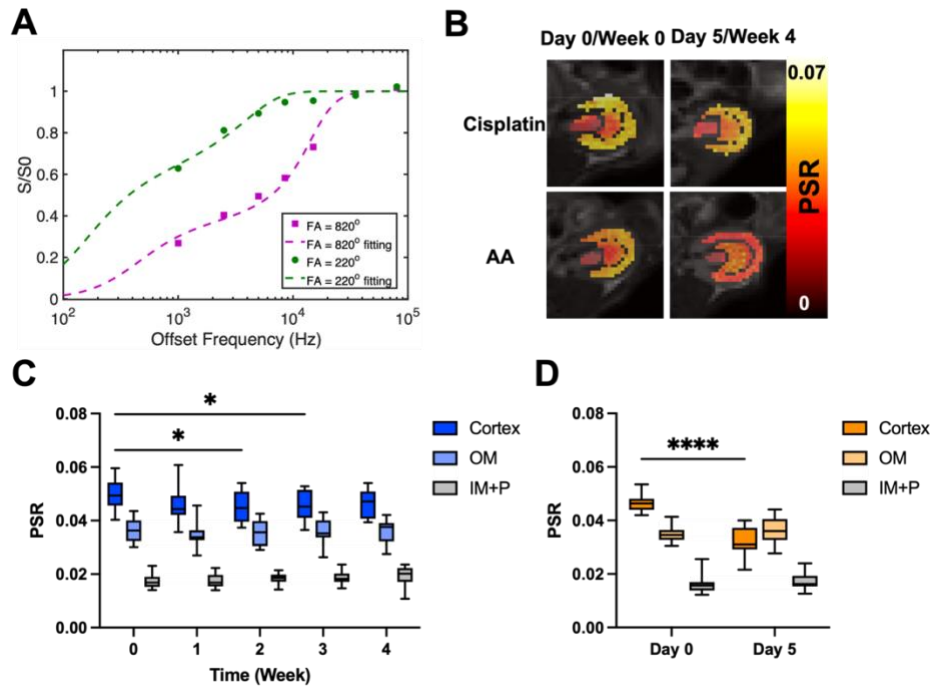
Figure 5.5. Quantitative magnetization transfer (qMT) imaging and pool-size ratio (PSR) measurements. (A) An example qMT spectra acquired at two saturation powers and 7 offset frequencies with fitting to the Ramani model. (B) PSR maps of cisplatin and AA group before and after inducing nephropathies. The cisplatin group shows a mild decrease of PSR contrast in the cortex, and the AA group shows a significant decrease in the same region. (C) PSR measurements over time from the cisplatin group shows a mild decrease of PSR in the cortex up to week 3, possibly due to the net sum effect of fibrosis development and acute injuries. *$P < 0.05$. (D) PSR measurements from the AA group show a large decrease of PSR in the cortex. Similar to the T_1 increase, this large decrease of PSR may be the consequence of the expansion of the free water pool from tubular injuries and subsequent decrease of relative semi-solid macromolecule pool. ****$P < 0.0001$.

5.4 Discussion

This study shows that multiparametric CEST-MRI and qMT imaging can quantitatively distinguish the differing pathologies of renal injuries induced by cisplatin and AA. Administration of Cisplatin and AA yielded vastly different patterns of disease progression as confirmed by blood tests and histology. This difference was well captured by our imaging method as different patterns of changes in urea and NOE CEST and qMT parameters. The relatively mild and chronic injuries induced by cisplatin showed changes only in T_1 times and PSR at the cortex from qMT, whereas the relatively acute and severe injuries shown in the AA model were reflected as significant changes of T_1, PSR, urea, and NOE CEST contrast. Correlation to histological scores revealed that CEST contrast from urea and NOE at -3.5 ppm are highly sensitive specifically to acute injuries, while other parameters were responsive to any types of injuries. These results collectively demonstrate the potential diagnostic value of our multiparametric CEST and qMT approach for noninvasively distinguishing different types of renal injuries and monitoring the progression of renal diseases.
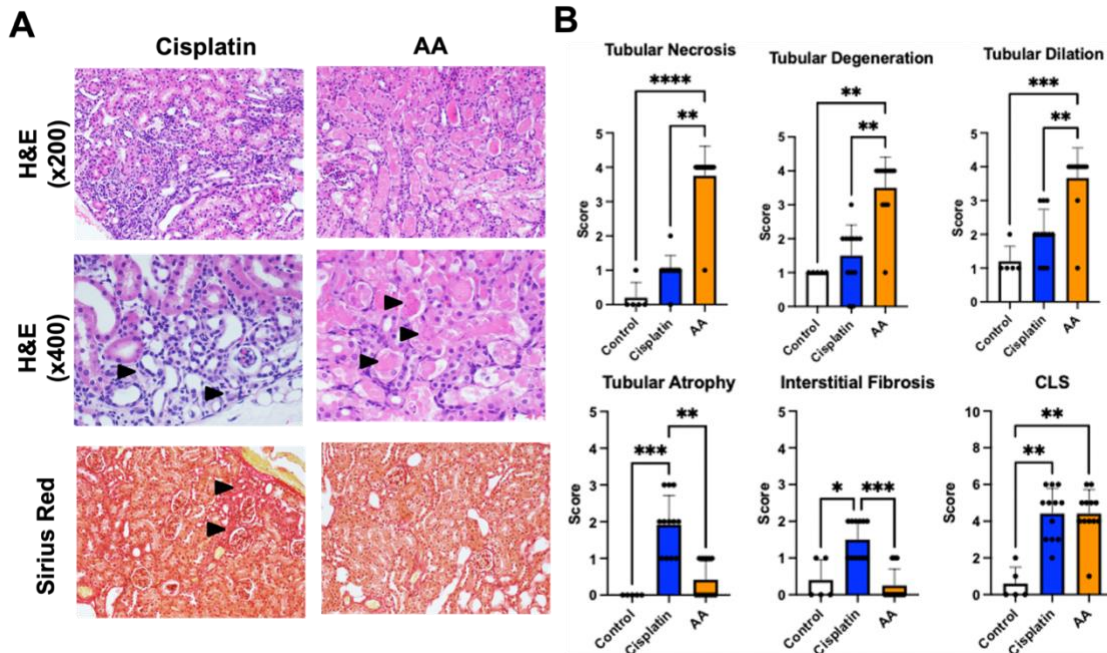
Figure 5.6 Histology and semi-quantitative scoring. (A) Hematoxylin and eosin (H&E) and Sirius red-stained sections of the kidneys. H&E-stained sections from the cisplatin group show multifocal tubular atrophy characterized by peritubular interstitial fibrosis and thickening of the basal lamina (Arrowheads). Arrowheads in the Sirius red sections also show focal interstitial fibrosis. H&E staining of the AA group shows marked areas of tubular necrosis, characterized by luminal accumulation of pyknotic cellular debris (Arrowheads). No interstitial fibrosis was observed from the Sirius red staining in the case of the AA group. (B) Semi-quantitative scoring of histology. The AA group shows significantly higher scores in tubular necrosis, degeneration, and dilation, which are considered the feature of acute injuries. The cisplatin group shows significantly higher scores from tubular atrophy and interstitial fibrosis, indicating more chronic development of renal injuries. $*P < 0.05$, $**P < 0.01$, $***P < 0.001$, $****P < 0.0001$.

We recently showed the feasibility of in vivo CEST imaging of urea in healthy mouse kidneys and further optimized the method to be more quantitative by correcting for the effects of regionally heterogeneous T_1 times on CEST contrast [152]. In this study, we tested whether this approach has diagnostic utility in renal diseases, especially focusing on whether it can distinguish differences between the two nephropathies. Our results show that both endogenous urea CEST contrast and the CEST response to the infusion of additional urea are sensitive to acute injuries induced by AA, whereas the cisplatin group did not show any changes. The correlation to histological scores also revealed that urea CEST is only sensitive to acute tubular injuries. Considering that the AA model showed significantly larger extents of tubular injuries than the cisplatin group, this observation may be due to the disruption of the urea gradient in the kidney, as a result of acute injuries on tubules on which urea transporters are expressed for urea recycling actions [10]. This is in line with previous studies on hyperpolarized ^{13}C imaging that showed a disrupted urea gradient in a mouse diabetic nephropathy model [126,162].

On top of urea CEST, NOE CEST and qMT imaging were also performed for a thorough investigation of renal injury progression. It was previously shown that NOE CEST contrast at -3.5 ppm decreases upon the development of sepsis-induced AKI in mice, which was replicated in our results [155]. We also tried to identify the histological origin of the decrease of NOE CEST contrast. Similar to urea CEST, NOE at -3.5 ppm showed a significant correlation only to acute injuries such as tubular necrosis, degeneration, and dilation. This may be due to the decrease in aliphatic

and olefinic protons in the tissue caused by disruption of the tubular cell membrane and reduced mitochondrial biogenesis leading to the loss of mobile macromolecules as previously shown [163,164]. The decrease of NOE CEST contrast may also be due to the loss of semi-solid macromolecules, which is supported by the decrease of qMT PSR observed in this study.
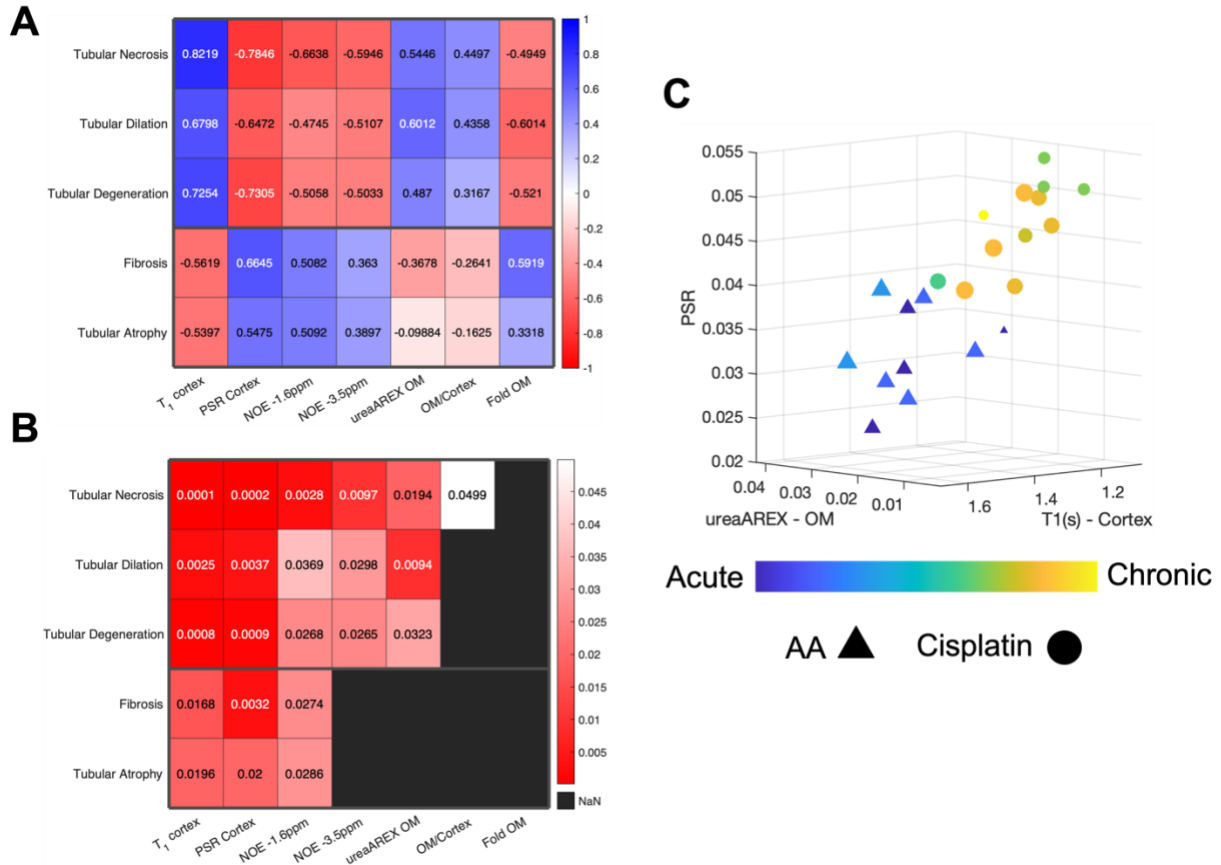
Figure 5.7 Correlation of CEST and qMT parameters to histology. Spearman correlation coefficients (A) and p-values (B) are shown. T_1, PSR, and NOE at -1.6 ppm in the cortex are sensitive to both acute and chronic injuries, whereas NOE at -3.5 ppm and urea AREX in the outer medulla (OM) are sensitive only to acute injuries. T_1 of the cortex is positively correlated to acute injuries and negatively to chronic ones, while PSR and NOE at -1.6 ppm show the opposite correlations. Black boxes in (B) indicate correlations that do not show statistical significance ($P > 0.05$). (C) An example multiparametric analysis of renal injuries. The combination of PSR, T_1 of the cortex, and urea AREX at the OM well distinguishes acute and chronic injuries. The size of data points indicates the overall severity of injuries as measured by cumulative layout shift (CLS) histological scores.

PSR from qMT imaging was previously shown to be an indicator of fibrosis development in the mouse and swine kidneys of various disease models including diabetic nephropathy and renal artery stenosis [159,160,165–167]. Similarly, we included a qMT scan protocol in this study to detect any fibrosis development from renal injuries via an increase of PSR. Paradoxically, the PSR measurements decreased in both cisplatin and AA groups, while the degree of decrease was much larger in the AA group. Since the AA group showed little or no development of fibrosis while showing severe tubular injuries, the decrease of PSR may arise from the insufficient development

58

of fibrosis with concurrent acute tubular injuries accompanied by the loss of semisolid macromolecules and the expansion of the free water pool via tubular dilation. This implies that both acute and chronic injuries alter PSR in either a decreasing or increasing fashion, respectively. Further, the PSR measurements may remain unchanged due to a combination of ongoing acute and chronic injuries. This implication is also supported by the fact that PSR measurements at week 4 in the cisplatin group did not show significant differences from the baseline measurements. As such, the counter-balancing effect of acute and chronic injuries demonstrates that the qMT imaging alone is not sufficient for accurately monitoring the renal tissue status and requires other MR parameters to complement the observations.

NOE contrast measured at -1.6 ppm is a recently discovered [132] CEST contrast. Although the origin of this contrast is largely unexplored, it has been shown that decreased contrast at -1.6ppm exists in regions of ischemic stroke in rats and has potential as a new imaging biomarker [168–171]. This novel contrast was also shown to be varying depending on the type of breathing gases for rats, suggesting the possibility that this contrast is oxygen level-dependent [134]. Since hypoxia is a common phenomenon in the diseased kidneys, we hypothesized that NOE at -1.6 ppm can also be a useful imaging target for probing renal tissue integrity [172,173]. The NOE at -1.6 ppm significantly decreased with the onset of injury from AA infusion, while the cisplatin group only showed minimal changes in the IM+P. Similar to NOE at -3.5 ppm, it is expected that the decrease is arising from the disruption of the tubular cell membrane as confirmed by the histology. Although the origin of the NOE at -1.6 ppm contrast should be further elucidated, the results indicate this contrast can be a useful imaging marker for observing renal diseases.

Some limitations of this study should be noted. Although we aimed to observe the progression of renal injuries toward the chronic end using the cisplatin model, histological findings suggest insufficient fibrosis development compared to previous mouse CKD models. Longer experiment timelines using mouse strains that are more vulnerable to cisplatin-induced injuries may induce more chronic injuries and enable investigation of how CEST and qMT parameters change at the chronic end of the spectrum of renal diseases [174–177]. In the CEST MRI perspective, the measurement of urea and NOE AREX is affected by the exchange rate of the target protons, which in turn is a function of the pH of the surrounding environment. Similar to T_1 times, intrarenal pH varies depending on the anatomical regions in the kidney, ranging from 7.0 to 6.6 from the cortex to IM+P [178]. Furthermore, it is likely that the pH of each kidney subregions change over disease progression [137]. Previous iopamidol CEST studies on mouse AKI models showed the increasing pH levels from 6.7 to 7.3 in the kidneys with disease progression [111,112]. This spatiotemporal change of pH should alter the exchange rate of the target protons and affect the CEST contrast, resulting in inaccurate estimation of renal function and tissue integrity loss. Several technical methods, such as numerical fitting of Bloch equations with different saturation times and saturation powers (QUEST/QUESP) and Omega plot analysis, can be considered for correcting the pH effects by quantifying exchange rates [146,147,179].

5.5 Materials & Methods

5.5.1 Mouse Renal Disease Models

All animal experiments were performed in accordance with the Institutional Animal Care and Use Committee guidelines. Cisplatin (Fresenius Kabi, Bad Homburg, Germany) was used for

inducing chronic and mild renal injuries, and aristolochic acid (AA; Acros Organics, Geel, Belgium) for acute and severe renal injuries. For the cisplatin group, 10-12-week-old male C57BL6/J mice (n = 26) were intraperitoneally injected with 10 mg/b.w. kg of cisplatin every week from week 0 to 3. Blood was collected every week for the measurement of blood urea nitrogen (BUN) and SCr (n = 10). The other mice (n = 16) were scanned every week up to week 4. Mice were infused with either 150 μL saline (n = 8) or 2M 150 μL urea (n = 8) during each scan to see renal response via urea CEST.

For the AA model, mice of the same age and species (n = 32) were i.p. injected with 5 mg/b.w. kg of AA dissolved in polyethylene glycol (Acros Organics) every day from day 0 to 4. Blood collection (n = 10) for BUN and SCr measurement and MR scans with saline (n = 10) or urea (n = 12) infusion were performed at days 0 and 5.

5.5.2 In vivo MRI Acquisition

MR scans were performed at 7T with a 40 mm volume coil (Bruker PharmaScan, Ettlingen, Germany). To tightly control diuretic states, every MR scan was initiated at ZT0 (7 AM) after 12-hour fasting. T_2-weighted images (RARE factor = 8, TR/TE = 2500/52 ms, NA = 2, slice thickness = 2 mm, field of view = 35 x 35 mm, Matrix = 256 x 256), T_1 maps (Inversion recovery, TR/TE = 4.3/2.1 ms, 15 TIs from 100 to 8000 ms, Matrix = 128 x 128), CEST Z-spectra (TR/TE = 7.4/3.1 ms, NA = 2, 59 offset frequencies, 70 0.6 μT 50-ms Gaussian sat pulses with duty cycle = 50%, Matrix= 128 x 128, 5 sec recovery time) were acquired before and 20 minutes after the infusion of saline or urea. During the acquisition of CEST z-spectra, reference images (-300 ppm offset) were acquired every 5 offset images for retrospective thermal drift correction [107,154]. B_0 and B_1 maps were acquired via water shift and B_1 (WASABI) method (3.7 μT, 5 ms-long continuous wave pulse, the same readout as CEST, 41 offset frequencies from -2 to 2 ppm), and MT-weighted images (FLASH, TR/TE = 24/2.5 ms, FA = 7°, NA= 24) at two saturation powers (flip angle = 220° and 820°, 10 ms Gaussian pulse) with seven offset frequencies each (1, 2.5, 5, 8.5, 15, 35, 80 kHz) were also acquired for qMT measurements. T_2-weighted images, T_1 maps, and CEST Z-spectra acquisition were repeated after infusion of either urea or saline.

5.5.3 CEST and qMT Data Analysis

All MR data analysis was performed by a custom-written code in MATLAB (Mathworks, Natick, MA). B_0 inhomogeneity was corrected voxel-wise using B_0 maps acquired from WASABI. Since B_1 maps showed minimal inhomogeneity, no B_1 correction was needed. After corrections, kidneys were segmented into the cortex, outer medulla (OM) and inner medulla and papilla (IM+P) by drawing region-of-interests (ROI) on T_2-weighted images and applying to CEST and qMT-weighted images. Using reference images that were periodically acquired during z-spectra acquisition, thermal drift was corrected by spline interpolation. Offset images showing severe motion artifacts were excluded from the analysis. ROI-averaged CEST z-spectra were fitted to 7-pool (water, MT, amine, amide, urea, NOE at -1.6 ppm and NOE at -3.5 ppm) Lorentzian functions as previously described [152]. After fitting to the sum of Lorentzian functions, the apparent exchange-dependent relaxation (AREX) method was applied to measure the T_1-corrected CEST contrast, which was used for all CEST contrast measurements [119]. Voxel-wise qMT spectra were fitted to a

two-pool Ramani equation to derive the PSR, the ratio of semi-solid macromolecule pool to free water pool [161].

5.5.4 Histology Analysis

Renal injuries were evaluated on paraffin-embedded sections with hematoxylin/eosin and Sirius red staining. Lesions were classified according to an adaptation of a previously published criterion and scored according to a 5-tier severity scale [129]. Tubular necrosis, atrophy, degeneration, and dilation: 0, normal; 1, minimal (less than 10% of tubules affected); 2, mild (10-30 % of tubules affected); 3, moderate (30 - 60 % of tubules affected); 4: marked (more than 60% of tubules affected). Fibrosis: 0, normal; 1, minimal (uncommon detection in <10% kidney fields (200x); 2, mild (detectable in up to 30% of kidney fields); 3, moderate (detectable in up to 30-60% of kidney fields); 4, marked (detectable in more than 60% of kidney fields). A final cumulative layout shift (CLS) score was created by the sum of tubular necrosis, atrophy, and fibrosis.

5.5.5 Statistical Analysis

All statistical analyses were performed using GraphPad Prism 9 (GraphPad Software, San Diego, CA). The normality of the data was confirmed by the Shapiro-Wilk test. BUN and SCr measurements were compared using one-way ANOVA for the cisplatin group and paired t-test for the AA group. Mixed-model effects analysis with Sidak's post-hoc test was performed for comparing MR measurements. Kruskall-Wallis test with Dunn's multiple comparison was used for analyzing histological scores, and Spearman's rank correlation coefficient was used for measuring the association between MR parameters and histological scores.

Chapter 6. Summary, Conclusions and Perspectives

6.1 Summary of Key Findings

Here, the feasibility of imaging urea with CEST MRI was shown, and the urea CEST acquisition and analysis methods were further optimized for better quantification via correction of T_1 effect and finer fitting to Lorentzian functions. Finally, this method was expanded to multiparametric CEST and tested in renal disease models, demonstrating the potential of distinguishing different nephropathies.

The first study was to characterize the properties of urea as a CEST contrast agent and test its feasibility of using in vivo. The in vitro characterization showed CEST contrast from urea at 1 ppm offset frequency from water, which can be well resolved at 7T. The CEST contrast from urea was well detected at the physiological concentrations at physiological pH range in the kidneys. In vivo imaging in mice detected significantly higher urea CEST contrast in the IM+P than other regions, which corresponds to the physiological urea gradient in the kidneys. The infusion of additional urea also increased the CEST contrast in the IM+P only, reflecting the urea recycling action by renal tubules.

In the second study, the urea CEST acquisition and analysis protocol was further optimized. The optimal time point for acquiring Z-spectra after infusing urea was explored, which turned out to be around 20 minutes. AREX method was implemented to remove the T_1 effect on the urea CEST contrast, which is the first time tested in the kidneys. Multi-Lorentzian modeling of Z-spectra was updated with adding more exchangeable proton pools, which resulted in more accurate measurement of urea CEST contrast. The CEST contrast also showed a significant correlation to the urea concentration of the kidney homogenate.

The updated CEST protocol was tested in mouse renal disease models in the last study. On top of urea CEST, two NOE pools from the Z-spectra were also investigated, as well as separate qMT spectra for probing mobile proteins and semi-solid macromolecules, respectively. These multiple molecular contrasts well correlated with specific histological features of renal injury models and distinguished two disease models tested.

Overall, the urea CEST approach that quantitatively probes urea recycling actions of renal tubules was established, and its potential of renal disease diagnosis was demonstrated through preclinical studies using mouse renal disease models. It is expected this molecular MR approach may enable investigation of microstructural changes in progressive renal disease patients upon successful clinical translation.

6.2 Perspectives of CEST imaging in the human kidneys

CEST is relatively a novel molecular MR technique (approximately two decades since its development) that is currently widely studied for various disease applications. Several subsets of CEST imaging, for instance amide proton transfer (APT) imaging, have shown promise in detecting and stratifying brain tumors in clinical studies[180]. Since CEST imaging is also studied for other various diseases as a method of diagnosis, guiding novel therapeutics, and measuring therapy response, it has a large potential to be used in clinics and a room for further development[181–183].

To further advance the urea CEST for renal imaging, better quantification of urea concentration is required. Although the T_1 effect on the CEST contrast was removed by adopting the AREX method, the effect of the exchange rate was not corrected. Considering the inherently different pH levels in the kidney subregions and the pH changes upon renal disease progression, the CEST contrast without exchange correction may lead to the inaccurate quantification of target molecules. Several approaches have been proposed for measuring exchange rates, such as QUEST/QUESP and Omega plot method, that allow measuring the exchange rate and the concentration of target exchangeable protons separately[146,179,184]. Adopting these techniques for multiparametric CEST imaging may be an interesting future study for improving the quantification of urea and aliphatic protons in the kidneys.

The specificity of urea CEST contrast is also an interesting topic to pursue in the future. So far, the CEST contrast at 1 ppm offset frequency was assumed to be originating solely from the urea. However, there are multiple metabolites in the kidney parenchyma and urine that also have exchangeable protons resonating at 1 ppm offset frequencies, including but not limited to myoinositol, glucose, allantoin, and alanine. Since the molecular signature of the CEST contrast was only assigned based on the offset resonant frequency, the CEST contrast at 1 ppm might represent the net sum of these metabolites, rather than urea alone. To further isolate the urea CEST effect, the slow exchange rate of urea may be leveraged via the variable delay multi-pulse (VDMP) method[115,116,185,186]. This method is based on varying the delay time between each saturation pulse so that the CEST contrast from slowly exchanging protons and that from fast exchanging protons can be separated. This adds another dimension of distinguishing metabolites other than offset frequencies so that the CEST effect from urea might be distinguished from other metabolites mentioned above.

In terms of the clinical translation of the urea CEST imaging, the safety profile of urea infusion to patients should be first established. Considering urea is commonly used as a food additive, it is expected to be safer than nephrotoxic CT agents or gadolinium-based MR contrast agents. Still, urea is also a waste product from protein metabolism that should be excreted and may induce carbamylation of proteins at high concentration[187,188]. However, as discussed in Chapter 5, the fold change of the urea CEST after the infusion of additional urea demonstrated the same utility as measuring the endogenous urea CEST in distinguishing different nephropathies. Thus, measuring the endogenous urea only may be sufficient for diagnostic purposes, which can be easily translated to human studies. Other molecules that represent renal excretory function may be explored as an exogenous CEST contrast agent. Inulin is a non-toxic polysaccharide that is used as a gold standard for measuring the GFR as it is neither reabsorbed nor secreted along the renal tubules[189]. If inulin turns out to be possessing appropriate CEST properties for imaging, then it may serve as a better substitute for urea as an exogenous CEST contrast agent that can be easily translated to clinical application. The lower field strength of clinical scanners is also an issue to be considered. All three studies presented here were performed at a 7T preclinical scanner, while 3T is the most commonly used field strength in clinical settings. Since the offset frequency of urea is only 1 ppm apart from the water resonant frequency, it should be tested whether the urea peak in a Z-spectrum can be well resolved from the water peak at lower field strengths. The saturation scheme and readout parameters also should be reoptimized based on the lower field strength.

Considering the clinical application of CEST imaging in general, the scan time for acquiring a Z-spectrum should be reduced. Acquiring a Z-spectrum means acquiring approximately 40 ~ 80 images with each image acquisition preceded by saturation pulses and followed by a delay time for T_1 recovery. This requires a long scan time, approximately 30 minutes

for urea CEST imaging described above. This acquisition time becomes even longer if the aforementioned methods for correcting the exchange rate effect are implemented as these methods require acquiring multiple z-spectra. Considering CEST imaging is ultimately expected to be used for disease patients, reducing the scan time is essential for patient experience. The CEST data acquisition may be accelerated in multiple ways, including undersampling of the k-space and reconstructing with a compressed sensing algorithm[190]. The long scan time also increases the chance that motion artifact arises in the images. Especially the organs in the chest and the abdomen—thus including the kidneys—are subject to heartbeat, breathing and peristaltic motions, which all contribute to motion artifacts. These artifacts subsequently generate noise in the z-spectra and prevent the accurate analysis of CEST contrast. A relatively motion-insensitive radial sampling scheme has been proposed to overcome this limit, but it is yet to be tested in the kidneys[191–193]. Lastly, a consensus in the CEST community is also needed for a standardized acquisition, processing, and analysis of CEST data. A recent study on breast tumor patients showed that the interpretation of CEST contrast can be completely different based on how the CEST data is analyzed[194]. As such, to guarantee the repeatability and robustness of CEST data, a saturation scheme adopted in an MR scanner should be replicated in another scanner, and a unified processing and analysis pipeline should be established for preparing a clinical standard of CEST imaging.

References

1.   Norris, T. L. & Lalchandani, R. *Porth's pathophysiology: concepts of altered health states*. (Lippincott Williams & Wilkins, 2018).

2.   Koeppen, B. M. & Stanton, B. A. *Renal Physiology E-Book: Mosby Physiology Monograph Series*. (Elsevier Health Sciences, 2012).

3.   Kidney Ultrasound | Johns Hopkins Medicine. https://www.hopkinsmedicine.org/health/treatment-tests-and-therapies/kidney-ultrasound.

4.   Widmaier, E. P., Raff, H. & Strang, K. T. *ISE Vander's Human Physiology*. (McGraw-Hill Education, 2018).

5.   Amerman, E. C. *Human anatomy & physiology*. (EBONY HOLT, 2021).

6.   Cockcroft, D. W. & Gault, H. Prediction of creatinine clearance from serum creatinine. *Nephron* **16**, 31–41 (1976).

7.   Levey, A. S. *et al.* A more accurate method to estimate glomerular filtration rate from serum creatinine: a new prediction equation. *Ann. Intern. Med.* **130**, 461–470 (1999).

8.   Yang, B. & Bankir, L. Urea and urine concentrating ability : new insights from studies in mice. *Am J Physiol Ren. Physiol* **288**, F881–F896 (2005).

9.   Bankir, L., Bouby, N., Trinh-Trang-Tan, M. M., Ahloulay, M. & Promeneur, D. Direct and indirect cost of urea excretion. *Kidney Int.* **49**, 1598–1607 (1996).

10.   Bankir, L., Chen, K. & Yang, B. Lack of UT-B in vasa recta and red blood cells prevents urea-induced improvement of urinary concentrating ability. *Am. J. Physiol. Renal Physiol.* **286**, F144–F151 (2004).

11.   Kellum, J. A. *et al.* Kidney disease: improving global outcomes (KDIGO) acute kidney injury work group. KDIGO clinical practice guideline for acute kidney injury. *Kidney Int. Suppl.* **2**, 1–138 (2012).

12.   Waikar, S. S., Murray, P. T. & Singh, A. K. *Core Concepts in Acute Kidney Injury*. (Springer, 2018).

13.   Susantitaphong, P. *et al.* World incidence of AKI: a meta-analysis. *Clin. J. Am. Soc. Nephrol.* **8**, 1482–1493 (2013).

14.   Hoste, E. A. J. *et al.* Epidemiology of acute kidney injury in critically ill patients: the multinational AKI-EPI study. *Intensive Care Med.* **41**, 1411–1423 (2015).

15.   Endre, Z. H. *et al.* Erythrocytes alter the pattern of renal hypoxic injury: predominance of proximal tubular injury with moderate hypoxia. *Clin. Sci.* **76**, 19–29 (1989).

16.   Zuk, A., Bonventre, J. V, Brown, D. & Matlin, K. S. Polarity, integrin, and extracellular matrix dynamics in the postischemic rat kidney. *Am. J. Physiol. Physiol.* **275**, C711–C731 (1998).

17.   Endre, Z. H. & Pickering, J. W. Cell cycle arrest biomarkers win race for AKI diagnosis. *Nat. Rev. Nephrol.* **10**, 683–685 (2014).

18.   Thurman, J. M., Lucia, M. S., Ljubanovic, D. & Holers, V. M. Acute tubular necrosis is characterized by activation of the alternative pathway of complement. *Kidney Int.* **67**, 524–530 (2005).

19.   Coca, S. G., Singanamala, S. & Parikh, C. R. Chronic kidney disease after acute kidney injury: a systematic review and meta-analysis. *Kidney Int.* **81**, 442–448 (2012).

20.   Chawla, L. S., Eggers, P. W., Star, R. A. & Kimmel, P. L. Acute Kidney Injury and Chronic Kidney Disease as Interconnected Syndromes. *N. Engl. J. Med.* **371**, 58–66

(2014).

21. Varrier, M., Forni, L. G. & Ostermann, M. Long-term sequelae from acute kidney injury: potential mechanisms for the observed poor renal outcomes. *Crit. care* **19**, 1–7 (2015).

22. Webster, A. C., Nagler, E. V., Morton, R. L. & Masson, P. Chronic Kidney Disease. *Lancet* **389**, 1238–1252 (2017).

23. Xie, Y. *et al.* Analysis of the Global Burden of Disease study highlights the global, regional, and national trends of chronic kidney disease epidemiology from 1990 to 2016. *Kidney Int.* **94**, 567–581 (2018).

24. Bikbov, B. *et al.* Global, regional, and national burden of chronic kidney disease, 1990–2017: a systematic analysis for the Global Burden of Disease Study 2017. *Lancet* **395**, 709–733 (2020).

25. Levey, A. S. *et al.* Definition and classification of chronic kidney disease: a position statement from Kidney Disease: Improving Global Outcomes (KDIGO). *Kidney Int.* **67**, 2089–2100 (2005).

26. Silverwood, R. J. *et al.* Association between younger age when first overweight and increased risk for CKD. *J. Am. Soc. Nephrol.* **24**, 813–821 (2013).

27. Cockwell, P. & Fisher, L.-A. The global burden of chronic kidney disease. *Lancet* **395**, 662–664 (2020).

28. Tovar-Palacio, C. *et al.* Proinflammatory gene expression and renal lipogenesis are modulated by dietary protein content in obese Zucker fa/fa rats. *Am. J. Physiol. Physiol.* **300**, F263–F271 (2011).

29. Venkatachalam, M. A., Weinberg, J. M., Kriz, W. & Bidani, A. K. Failed tubule recovery, AKI-CKD transition, and kidney disease progression. *J. Am. Soc. Nephrol.* **26**, 1765–1776 (2015).

30. Panizo, S. *et al.* Fibrosis in chronic kidney disease: pathogenesis and consequences. *Int. J. Mol. Sci.* **22**, 408 (2021).

31. Kalantar-Zadeh, K., Jafar, T. H., Nitsch, D., Neuen, B. L. & Perkovic, V. Chronic kidney disease. *Lancet* **398**, 786–802 (2021).

32. Koppe, L. & Fouque, D. The role for protein restriction in addition to renin-angiotensin-aldosterone system inhibitors in the management of CKD. *Am. J. Kidney Dis.* **73**, 248–257 (2019).

33. National data - OPTN. https://optn.transplant.hrsa.gov/data/view-data-reports/national-data/#.

34. Matas, A. J. *et al.* OPTN/SRTR 2013 Annual Data Report: Kidney. *Am J Transpl.* **15**, 1–34 (2015).

35. Williams, W. W., Taheri, D., Tolkoff-rubin, N. & Colvin, R. B. Clinical role of the renal transplant biopsy. *Nat Rev Nephrol* **8**, 110–121 (2012).

36. Mannon, R. B. Delayed Graft Function : The AKI of Kidney Transplantation. **35294**, 94–98 (2018).

37. Nankivell, B. J. & Kuypers, D. R. J. Organ Transplantation 3 Diagnosis and prevention of chronic kidney allograft loss. *Lancet* **378**, 1428–1437 (2011).

38. Riella, L. V, Djamali, A. & Pascual, J. Chronic allograft injury : Mechanisms and potential treatment targets. *Transplant. Rev.* **31**, 1–9 (2017).

39. Bohl, D. L. & Brennan, D. C. BK virus nephropathy and kidney transplantation. *Clin. J. Am. Soc. Nephrol.* **2**, (2007).

40. Josephson, M. A. Monitoring and Managing Graft Health in the Kidney Transplant

Recipient. **6**, (2011).

41. Ostermann, M. & Joannidis, M. Acute kidney injury 2016: Diagnosis and diagnostic workup. *Crit. Care* **20**, 1–13 (2016).

42. Vaidya, V. S. *et al.* Kidney injury molecule-1 outperforms traditional biomarkers of kidney injury in preclinical biomarker qualification studies. *Nat. Biotechnol.* **28**, 478–485 (2010).

43. Yu, Y. *et al.* Urinary biomarkers trefoil factor 3 and albumin enable early detection of kidney tubular injury. *Nat. Biotechnol.* **28**, 470–477 (2010).

44. Tomson, C. R. V. Indications for renal biopsy in chronic kidney disease. *Clin. Med. (Northfield. Il).* **3**, 513 (2003).

45. Choi, B. S. *et al.* Clinical significance of an early protocol biopsy in living-donor renal transplantation: ten-year experience at a single center. *Am. J. Transplant.* **5**, 1354–1360 (2005).

46. Furness, P. N. *et al.* Protocol biopsy of the stable renal transplant: a multicenter study of methods and complication rates. *Transplantation* **76**, 969–973 (2003).

47. Agarwal, S. K., Sethi, S. & Dinda, A. K. Basics of kidney biopsy: A nephrologist's perspective. *Indian J. Nephrol.* **23**, 243 (2013).

48. Luciano, R. L. & Moeckel, G. W. Update on the Native Kidney Biopsy : Core Curriculum 2019. *Am. J. Kidney Dis.* **73**, 404–415 (2019).

49. Shah, S., Elder, M. A. & Hata, J. Case Report: A Rare Presentation of NSAID-Induced Secondary Membranous Nephropathy in a Pediatric Patient . *Frontiers in Pediatrics* vol. 9 (2021).

50. O'Neill, W. C. Renal relevant radiology: Use of ultrasound in kidney disease and nephrology procedures. *Clin. J. Am. Soc. Nephrol.* **9**, 373–381 (2014).

51. O'Neill, W. C. Sonographic evaluation of renal failure. *Am. J. kidney Dis.* **35**, 1021–1038 (2000).

52. Raj, D. S. C., Hoisala, R., Somiah, S., Sheeba, S. D. & Yeung, M. Quantitation of change in the medullary compartment in renal allograft by ultrasound. *J. Clin. ultrasound* **25**, 265–269 (1997).

53. Faubel, S., Patel, N. U., Lockhart, M. E. & Cadnapaphornchai, M. A. Renal relevant radiology: Use of ultrasonography in patients with AKI. *Clin. J. Am. Soc. Nephrol.* **9**, 382–394 (2014).

54. Schnell, D. & Darmon, M. Bedside Doppler ultrasound for the assessment of renal perfusion in the ICU : advantages and limitations of the available techniques. *Crit. Ultrasound J.* **7**, 8 (2015).

55. Dorze, M. Le, Bougle, A. & Duranteau, J. RENAL DOPPLER ULTRASOUND : A NEW TOOL TO ASSESS RENAL PERFUSION IN CRITICAL ILLNESS. **37**, 360–365 (2012).

56. Vasbinder, G. B. Diagnostic tests for renal artery stenosis in patients suspected of having renovasclar hypertension: A metaanalysis. *Ann Intern Med* **135**, 401411 (2001).

57. Mititelu, R. & Bratu, O. Radionuclide Imaging . An Update on the Use of Dynamic Renal Scintigraphy. **24**, 199–203 (2017).

58. Aktaş, A. Transplanted kidney function evaluation. in *Seminars in Nuclear Medicine* vol. 44 129–145 (Elsevier, 2014).

59. Upputalla, R., Moore, R. M. & Jim, B. Spontaneous forniceal rupture in pregnancy. *Case Reports Nephrol.* **2015**, (2015).

60. Hasebroock, K. M. & Serkova, N. J. Toxicity of MRI and CT contrast agents. *Expert Opin Drug Metab Toxicol* **5**, 403–416 (2009).

61. Davenport, M. S. *et al.* Contrast material-induced nephrotoxicity and intravenous low-osmolality iodinated contrast material. *Radiology* **267**, 94–105 (2013).

62. Sharfuddin, A. Renal relevant radiology: Imaging in kidney transplantation. *Clin. J. Am. Soc. Nephrol.* **9**, 416–429 (2014).

63. Elzanaty, A. *et al.* Intra-Arterial Hemodynamics to Guide the Percutaneous Treatment of a Difficult-to-Engage Transplant Renal Artery Stenosis. *Cardiovasc. Revascularization Med.* **21**, 171–173 (2020).

64. Loubeyre, P. *et al.* Transplant renal artery stenosis: evaluation of diagnosis with magnetic resonance angiography compared with color duplex sonography and arteriography. *Transplantation* **62**, 446–450 (1996).

65. Grobner, T. & Prischl, F. C. Gadolinium and nephrogenic systemic fibrosis. *Kidney Int.* **72**, 260–264 (2007).

66. Marckmann, P. *et al.* Nephrogenic systemic fibrosis: Suspected causative role of gadodiamide used for contrast-enhanced magnetic resonance imaging. *J. Am. Soc. Nephrol.* **17**, 2359–2362 (2006).

67. Grenier, N., Merville, P. & Combe, C. Radiologic imaging of the renal parenchyma structure and function. *Nat. Rev. Nephrol.* **12**, 348–359 (2016).

68. Nishimura, D. G. *Principles of magnetic resonance imaging*. (Stanford University, 1996).

69. Brown, R. W. *et al.* Magnetic Resonance Imaging : Physical Principles and Sequence Design Second Edition.

70. Bernstein, M. A., King, K. F. & Zhou, X. J. *Handbook of MRI pulse sequences*. (Elsevier, 2004).

71. Wu, B. *et al.* An overview of CEST MRI for non-MR physicists. *EJNMMI Phys.* **3**, (2016).

72. van Zijl, P. C. M., Lam, W. W., Xu, J., Knutsson, L. & Stanisz, G. J. Magnetization Transfer Contrast and Chemical Exchange Saturation Transfer MRI. Features and analysis of the field-dependent saturation spectrum. *Neuroimage* 1–20 (2017) doi:10.1016/j.neuroimage.2017.04.045.

73. Guivel-Scharen, V., Sinnwell, T., Wolff, S. D. & Balaban, R. S. Detection of proton chemical exchange between metabolites and water in biological tissues. *J. Magn. Reson.* **133**, 36–45 (1998).

74. Vinogradov, E., Sherry, A. D. & Lenkinski, R. E. CEST : From basic principles to applications , challenges and opportunities. *J. Magn. Reson.* **229**, 155–172 (2013).

75. Zaiss, M., Ehses, P. & Scheffler, K. Snapshot-CEST: Optimizing spiral-centric-reordered gradient echo acquisition for fast and robust 3D CEST MRI at 9.4 T. *NMR Biomed.* **31**, 1–14 (2018).

76. Zaiss, M. & Bachert, P. Chemical exchange saturation transfer (CEST) and MR Z-spectroscopy in vivo : a review of theoretical approaches and methods Chemical exchange saturation transfer (CEST) and MR Z -spectroscopy in vivo : a review of theoretical. doi:10.1088/0031-9155/58/22/R221.

77. Zaiß, M., Schmitt, B. & Bachert, P. Quantitative separation of CEST effect from magnetization transfer and spillover effects by Lorentzian-line-fit analysis of z-spectra. **211**, 149–155 (2011).

78. Jones, K. M., Pollard, A. C. & Pagel, M. D. Clinical Applications of Chemical Exchange

Saturation Transfer (CEST) MRI. *J Magn Reson Imaging* **47**, 11–27 (2018).

79. Van Zijl, P. C. M. & Yadav, N. N. Chemical exchange saturation transfer (CEST): What is in a name and what isn't? *Magn. Reson. Med.* **65**, 927–948 (2011).

80. Roeloffs, V., Meyer, C., Bachert, P. & Zaiss, M. Towards quantification of pulsed spinlock and CEST at clinical MR scanners: An analytical interleaved saturation-relaxation (ISAR) approach. *NMR Biomed.* **28**, 40–53 (2015).

81. Kim, M., Gillen, J., Landman, B. A., Zhou, J. & Van Zijl, P. C. M. Water saturation shift referencing (WASSR) for chemical exchange saturation transfer (CEST) experiments. *Magn. Reson. Med.* **61**, 1441–1450 (2009).

82. Windschuh, J. *et al.* Correction of B1-inhomogeneities for relaxation-compensated CEST imaging at 7T. *NMR Biomed.* **28**, 529–537 (2015).

83. Zhou, J., Heo, H. Y., Knutsson, L., van Zijl, P. C. M. & Jiang, S. APT-weighted MRI: Techniques, current neuro applications, and challenging issues. *J. Magn. Reson. Imaging* **50**, 347–364 (2019).

84. Zhou, J., Hong, X., Zhao, X., Gao, J. H. & Yuan, J. APT-weighted and NOE-weighted image contrasts in glioma with different RF saturation powers based on magnetization transfer ratio asymmetry analyses. *Magn. Reson. Med.* **70**, 320–327 (2013).

85. Wang, F. *et al.* Mapping murine diabetic kidney disease using chemical exchange saturation transfer MRI. *Magn. Reson. Med.* **76**, 1531–1541 (2016).

86. Deshmane, A. *et al.* 3D gradient echo snapshot CEST MRI with low power saturation for human studies at 3T. *Magn. Reson. Med.* **81**, 2412–2423 (2019).

87. Stevens, L. A., Coresh, J., Greene, T. & Levey, A. S. Assessing Kidney Function — Measured and Estimated Glomerular Filtration Rate. *N. Engl. J. Med.* **354**, 2473–2483 (2006).

88. Ebrahimi, B., Textor, S. C. & Lerman, L. O. Renal relevant radiology: Renal functional magnetic resonance imaging. *Clin. J. Am. Soc. Nephrol.* **9**, 395–405 (2014).

89. Sourbron, S. P., Michaely, H. J., Reiser, M. F. & Schoenberg, S. O. MRI-measurement of perfusion and glomerular filtration in the human kidney with a separable compartment model. *Invest. Radiol.* **43**, 40–48 (2008).

90. Heaf, J. G. & Iversen, J. Review article Uses and limitations of renal scintigraphy in renal transplantation monitoring. *Eur J Nucl Med* **27**, 871–879 (2000).

91. Durand, E. & Chaumet-riffaud, P. Functional Renal Imaging : New Trends in Radiology and Nuclear Medicine. *Semin Nucl Med* **41**, 61–72 (2011).

92. Maril, N. *et al.* Sodium MRI of the human kidney at 3 tesla. *Magn. Reson. Med.* **56**, 1229–1234 (2006).

93. von Morze, C., Bok, R. A., Sands, J. M., Kurhanewicz, J. & Vigneron, D. B. Monitoring urea transport in rat kidney in vivo using hyperpolarized 13C magnetic resonance imaging. *Am. J. Physiol. Renal Physiol.* **302**, F1658–F1662 (2012).

94. Maril, N., Margalit, R., Mispelter, J. & Degani, H. Sodium Magnetic Resonance Imaging of Diuresis : Spatial and Kinetic Response. *Magn Reson Med* **552**, 545–552 (2005).

95. Maril, N., Margalit, R., Rosen, S., Heyman, S. N. & Degani, H. Detection of evolving acute tubular necrosis with renal 23Na MRI: Studies in rats. *Kidney Int.* **69**, 765–768 (2006).

96. Atthe, B. K. *et al.* Early monitoring of acute tubular necrosis in the rat kidney by Na-MRI. *Am. J. Physiol. Renal Physiol.* **297**, F1288–F1298 (2009).

97. Weiner, I. D., Mitch, W. E. & Sands, J. M. Urea and ammonia metabolism and the control

of renal nitrogen excretion. *Clin. J. Am. Soc. Nephrol.* **10**, 1444–1458 (2015).

98.   Schmidt, C., Höcherl, K. & Bucher, M. Cytokine-mediated regulation of urea transporters during experimental endotoxemia. *Am. J. Physiol. Renal Physiol.* **292**, F1479–F1489 (2007).

99.   Terreno, E., Delli, D. & Aime, S. Encoding the frequency dependence in MRI contrast media : the emerging class of CEST agents. *Contrast Media Mol Imaging* **5**, 78–98 (2010).

100.   Liu, G. *et al.* In Vivo Multicolor Molecular MR Imaging Using Diamagnetic Chemical Exchange Saturation Transfer Liposomes. *Magn Reson Med* **67**, 1106–1113 (2012).

101.   Dagher, A. P., Aletras, A., Choyke, P. & Balaban, R. S. Imaging of urea using chemical exchange-dependent saturation transfer at 1.5 T. *J. Magn. Reson. Imaging* **12**, 745–748 (2000).

102.   Vinogradov, E. *et al.* Endogenous Urea CEST (urCEST) for MRI monitoring of kidney function. *Proc Intl Soc Magn Reson Med* 3375 (2015).

103.   Stancanello, J. *et al.* Development and validation of a smoothing-splines-based correction method for improving the analysis of CEST-MR images. *Contrast Media Mol. Imaging* **3**, 136–149 (2008).

104.   Liu, G. *et al.* Non-invasive temperature mapping using temperature-responsive water saturation shift referencing (T-WASSR) MRI. *NMR Biomed* **27**, 320–331 (2014).

105.   Jiang, T. *et al.* Generation and phenotypic analysis of mice lacking all urea transporters. *Kidney Int.* **91**, 338–351 (2017).

106.   Reed, G. D. *et al.* Imaging Renal Urea Handling in Rats at Millimeter Resolution Using Hyperpolarized Magnetic Resonance Relaxometry. *Tomography* **2**, 125–137 (2016).

107.   Desmond, K. L., Moosvi, F. & Stanisz, G. J. Mapping of amide, amine, and aliphatic peaks in the CEST spectra of murine xenografts at 7 T. *Magn. Reson. Med.* **71**, 1841–1853 (2014).

108.   Windschuh, J. *et al.* Assessment of frequency drift on CEST MRI and dynamic correction: Application to gagCEST at 7 T. *Magn Reson Med* **81**, 573–582 (2019).

109.   Zaiss, M. *et al.* Possible artifacts in dynamic CEST MRI due to motion and field shifts. *J Magn Reson* **298**, 16–22 (2019).

110.   Wu, Y. *et al.* A generalized ratiometric chemical exchange saturation transfer (CEST) MRI approach for mapping renal pH using iopamidol. *Magn. Reson. Med.* **79**, 1553–1558 (2018).

111.   Longo, D. L., Busato, A., Lanzardo, S., Antico, F. & Aime, S. Imaging the pH evolution of an acute kidney injury model by means of iopamidol, a MRI-CEST pH-responsive contrast agent. *Magn. Reson. Med.* **70**, 859–864 (2013).

112.   Longo, D. L., Cutrin, J. C., Michelotti, F., Irrera, P. & Aime, S. Noninvasive evaluation of renal pH homeostasis after ischemia reperfusion injury by CEST-MRI. *NMR Biomed.* **30**, 1–8 (2017).

113.   Longo, D. L. *et al.* Iopamidol as a Responsive MRI-Chemical Exchange Saturation Transfer Contrast Agent for pH Mapping of Kidneys : In Vivo Studies in Mice at 7 T. *Magn Reson Med* **65**, 202–211 (2011).

114.   Finer, E. G., Franks, F. & Tait, M. J. Nuclear Magnetic Resonance Studies of Aqueous Urea Solutions. *J. Am. Chem. Soc.* **94**, 4424–4429 (1972).

115.   Xu, J. *et al.* Variable Delay Multi-Pulse Train for Fast Chemical Exchange Saturation Transfer and Relayed-Nuclear Overhauser Enhancement MRI. *Magn Reson Med* **71**,

1798–1812 (2014).

116. Chen, L. *et al.* Separating fast and slow exchange transfer and magnetization transfer using off-resonance variable-delay multiple-pulse (VDMP) MRI. *Magn Reson Med* **80**, 1568–1576 (2018).

117. Stabinska, J. *et al.* Proton exchange in aqueous urea solutions measured by water-exchange (WEX) NMR spectroscopy and chemical exchange saturation transfer (CEST) imaging in vitro. *Magn. Reson. Med.* **82**, 935–947 (2019).

118. Hueper, K. *et al.* T1-mapping for assessment of ischemia-induced acute kidney injury and prediction of chronic kidney disease in mice. *Eur. Radiol.* **24**, 2252–2260 (2014).

119. Zaiss, M. *et al.* Inverse Z-spectrum analysis for spillover-, MT-, and T1-corrected steady-state pulsed CEST-MRI - application to pH-weighted MRI of acute stroke. *NMR Biomed.* **27**, 240–252 (2014).

120. van Zijl, P. C. M., Lam, W. W., Xu, J., Knutsson, L. & Stanisz, G. J. Magnetization Transfer Contrast and Chemical Exchange Saturation Transfer MRI. Features and analysis of the field-dependent saturation spectrum. *Neuroimage* **168**, 222–241 (2018).

121. Xu, X. *et al.* Dynamic glucose enhanced (DGE) MRI for combined imaging of blood-brain barrier break down and increased blood volume in brain cancer. *Magn. Reson. Med.* **74**, 1556–1563 (2015).

122. Xu, X. *et al.* Dynamic Glucose-Enhanced (DGE) MRI: Translation to Human Scanning and First Results in Glioma Patients. *Tomography* **1**, 105–114 (2015).

123. Sands, J. M. Regulation of Renal Urea Transporters. *J Am Soc Nephrol* **10**, 635–646 (1999).

124. Atta, M. G. Diagnosis and Natural History of HIV-Associated Nephropathy. *Adv. Chronic Kidney Dis.* **17**, 52–58 (2010).

125. John, R. & Herzenberg, A. M. Our approach to a renal transplant biopsy. *J. Clin. Pathol.* **63**, 26–37 (2010).

126. Zhang, X. *et al.* Diabetes induced renal urea transport alterations assessed with 3D hyperpolarized 13 C, 15 N-Urea. *Magn. Reson. Med.* **77**, 1650–1655 (2016).

127. Knutsson, L., Xu, J., Ahlgren, A. & van Zijl, P. C. M. CEST, ASL, and magnetization transfer contrast: How similar pulse sequences detect different phenomena. *Magn. Reson. Med.* **80**, 1320–1340 (2018).

128. Shin, S. H. *et al.* Noninvasive imaging of renal urea handling by CEST-MRI. *Magn. Reson. Med.* **83**, 1034–1044 (2020).

129. Baudoux, T. E. R. *et al.* Probenecid prevents acute tubular necrosis in a mouse model of aristolochic acid nephropathy. *Kidney Int.* **82**, 1105–1113 (2012).

130. Windschuh, J. *et al.* Correction of B1-inhomogeneities for relaxation-compensated CEST imaging at 7T. *NMR Biomed.* **28**, 529–537 (2015).

131. Missbach-Guentner, J. *et al.* 3D virtual histology of murine kidneys -high resolution visualization of pathological alterations by micro computed tomography. *Sci. Rep.* **8**, 1–14 (2018).

132. Zhang, X. Y. *et al.* A new NOE-mediated MT signal at around -1.6 ppm for detecting ischemic stroke in rat brain. *Magn. Reson. Imaging* **34**, 1100–1106 (2016).

133. Zhang, X. Y. *et al.* MR imaging of a novel NOE-mediated magnetization transfer with water in rat brain at 9.4 T. *Magn. Reson. Med.* **78**, 588–597 (2017).

134. Zu, Z. Toward more reliable measurements of NOE effects in CEST spectra at around −1.6 ppm (NOE (−1.6)) in rat brain. *Magn. Reson. Med.* **81**, 208–219 (2019).

135. Moon, B. F. *et al.* A comparison of iopromide and iopamidol, two acidoCEST MRI contrast media that measure tumor extracellular pH. *Contrast Media Mol. Imaging* **10**, 446–455 (2015).

136. Lindeman, L. R. *et al.* A comparison of exogenous and endogenous CEST MRI methods for evaluating in vivo pH. *Magn. Reson. Med.* **79**, 2766–2772 (2018).

137. Pavuluri, K. D. *et al.* Noninvasive monitoring of chronic kidney disease using pH and perfusion imaging. *Sci. Adv.* **5**, 1–11 (2019).

138. Zaiss, M. *et al.* Relaxation-compensated CEST-MRI of the human brain at 7T: Unbiased insight into NOE and amide signal changes in human glioblastoma. *Neuroimage* **112**, 180–188 (2015).

139. Reed, G. D. *et al.* High Resolution 13C MRI With Hyperpolarized Urea: In Vivo T2 Mapping and 15N Labeling Effects. *IEEE Trans. Med. Imaging* **33**, 362–371 (2014).

140. Xu, X. *et al.* Dynamic Glucose-Enhanced (DGE) MRI: Translation to Human Scanning and First Results in Glioma Patients. *Tomography* **1**, 105–114 (2015).

141. Xu, X. *et al.* d-glucose weighted chemical exchange saturation transfer (glucoCEST)-based dynamic glucose enhanced (DGE) MRI at 3T: early experience in healthy volunteers and brain tumor patients. *Magn. Reson. Med.* **84**, 247–262 (2020).

142. Jones, C. K. *et al.* Nuclear Overhauser enhancement (NOE) imaging in the human brain at 7T. *Neuroimage* **77**, 114–124 (2013).

143. Raghunand, N., Howison, C., Sherry, A. D., Zhang, S. & Gillies, R. J. Renal and systemic pH imaging by contrast-enhanced MRI. *Magn. Reson. Med.* **49**, 249–257 (2003).

144. Longo, D. L. *et al.* A General MRI-CEST Ratiometric Approach for pH Imaging: Demonstration of in Vivo pH Mapping with Iobitridol. *J Am Chem Soc* **136**, 14333–14336 (2014).

145. Finer, E. G., Franks, F. & Tait, M. J. Nuclear Magnetic Resonance Studies of Aqueous Urea Solutions. *J Am Chem Soc* **94**, 4424–4429 (1972).

146. Dixon, W. T. *et al.* A concentration-independent method to measure exchange rates in PARACEST agents. *Magn. Reson. Med.* **63**, 625–632 (2010).

147. Meissner, J. E. *et al.* Quantitative pulsed CEST-MRI using Ω-plots. *NMR Biomed.* **28**, 1196–1208 (2015).

148. Morozumi, K. *et al.* Recurrent glomerular disease after kidney transplantation: an update of selected areas and the impact of protocol biopsy. *Nephrology (Carlton).* **19**, 6–10 (2014).

149. Chawla, L. S. & Kimmel, P. L. Acute kidney injury and chronic kidney disease: An integrated clinical syndrome. *Kidney Int.* **82**, 516–524 (2012).

150. Gameiro, J., Marques, F. & Lopes, J. A. Long-term consequences of acute kidney injury: A narrative review. *Clin. Kidney J.* **14**, 789–804 (2021).

151. Liu, G., Song, X., Chan, K. W. Y. & Mcmahon, M. T. Nuts and Bolts of CEST MR imaging. *NMR Biomed* **26**, 810828 (2013).

152. Shin, S. H., Wendland, M. F. & Vandsburger, M. H. Delayed urea differential enhancement CEST (dudeCEST)-MRI with T1 correction for monitoring renal urea handling. *Magn. Reson. Med.* **85**, 2791–2804 (2021).

153. Wu, Y. *et al.* A generalized ratiometric chemical exchange saturation transfer (CEST) MRI approach for mapping renal pH using iopamidol. *Magn. Reson. Med.* **79**, 1553–1558 (2018).

154. Jones, C. K. *et al.* Nuclear Overhauser enhancement (NOE) imaging in the human brain at

7T. *Neuroimage* **77**, 114–124 (2013).

155. Liu, J. *et al.* CEST MRI of sepsis-induced acute kidney injury. 1–11 (2018) doi:10.1002/nbm.3942.

156. Wang, F. *et al.* Mapping Murine Diabetic Kidney Disease Using Chemical Exchange Saturation Transfer MRI. **00**, 1–11 (2015).

157. Sled, J. G. & Pike, G. B. Quantitative Interpretation of Magnetization Transfer in Spoiled Gradient Echo MRI Sequences. *J. Magn. Reson.* **145**, 24–36 (2000).

158. Sled, J. G. & Bruce Pike, G. Quantitative imaging of magnetization transfer exchange and relaxation properties in vivo using MRI. *Magn. Reson. Med.* **46**, 923–931 (2001).

159. Wang, F. *et al.* Assessment of renal fibrosis in murine diabetic nephropathy using quantitative magnetization transfer MRI. *Magn. Reson. Med.* **80**, 2655–2669 (2018).

160. Wang, F. *et al.* Noninvasive quantitative magnetization transfer MRI reveals tubulointerstitial fibrosis in murine kidney. *NMR Biomed.* **32**, 1–13 (2019).

161. Ramani, A., Dalton, C., Miller, D. H., Tofts, P. S. & Barker, G. J. Precise estimate of fundamental in-vivo MT parameters in human brain in clinically feasible times. *Magn. Reson. Imaging* **20**, 721–731 (2002).

162. Hansen, E. S. S., Stewart, N. J., Wild, J. M., Stï¿½dkilde-Jï¿½rgensen, H. & Laustsen, C. Hyperpolarized13C,15N2-Urea MRI for assessment of the urea gradient in the porcine kidney. *Magn. Reson. Med.* **76**, 1895–1899 (2016).

163. Gomez, H. *et al.* A unified theory of sepsis-induced acute kidney injury: Inflammation, microcirculatory dysfunction, bioenergetics, and the tubular cell adaptation to injury. *Shock* **41**, 3–11 (2014).

164. Cai, K. *et al.* Breast Cancer Redox Heterogeneity Detectable with Chemical Exchange Saturation Transfer (CEST) MRI. *Mol. Imaging Biol.* **16**, 670–679 (2014).

165. Jiang, K. *et al.* Noninvasive assessment of renal fibrosis with magnetization transfer MR imaging: Validation and evaluation in murine renal artery stenosis. *Radiology* **283**, 77–86 (2017).

166. Jiang, K., Ferguson, C. M., Woollard, J. R., Zhu, X. & Lerman, L. O. Magnetization Transfer Magnetic Resonance Imaging Noninvasively Detects Renal Fibrosis in Swine Atherosclerotic Renal Artery Stenosis at 3.0 T. *Invest. Radiol.* **52**, 686–692 (2017).

167. Jiang, K. *et al.* Quantitative Magnetization Transfer Detects Renal Fibrosis in Murine Kidneys With Renal Artery Stenosis. *J. Magn. Reson. Imaging* **53**, 884–893 (2021).

168. Zu, Z. Ratiometric NOE(−1.6) contrast in brain tumors. *NMR Biomed.* **31**, 1–10 (2018).

169. Cui, J., Zhao, Y., Wang, F., Gochberg, D. F. & Zu, Z. Contribution of blood to nuclear Overhauser effect at −1.6 ppm. *Magn. Reson. Med.* **87**, 409–416 (2022).

170. Chang, Y. C., Liu, H. Q., Chang, J. H., Chang, Y. Y. & Lin, E. C. Role of the cholesterol hydroxyl group in the chemical exchange saturation transfer signal at −1.6 ppm. *NMR Biomed.* **33**, 1–8 (2020).

171. Zhang, X. Y. *et al.* MR imaging of a novel NOE-mediated magnetization transfer with water in rat brain at 9.4 T. *Magn. Reson. Med.* **78**, 588–597 (2017).

172. Eckardt, K. U. *et al.* Role of hypoxia in the pathogenesis of renal disease. *Kidney Int.* **68**, 46–51 (2005).

173. Tanaka, S., Tanaka, T. & Nangaku, M. Hypoxia as a key player in the AKI-to-CKD transition. *Am. J. Physiol. - Ren. Physiol.* **307**, F1187–F1195 (2014).

174. Sharp, C. N. *et al.* Repeated administration of low-dose cisplatin in mice induces fibrosis. *Am. J. Physiol. Physiol.* **310**, F560–F568 (2016).

175. Sharp, C. N. & Siskind, L. J. Developing better mouse models to study cisplatin-induced kidney injury. *Am. J. Physiol. Physiol.* **313**, F835–F841 (2017).

176. Sharp, C. N. *et al.* Subclinical kidney injury induced by repeated cisplatin administration results in progressive chronic kidney disease. *Am. J. Physiol. - Ren. Physiol.* **315**, F161–F172 (2018).

177. Sears, S. M. *et al.* C57BL/6 mice require a higher dose of cisplatin to induce renal fibrosis and CCL2 correlates with cisplatin-induced kidney injury. *Am. J. Physiol. - Ren. Physiol.* **319**, F674–F685 (2020).

178. Wu, Y. *et al.* A generalized ratiometric chemical exchange saturation transfer (CEST) MRI approach for mapping renal pH using iopamidol. *Magn. Reson. Med.* **79**, 1553–1558 (2018).

179. McMahon, M. T. *et al.* Quantifying exchange rates in chemical exchange saturation transfer agents using the saturation time and saturation power dependencies of the magnetization transfer effect on the magnetic resonance imaging signal (QUEST and QUESP): pH calibration for poly. *Magn. Reson. Med.* **55**, 836–847 (2006).

180. Zhou, J., Lal, B., Wilson, D. A., Laterra, J. & Van Zijl, P. C. M. Amide Proton Transfer (APT) Contrast for Imaging of Brain Tumors. *Magn. Reson. Med.* **50**, 1120–1126 (2003).

181. Meier, S. *et al.* Non-invasive detection of adeno-associated viral gene transfer using a genetically encoded CEST-MRI reporter gene in the murine heart. *Sci. Rep.* **8**, 1–10 (2018).

182. Chen, H. *et al.* CEST MRI monitoring of tumor response to vascular disrupting therapy using high molecular weight dextrans. *Magn. Reson. Med.* **82**, 1471–1479 (2019).

183. Mehrabian, H., Myrehaug, S., Soliman, H., Sahgal, A. & Stanisz, G. J. Evaluation of Glioblastoma Response to Therapy With Chemical Exchange Saturation Transfer. *Int. J. Radiat. Oncol. Biol. Phys.* **101**, 713–723 (2018).

184. Sun, P. Z., Wang, Y., Dai, Z. Z., Xiao, G. & Wu, R. Quantitative chemical exchange saturation transfer (qCEST) MRI - RF spillover effect-corrected omega plot for simultaneous determination of labile proton fraction ratio and exchange rate. *Contrast Media Mol. Imaging* **9**, 268–275 (2014).

185. Xu, J. *et al.* On-resonance variable delay multipulse scheme for imaging of fast-exchanging protons and semisolid macromolecules. *Magn. Reson. Med.* **77**, 730–739 (2017).

186. Xu, X. *et al.* Magnetization transfer contrast–suppressed imaging of amide proton transfer and relayed nuclear overhauser enhancement chemical exchange saturation transfer effects in the human brain at 7T. *Magn. Reson. Med.* **75**, 88–96 (2016).

187. Pietrement, C. & Gillery, P. Protein Carbamylation : Chemistry , Pathophysiological Involvement , and Biomarkers. **84**, 1–38 (2018).

188. Claxton, J. N. S. *et al.* Endogenous Carbamylation of Renal Medullary Proteins. doi:10.1371/journal.pone.0082655.

189. Florijn, K. W. *et al.* Glomerular filtration rate measurement by "single-shot" injection of inulin. *Kidney Int.* **46**, 252–259 (1994).

190. Lam, B., Wendland, M., Godines, K., Shin, S. H. & Vandsburger, M. Accelerated multi-target chemical exchange saturation transfer magnetic resonance imaging of the mouse heart. *Phys. Med. Biol.* **66**, 145016 (2021).

191. Sui, R. *et al.* Whole-brain amide CEST imaging at 3T with a steady-state radial MRI acquisition. *Magn. Reson. Med.* **86**, 893–906 (2021).

192. Zhou, Y. *et al.* Magnetic resonance imaging of glycogen using its magnetic coupling with water. *Proc. Natl. Acad. Sci.* **117**, 3144–3149 (2020).

193. Chen, L. *et al.* Protein aggregation linked to Alzheimer's disease revealed by saturation transfer MRI. *Neuroimage* **188**, 380–390 (2019).

194. Zhang, S. *et al.* Assessment of early response to neoadjuvant systemic therapy in triple-negative breast cancer using amide proton transfer–weighted chemical exchange saturation transfer mri: A pilot study. *Radiol. Imaging Cancer* **3**, (2021).